

UNIVERSITÀ DEGLI STUDI DI TRIESTE

FACOLTÀ DI SCIENZE MATEMATICHE, FISICHE E NATURALI

CORSO DI LAUREA SPECIALISTICA IN FISICA

Curriculum: Fisica della Materia

Studio della dinamica elettronica ultraveloce del cromoforo di una proteina retinica

Relatore:

Ch.mo Prof. Fulvio Parmigiani

Laureanda:

Anna Maria Novello

Correlatore:

Dr. Goran Zgrablic

Anno Accademico 2007 - 2008



UNIVERSITÀ DEGLI STUDI DI TRIESTE

FACOLTÀ DI SCIENZE MATEMATICHE, FISICHE E NATURALI

CORSO DI LAUREA SPECIALISTICA IN FISICA

Curriculum: Fisica della Materia

Study of the ultrafast electronic dynamics of a retinal protein chromophore

Relatore:

Ch.mo Prof. Fulvio Parmigiani

Laureanda:

Anna Maria Novello

Correlatore:

Dr. Goran Zgrablic

Anno Accademico 2007 - 2008

Abstract

Il retinale svolge il ruolo di cromoforo, cioè di molecola fotosensibile, in diverse proteine retiniche come, per esempio, la rodopsina, fondamentale per il processo visivo di molti animali tra cui l'uomo, o la batteriorodopsina, che svolge il ruolo di "pompa di protoni" nell'*Halobacterium salinarium*, un archeobatterio che vive in acque saline sature.

Questa tesi riporta uno studio sulla base di Schiff protonata del retinale (PSBR) *all-trans* che rappresenta la forma più simile al cromoforo presente nelle proteine batteriche. Come solventi sono stati utilizzati il metanolo e l'acetononitrile. Questi solventi sono entrambi polari e presentano simili caratteristiche fisico-chimiche, a parte l'incapacità del secondo a formare legami idrogeno. Inoltre, in essi, si osserva una diversa efficienza di fotoisomerizzazione del PSBR [3], mentre recenti misure di fluorescenza risolte in tempo [4], mostrano anche una variazione nella durata del rilassamento vibrazionale del retinale. Questa è accompagnata da una differente dinamica di diseccitazione dal primo stato eccitato, caratterizzata dalla presenza di canali di rilassamento differenti.

Questo lavoro di tesi riporta, lo studio della dipendenza dell'efficienza di fotoisomerizzazione del retinale dalla lunghezza d'onda e quindi lo studio sulla dinamica del processo ottenuto mediante misure di "pump-probe", dove come "probe" si sono utilizzati impulsi laser ultracorti e con una dispersione spettrale continua tra ~ 420 nm e ~900 nm (supercontinuo) e come "pump" la seconda armonica dell'emissione fondamentale (800 nm) di un laser Titanio:Zaffiro amplificato.

Questo studio ha portato alla conferma della presenza di diversi canali di rilassamento, reattivi e non-reattivi, e ha permesso una stima del tempo di isomerizzazione che sarà utile come punto di partenza per successivi esperimenti.

Index

Abstract III

Index IV

1. Introduction 1

1.1 The role of retinal in living systems 4
1.2 Two-State model 7
1.3 The influence of the environment 8
1.4 Retinal photoisomerization in solvents 10
1.5 PSBR excited-state dynamics 13
1.6 Scope of the experiment 18

2. Experimental 19

2.1 Laser system 19
2.2 Steady-state set-up 21
2.3 Pump-probe set-up 23
2.4 Supercontinuum generation 25
2.5 Flattering of the supercontinuum light 27
2.6 Pump end probe pulse characterization 29
2.7 Experimental procedures 31
2.8 Data acquisition 35
2.9 An example: Rhodamine 6G 37
2.10 Cross Phase modulation (XPM) 39
2.11 GVD correction 44
2.12 Subtraction of solvent contribution 46
2.13 Pump-probe data analysis technique 49

3. Results 52
3.1 Measurements of the photoisomerization efficiency 52
3.2 Results of pump-probe measurements 57
3.2.1 The data matrices 58
3.2.2 Spectra and kinetic traces 61
3.2.3 SVD analysis 71

4. Discussion 74
4.1 Spectral structure assignments 74
4.2 Dynamics of the system 76
4.3 Early events: vibrational relaxation and S_2 internal conversion 78
4.4 Internal conversion process of the S_1 state 80
4.5 Comparison with protein environment 84

5. Conclusion 87

Bibliography 89

1. Introduction

The retinal is found in nature as the chromophore in some important biological systems such as visual pigments and photosynthetic bacteria or, more interestingly, in retinal proteins. These proteins, formed by an opsin apoprotein to which is bound an isomer of retinal via a Schiff base linkage to a lysine residue, are involved in phototransduction. Some examples are the rhodopsin, fundamental in human vision, the bacteriorhodopsin and the halorodopsin in *Halobacteria*, that function as proton and ion pump, respectively.

The biological activity of retinal proteins is triggered by the ultrafast light-induced isomerization of the corresponding retinal chromphores that, in turn, induces a conformational change of the protein. This photochemical step is the primary event of the protein photocycle and represents one of the fastest photochemical reactions observed so far in nature (~200 fs in rhodopsin) [1] .

The details of the photoreaction, i.e. the isomerization pathways, the reaction speed and the quantum yield, critically depend on the specific surrounding of the chromophore. For example in bacteriorhodopsin the isomerization is highly selective and presents a photoisomerization quantum yield (Φ) of 65% [2] while in solution the yield is low (~20%) [3] and the isomerization is not selective, that is, it can happen along various double bonds. In order to separate the influence of

the protein from the intrinsic properties of the retinal molecule, it is essential to investigate PSBR in solution.

The protonated Schiff base of *all-trans* retinal (PSBR) is the form most similar to that found in *Halobacteria* where the chromophore isomerizes from *all-trans to cis* form.
In the past, detailed studies on photoisomerization efficiency in solution by high-pressure liquid chromatography (HPLC) were taken [3]. They determined Φ and studied the effects of protonation, polarity and hydrogen bonding of the solvents, but they did not consider the possible dependence on the excitation wavelength (λ_{ex}). The existence of this dependence is suggested by results of fluorescence measurements [4], where different decay channels for different λ_{ex} are found. In particular, the disappearance of the 0.6-0.9 ps decay channels, when the molecule is excited at 540 nm instead at 400 nm suggests a dependence of Φ on the wavelength [4]. To study this process, a novel all optical set-up is developed, while Φ of PSBR in methanol and acetonitrile, have been measured.
The choice of these solvents comes from the fact that in the latter solvent Φ is 50% larger [3]. Moreover, in acetonitrile the PSBR photoisomerization is independent from λ_{ex} while the presence of the 0.6-0.9 ps decay channel is not observed.

To obtain a more complete analysis of the photoisomerization process, the PSBR ultrafast dynamics are studied using pump-probe measurements. Femtosecond transient absorption spectroscopy [5,6,7] has been already used to study the light induced isomerization reaction of PSBR in methanol and acetonitrile, however this is the first time that measurements with ~60 fs has been performed. The scope of this experiment is to understand, beside the dynamics of the system, the reaction paths of the isomerization processes and their boundary conditions.

The thesis is organized as follow.

In section 1, after a brief introduction on the role of retinal in living systems and a short presentation of the two-state theoretical model describing the isomerization path, the attention is concentrated on the photoisomerization process in solvents with a summary of the principle results from previous HPLC, pump-probe and fluorescence measurements.

In section 2 the experimental set-ups for steady-state and pump-probe measurements together with the experimental procedure are described. A particular attention is dedicated in explaining the phenomenon of cross (X) phase modulation (PM) that affects pump-probe measurements.

Finally, a brief introduction of the analysis technique used to treat pump-probe data is also given.

In section 3 the results are presented and analyzed, while their discussion is reported in section 4.

In section 5 the conclusion is reported where the main results are summarized with their interpretation.

1.1 The role of retinal in living systems

A chromophore is a photosensitive molecule responsible for visible light absorption. In retinal proteins consists of a retinal isomer - a derivative of vitamin A – covalently bound to the protein via a protonated Schiff base linkage through a lysine residue [8,9].

In solution, the closest analogue to the chromophore in protein is the protonated Schiff base of Retinal (PSBR) that isomerizes under the influence of light (Fig.1.1). Light-induced isomerization starts biological function in a number of different photosensitive proteins. Here are some examples of different isomerization types in proteins:

- Rhodopsin (*11-cis→all-trans*) and Retinochrome (*all-trans→11-cis*), which are the key unit of vision in human and in many other vertebrates and cephalopods, respectively [10,11,12,13,14,15] ;
- Bacteriorhodopsin which serves as a light driven proton pump in bacteria *Halobacterium salinarium*, demonstrating an alternative form of photosynthesis (*all-trans→13-cis*) [16,17,18];
- Halorhodopsin, which is similar to Bacteriorhodopsin but functions as a light-induced chloride pump in *Halobacteria* (*all-trans→13-cis*) [19,20].

As an example, in Fig. 1.2 the crystal structure of bovine rhodopsin is reported, where the retinal chromophore and the opsin protein can be distinguished. Rhodopsin (Rh) is a visual pigment consisting of an apoprotein (opsin) and a chromophore (11-cis retinal) and its tertiary structure is formed by a bundle of seven transmembrane α helices connected by six loops of varying lengths [10]. The ground-state chromophore, 11-cis retinal, holds the transmembrane region of

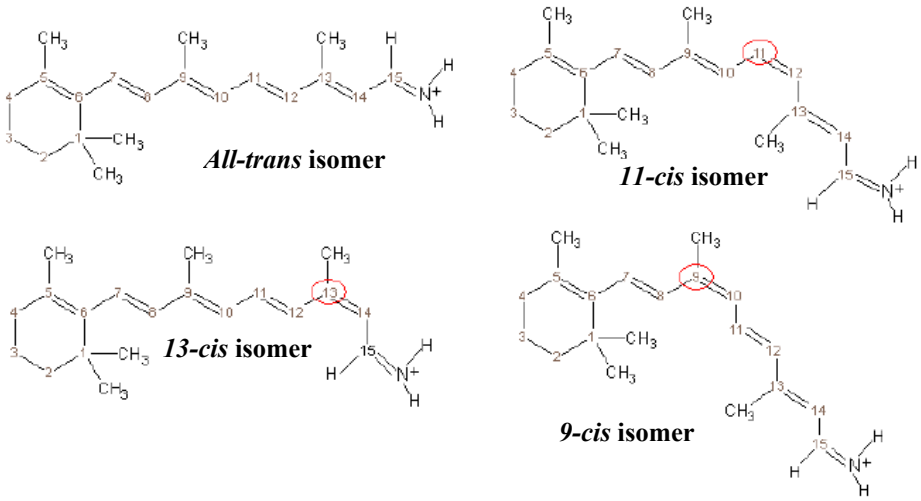


Fig. 1.1: Different isomers of protonated Schiff base of retinal.

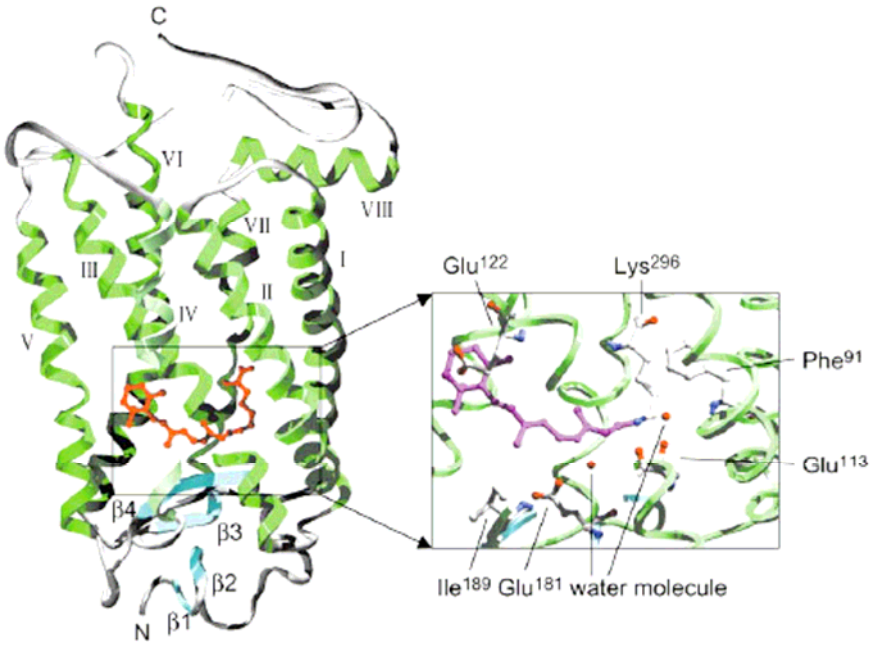


Fig. 1.2: Crystal structure of bovine rhodopsin parallel to the plane of the membrane. In the right panel, the six amino acid residues and the two water molecules around the chromophore are shown. [21]

the protein in the inactive conformation. Interactions of the chromophore with a cluster of key residues (charged aminoacids) determine the wavelength of the maximum absorption and changes in these interactions among various rhodopsins permit colour discrimination. Rhodopsin is contained in the retina, in the cones, photoreceptors used for vision in daylight and for colour vision, and in the rods that are responsible for vision in dim light [11, 22, 23, 24]. Absorption of a photon by the 11-cis retinal causes its isomerization to *all-trans* retinal, leading to a conformational change of the protein moiety, including the cytoplasmic surface. The photopigment is activated and this triggers the signal amplification cascade that stays at the base of the vision process. The photolyzed chromophore only transiently activates opsin, before the *all-trans* retinal is hydrolyzed and dissociated from the opsin. Rhodopsin is regenerated by newly synthesized 11-cis retinal delivered from adjacent retinal epithelial cells [10,24].

An example of isomerization from the *all trans* state to the *cis* state, the process we are investigating in our experiment, can be found in the light-driven proton pump Bacteriorhodopsin (bR). The transport of protons across membranes is an important process in cellular bioenergetics and bR is the best-characterized protein providing this function. The structure of the protein is very similar to that of Rhodopsin, but in this case retinal isomerizes from *all-trans* to *13-cis*. In particular light induced isomerization of retinal results in deprotonation of the Schiff base followed by alterations in protonatable groups within bacteriorhodopsin. The changed force field induces changes, even in the tertiary structure, which are necessary for proton pumping [18,25].

1.2 Two – State Model

To describe the chromophore isomerization path, the most accepted model is the so called 2-state/2-mode model, which is elaborated in several quantum chemical calculations for different Rhodopsin proteins [26, 27]. Here we consider the all-*trans*→*cis* process but the same model applies to any isomerization type (11-*cis*→*all-trans*, *all-trans*→13-*cis*).

If we consider the two potential energy surfaces (PES) of the ground and excited state – S_0 and S_1 respectively – the basic idea is that there is a non-zero slope along the S_1 reaction coordinate, corresponding to the double-bond torsional mode, which causes the acceleration of the molecule toward the decay channel. At first, it was considered that the principle reaction coordinate is a torsional motion about the "reactive" double bond, but more recent computations [28] show that the S_1 reaction coordinate is sequentially dominated by two uncoupled modes. In Fig. 1.3 the absorption process is represented from the point of view of the PES. In the first step, the electrons go from the ground state to the excited state following the Franck Condon principle and then the stretching of double bonds along with the shortening of single bonds start, in other words the molecule relaxes from the Franck Condon point (FC) to the stationary point (SP), where SP corresponds to "metastable" species that are more flexible, so that they isomerize more efficiently . This is a common mechanism in many photoactive molecules [29].

In the second step a torsional motion around one of the central double bonds starts. In contrast to the first mode (stretching), that is totally symmetric, the second mode (torsional) is asymmetric [26].

When the coordinates of the center of mass of the molecule overlaps with the coordinates of the conical intersection (CI) between the potential surfaces of the excited (S_1) and of the ground state (S_0), two possibilities open:

1. the molecule returns back to the *all trans* initial state;
2. it reaches a new equilibrium point on the S_0 surface that corresponds to a *cis* conformation.

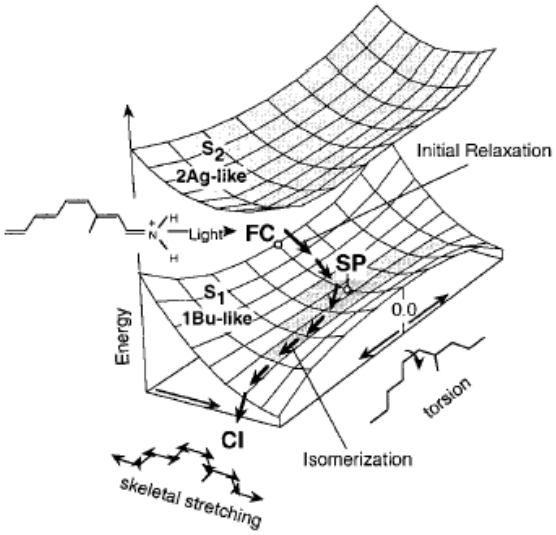


Fig. 1.3: Structure of the S_1 surface along the reaction path. After the absorption of a photon, the path starts from the FC zone and continues along the skeletal stretching mode to the SP and then along torsional coordinate to the CI. [26]

1.3 The influence of the environment

Investigations of the photochemistry of PSBR have established fundamental role of the environment in determine selectivity [2, 3, 31], quantum yield [2, 3, 30, 31, 32, 33] and time scales of the photoisomerization process [4, 5, 6, 7, 34, 35, 36, 37]. In order to separate the influence of the protein from the intrinsic properties of the retinal molecules, it is essential to investigate PSBR in solution. Here, the main differences observed between PSBR in the protein and in the solvent environments are reported.

a. Reaction selectivity

PSBR has five double bonds (Fig.1.1) capable of undergoing isomerization. After absorption of light, the chromophore isomerizes and the configuration of the photo-products (e.g., 11-cis or 13-cis) depends on the environment. In fact, in the protein environment, isomerization occurs exclusively around a single bond. For

example only 11-cis → *all trans* in Rhodopsin and *all-trans* → 13-cis processes are present in Rh and bR respectively. In contrast, PSBR is solution isomerizes to different photo-products with 11-cis being the most dominant [3]. A possible explanation of this behaviour is proposed in a theoretical work by Ben-Nun et Al. [38] in which the origin of bond selectivity is attributed to the shape (topography) of the PES in the vicinity of points of true degeneracy (conical intersections) between the ground and first excited electronic states. This theory seems to be confirmed by recent calculations on rhodopsin [39] where it is shown that the protein cavity induces a large deformation of the S_1 and S_0 PES near conical intersections.

b. Photoisomerization efficiency

The quantum yield of photoisomerization **Φ_{iso} (isomer A)** is defined as the number of the starting isomer A molecules which disappeared through isomerization per the number of photons absorbed [3]. Some measurements of Φ_{iso} in different environments reveal it is larger than 50% in proteins [2] and less then 20% in most solvents [3,32]. A detailed discussion on the photoisomerization efficiency of PSBR in solution is reported in the next paragraph.

c. Time-scales

The two-state model seems to be confirmed by pump-probe measurements and the relaxation times corresponding to the depopulation of FC zone, the vibrational energy redistribution and to the evolution of the species at SP toward CI were determined [5,7]. It was found that these processes appear with different time-scales in protein and solvent environments.

For example, for PSBR in ethanol [5,6,7] the following relaxation times were found:

1. the FC → SP relaxation occurs in <100 fs;

2. the evolution of the S1 molecule states toward CI occurs in few picoseconds.

The initial dynamics appear to be similar in the protein environment [40, 41, 42, 43], but S_1 lifetimes are very different, resulting ~200 fs in rhodopsin [1] and ~500 fs in bacteriorhodopsin [40]. Some computations made by R. Gonzalez-Luque et al. [26] suggest that the S_1 lifetime is, to some extent, controlled by the presence of a long energy plateau and/or a small barrier along the torsional mode. This barrier may be smaller or even disappear when the chromophore is enclosed in the protein cavity, thus explaining the increase in the reaction rate.

1.4 Retinal photoisomerization in solvents

Studies on isomerization efficiency in solution by high-pressure liquid chromatography (HPLC) were done by Becker and Freedman [31,32], who determined the quantum yield of photoisomerization (Φ) and studied the effects of protonation as well as of the polarity and hydrogen bonding of the solvents, a work continued by Koyama et al [3]. Here a summary of their results is given with particular attention to methanol (MeOH) and acetonitrile (ACN), since they are the solvents used in our experiments. The steric structures of methanol and acetonitrile along with some physical-chemical properties are reported on Fig. 1.4 and Table 1.1, respectively.

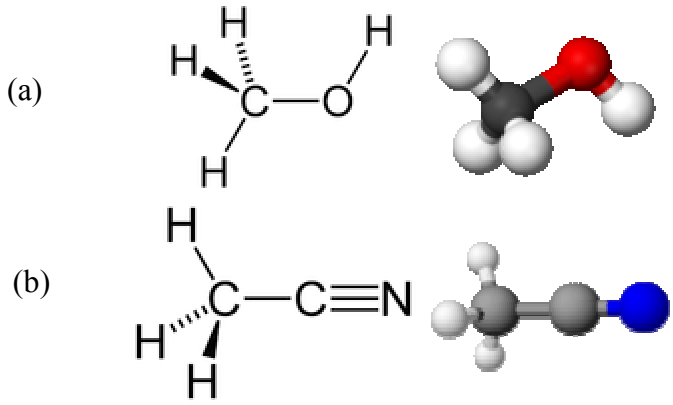


Fig. 1.4: Chemical structures of (a) Methanol (MeOH) and (b) Acetonitrile (ACN).

	MeOH	**ACN**
ε_r ($\omega = 0$)	32.66	35.94
n_d	1.327	1.342
η (mPa s)	0.547	0.345

Table 1.1: Solvent properties: static dielectric constant $\varepsilon_r(\omega = 0)$, refractive index n_d and absolute viscosity η [44].

Before starting to describe the different cases studied, it is useful to introduce some nomenclature:

- Φ' (isomer A→isomer B) = number of the isomer B molecules produced from the isomer A molecules through photoisomerization per the number of photons absorbed; the sum of Φ' over all the isomerization products equals Φ_{iso}(isomer A).

- Single(two)(three)-way isomerization = only one kind (two-three kinds) of isomer is (are) generated from a starting isomer. If $\Phi'=\Phi_{iso}$ we have a single-way isomerization.

- One way A→B isomerization = considering a pair of isomers (A and B), when the A←B isomerization is negligible compared to the A→B isomerization.

- Mutual isomerization = when both the forward and the reverse isomerization is comparable.

Koyama et al. [3] studied both deprotonated (SBR) and protonated Schiff base of retinal (PSBR). They can be distinguished spectroscopically because they have different spectral maximum (λ_{max}) values, lower in the first case than in the second. Of particular interest is the case of SBR in different solvents, since its larger λ_{max} values in the alcohols with respect to those in n-hexane and ACN

probably reflect hydrogen bonding of the SBR with alcohols. It has been established that alcohols act as hydrogen donors on Schiff bases [45] and for this reason alcohols are often called "hydrogen-bonding" solvents.
From their measurements three important observation can be made:

1. *all-trans* SBR goes to 13-cis if it is in a non-protonating environment (n-hexane or ACN) while 11-cis is produced if it is in a protonating environment (MeOH). Thus, it can be said that the isomerization pathways from all-trans is controlled by protonation;

2. *all-trans* PSBR goes to 11-cis both in a non-proton donating and in a protonating environments, as in previous case of *all-trans* SBR in MeOH, suggesting that the "protonated state" can be induced either by the acid through direct protonation, or by alcohols through hydrogen-bond formation;

3. larger Φ_{iso} is found in *all-trans* PSBR in ACN, a non-proton-donating and polar environment, respect to the case of MeOH, so it is observed that the photoisomerization is accelerated when the protonated species is in a polar but no-hydrogen-bonding environment.

In Table 1.2 Φ_{iso} and Φ'_{iso} values for PSBR in MeOH and ACN are reported. In particular it can be noted that PSBR in MeOH presents a three-way isomerization while PSBR in ACN presents a two-way isomerization with 13-cis isomer as a secondary product. Anyway in both cases 11-cis isomer has the largest Φ'_{iso} value. The reason why Φ_{iso} is largest in ACN is not understood. In fact, from Table 1.1 it is evident that the two solvents have similar properties and the only evident difference is capability to make (MeOH) or not (ACN) hydrogen bonds. Anyway we can note that from the point of view of Φ_{iso}, ACN seems to be the most similar to that of the protein environment where the retinal is hosted. Therefore, it

is interesting to investigate and compare the behaviour of Φ_{iso} and the excited state dynamics in these two solvents.

		MeOH	**ACN**
Φ_{iso}		0.17±0.03	0.27±0.04
Φ'_{iso}	11-cis	0.14	0.25
	9-cis	0.02	0.01
	13-cis	0.01	-

Table 1.2: The quantum yields Φ_{iso} and Φ'_{iso} for PSBR in MeOH and ACN [3].

1.5 PSBR excited-state dynamics

The light induced isomerization reaction of PSBR in solution has been studied both by femtosecond absorption [5,6,7] and fluorescence spectroscopy [4,36]. The scope of these experiments is to understand the dynamics and the reaction path of the isomerization process and how they are influenced by the environment.

As reported before, since the earliest pump-probe experiments three principle phases are recognized related to the population of the F.C. region, the vibrational energy redistribution and then relaxation along different torsional coordinates[5,7]. An unexpected behaviour is observed in the third phase in a pump-probe experiment of *all trans* PSBR in ethanol by Hamm et al. [5] and then confirmed from other measurements [7]. In theory, reaching a fully vibrational relaxed electronic state leads to a reaction rate which is time-independent, i.e. a mono-exponential decay of the excited molecules would be observed at late delay times. Instead, what Hamm et al. [5] observe experimentally is a bi-exponential decay with time constants of 2 and 7.2 ps. A possible explanation proposed is the presence of two different decay channels from two separate local minima on the S_1 potential surface, the reactive pathway (i.e. the isomerization pathway) and the loss pathway (i.e. the back reaction to the *all-trans* configuration) respectively [5]. At first this theory was used to explain the photoreaction of Halorodopsin that,

unlike other proteins, presents a biexponential decay of the electronic transition from the excited to the ground state [46], but it can equally well describe also the behaviour of PSBR in solution as concluded from recent ultrafast fluorescence measurements in various solvents [4].

A complete study of the steady-state absorption and fluorescence spectra of *all-trans* PSBR in different solvents has been recently done by Zgrablic et al. [4]. Two different excitation wavelengths were used, 570 and 400 nm. It is noted that for excitation at 570 nm, i.e. the wavelength where absorption and emission spectra intersect, no excess energy is delivered to the chromophore that could populate higher vibrational states in the excited state. For this reason the fluorescence spectra collected upon 570 nm excitation are called "vibrationally equilibrated spectra" [4]. Another consideration about the choice of these two wavelengths is the fact that a previous two photon thermal lens study [47] reports how at 570 nm only the S_0-S_1 transition can be excited, while at 400 nm also the S_2 state may be accessed.
Time-resolved fluorescent experiments are of particular importance since, respect to pump-probe measurements, they have the advantage of connecting only the excited state and the ground state surfaces.
The spectral deconvolution of the time resolved fluorescence spectra allowed Zgrablic et al. [4] to isolate three spectral components (Fig.1.7):

1. *spectral component a (or main spectral component)*: related to vibrationally relaxed S_1 fluorescence, i.e. to the emission originating from transitions from the bottom of S_1 potential energy surface to the vibrational levels of the ground state;
2. *spectral component b (or double spectral component)*: related to a vibrationally "hot" S_1 fluorescence;
3. *spectral component c (or blue spectral component)*: related to S_2 fluorescence.

A large difference between the b-spectral component decay constants in MeOH and ACN has been observed. Since it is greater in MeOH respect to the latter, it can be concluded that ACN cools down the molecule more efficiently.

Since the time decay of the c-spectral component does not show up in the rise of the other spectral components, they conclude that the S_2 state is not connected to S_1 and its spectral evolution reflects its relaxation due to cooling.

The time evolution of the a-component can be described by a multiexponential function whose decay time constants are reported in Table 1.3. In most solvents the vibrationally equilibrated S_1 fluorescence relaxation can be described using three decay components upon 400 nm excitation, and only two of them upon 570 nm excitation (not reported in table 1.3). In ACN even upon 400 nm excitation only two decay components are necessary. The different lifetimes associated to the decay kinetics of the a-component are denoted channel I to III, that are channels responsible for PSBR photoreactivity.

The bi (or tri) -exponential decays are attributed to two (or three) different minima on the S_1 potential surface, with pre-exponential factors reflecting the relative population of these channels. According to this interpretation, in ACN the III channel is dominantly populated respect to others, while in other solvents, where also another channel (I) is present, it is unfavourably populated. The general picture that emerges is that not only the S_1 fluorescence stem from several minima, but the population pathways to these radiative channels differ with the excitation energy and with the solvent. Since ACN has the highest isomerization yield, the slower decay channels II and III are attributed to isomerization (reactive pathways) while channel I is considered as non-reactive or loss channel. Channels II and III lead to conical intersections, where additional *trans-cis* partition takes place, which may be the main effect that limits the isomerization yield in ACN and in other solvents.

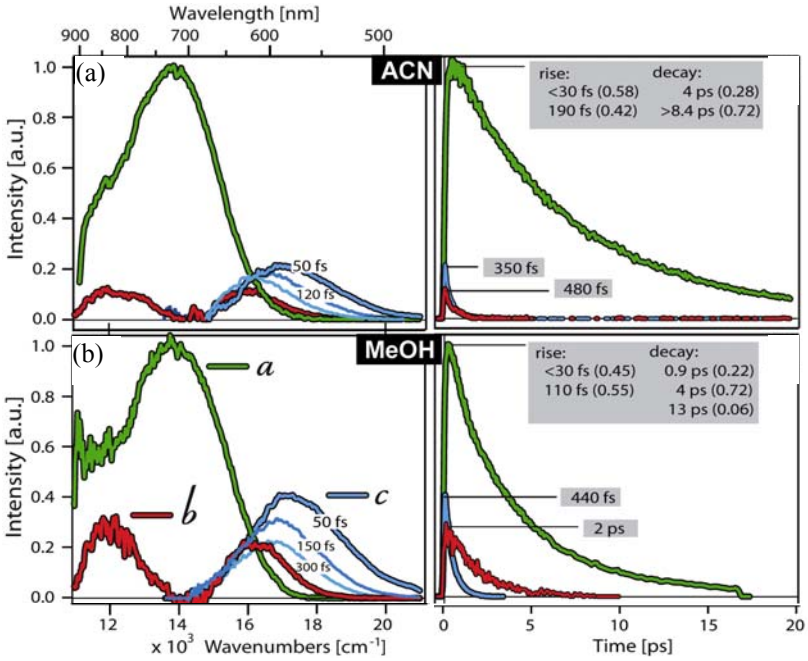


Fig.1.7: The Decay associated spectra (left) and the corresponding kinetic traces (right) in ACN (a) and MeOH (b) [4].

	MeOH	**ACN**
a-spectral component		
τ_{rise1}/fs	<30 (0.45)	<30 (0.58)
τ_{rise2}/fs	110 (0.55)	190 (0.42)
τ_1/fs (channel I)	0.9 (0.22)	-
τ_2/fs (channel II)	4.0 (0.72)	4.0 (0.28)
τ_3/fs (channel III)	13 (0.06)	8.4 (0.72)
b-spectral component		
τ_b/fs	2	0.48
c-spectral component		
τ_c/fs	0.44	0.35

Table 1.3: The values in each row are: rise and decay time constants τ_i and relative amplitudes (in parenthesis) of the i-th decay for a-spectral component, and decay time constants τ_b and τ_c for b- and c-spectral component. The uncertainties on lifetimes are: $\tau_{rise1} \pm 20$ fs, $\tau_{rise2} \pm 50$ fs, $\tau_{1,2} \pm 0.5$ fs, $\tau_3 \pm 3$ ps, $\tau_b \pm 0.3$ ps, $\tau_c \pm 0.08$ ps [4, 44].

The model proposed by Zgrablic et al. [4] to describe the relaxation leading to the radiative decay channels starts from that of Gonzalez-Luque et al. [26] but it is extended up to three SP_s on the S_1 hypersurface. A scheme of this model is reported in Fig. 1.8 where one observes:

1. the primary event is in the ultrafast (<30fs) relaxation from the F.C. excited region into a non-stationary point on the excited-state surface, which is labelled I^*;
2. the consequent relaxation lead to population of the SPs on the S_1 surface belonging to the a-structure (green-shaded area, Fig. 1.8) and of a SP on the S_2 surface giving rise to the c-spectral component (blue shaded area, Fig.1.8).

More theoretical work is needed to explain the behaviour in ACN, which, besides accelerating vibrational relaxation, seems to affect topography of the excited state potential of the PSBR.

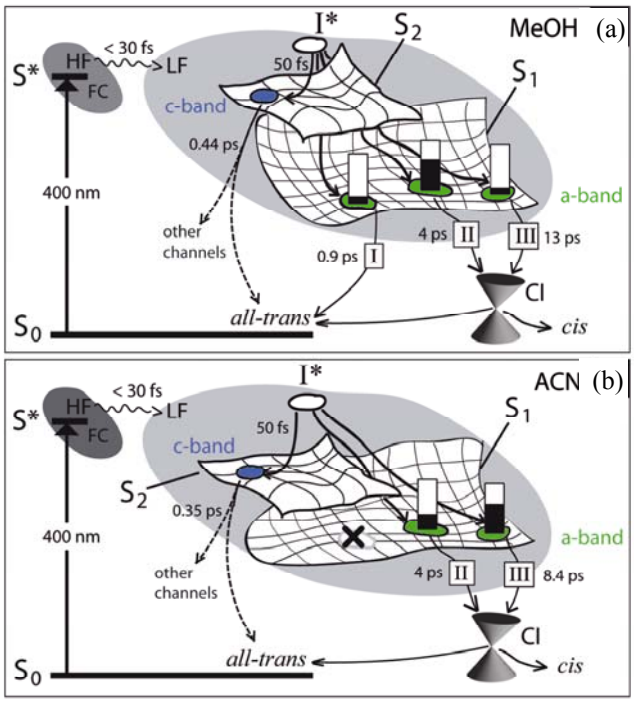


Fig. 1.8: Schematic representation of SPs on the S_1 and S_2 surfaces for PSBR MeOH and ACN [4]: (a) MeOH upon 400 nm excitation; (b) ACN upon 400 nm excitation.

1.6 Scope of the experiment

As discussed above, the fast decay channel (channel I) was individuated and assigned to the repopulation of *all-trans* ground state. It is detected upon 400 nm excitation while it is absent upon 570 nm excitation when no excess of vibrational energy is given to the molecule. The only exception is ACN where this channel is missing also upon 400 nm excitation and this is probably due to an effective dispersion of the exciding of energy. This observation is of particular interest because ACN is also the solvent in which PSBR has the larger photoisomerization efficiency [3], therefore realizing an environment quite similar to that of the protein. The absence of a fast decay channel could be responsible for the high photoisomerization efficiency. To verify this effect, photoisomerization measurements upon different excitation wavelengths and in different solvents are needed. In fact, the photoisomerization efficiency of the all *trans*→*cis* reactions should be excitation-wavelength independent in ACN, whereas in other solvents (MeOH in our case) it should increase if the excitation energy is decreased. This is what we want to verify with our first experiment where the photoisomerization efficiency, at different excitation wavelengths (400 and 540 nm), is measured. To this end we use a novel all-optical method where the decreasing of the optical density (OD), induced by the increasing concentration of the *cis*-isomer in solution due to the light exposure, is measured. The variation of OD originates from the extinction coefficient of the *cis*-isomer, which is 50% smaller than the extinction coefficient of the *all-trans* [32].

In the second experiment a pump-probe experiment of the PSBR in MeOH and ACN upon 400 nm excitation has been used to study the decay dynamics between S_1 and S_0. The dynamic of the isomerization process is observed focusing to individuate any possible differences between the two environments. In particular, the presence of the decay channels observed in the fluorescence processes has to be confirmed.

2. Experimental

In this section, after a brief description of the laser system, the steady-state and pump-probe set-ups are presented. The pump and probe pulses are fully characterized and a test measurement with a dye is shown. A short theoretical description of supercontinuum generation is also reported, while in the final part the cross-phase modulation (XPM) effect is introduced and used for determing the group velocity dispersion (GVD) of supercontinuum . This section ends with an introduction on the data analysis technique, and the singular value decomposition (SVD), used to elaborate the pump-probe data.

2.1 Laser system

The light source used is a commercial laser system consisting of a Ti:Al_2O_3 (Titanium Sapphire – Ti:Sa) Oscillator (Coherent-Mira Seed) and a regenerative amplifier (Coherent-Legend). The scheme of the system is reported in Fig. 2.1.

The oscillator is pumped by a Neodymium Vanadate (Nd:YVO_4) laser (Coherent-Verdi): a CW laser with a wavelength of 532 nm and with an average power of 5 W. The oscillator uses a passive mode-locking, based on the Kerr-Lens mode locking mechanism, to obtain pulses of ~20 fs, duration centered at 795 nm, with

~48 nm bandwidth, few nJ per pulse, at a repetition rate of 76 MHz that provide an average power of 350mW [48]. Then the pulses enter in the amplifier pumped by a Neodynium:Yttrium Lithium Fluoride (Nd:YLF) laser (Coherent-Evolution 30) providing pulses at a wavelength of 527 nm, time duration 300 ns, average power 20 W and repetition rate 1 kHz. After a three-step process in which the pulses are stretched, amplified, and recompressed, the final output is obtained, that consists in 2.5 mJ pulses with a wavelength of 800 nm, duration of 50 fs, at repetition rate of 1 kHz that result in average power of 2.5 W [49].

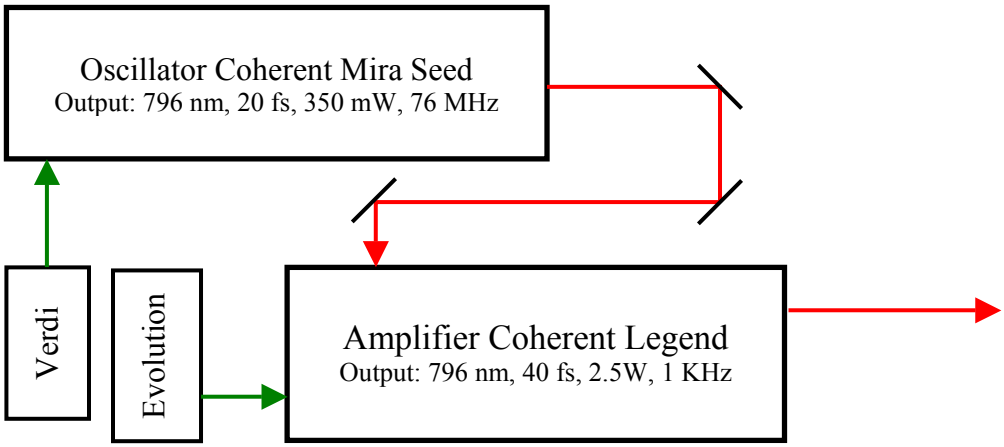


Fig 2.1: Laser system scheme

2.2 Steady-State set-up

A set-up able to measure how sample absorption changes in time has been constructed (Fig. 2.2). Two kinds of light source are used: one is a halogen lamp with a monochromator and the other is the laser system described before. The former is used to continuously illuminate the sample at a specific wavelength (400 or 540 nm). The latter is used to generate the supercontinuum (SC), a white light pulse that covers the range from infrared to ultraviolet, that is used to measure the transmission spectra of the sample. The theory that stays behind the SC generation is briefly reported in paragraph 2.4. In practice, it is generated by focusing the laser beam, whose power is controlled by a variable filter, into a 2 mm thick CaF_2 crystal. To avoid damage of the crystal due to intense laser beam, the crystal is slowly oscillating at a frequency of 1 Hz. After the crystal a spherical mirror re-collimates the beam which is then splitted into two parts by a 50%-50% metallic coated beamsplitter into the signal and the reference beam. Since the white light is not perfectly stable due to intrinsic laser instability, it is necessary to have the reference beam. Finally the two beams are focalized by a spherical mirror with a focal length of 15 cm so that only one passes through the sample. After the sample the two beams are dispersed with a transmission grating and the spectra are collected by two photodiode arrays with 512 pixel. Before the beamsplitter the supercontinuum beam passes through BG39 filter (Schott) to cut-off the contribution of the remaining fundamental that could cause heating of the sample.

The excitation beam is focalized on the sample to have an uniformly illuminated rectangle of 7x10 mm (Fig. 2.3). The beam intensity is regulated by varying the voltage on the power supply of the lamp and is adjusted using a laser power meter and a silicon detector head suitable for low intensity light sources. The probe beam has ~1.5 mm diameter and a power intensity of 0.3 μW.

The retinal solution is put in a quartz flow cell (fig 2.3) connected to a peristaltic pump that permits us to easily change the sample. The flow cell is 3 mm thick, sample inside only 0.5 mm, and has a window of 8x25 mm.

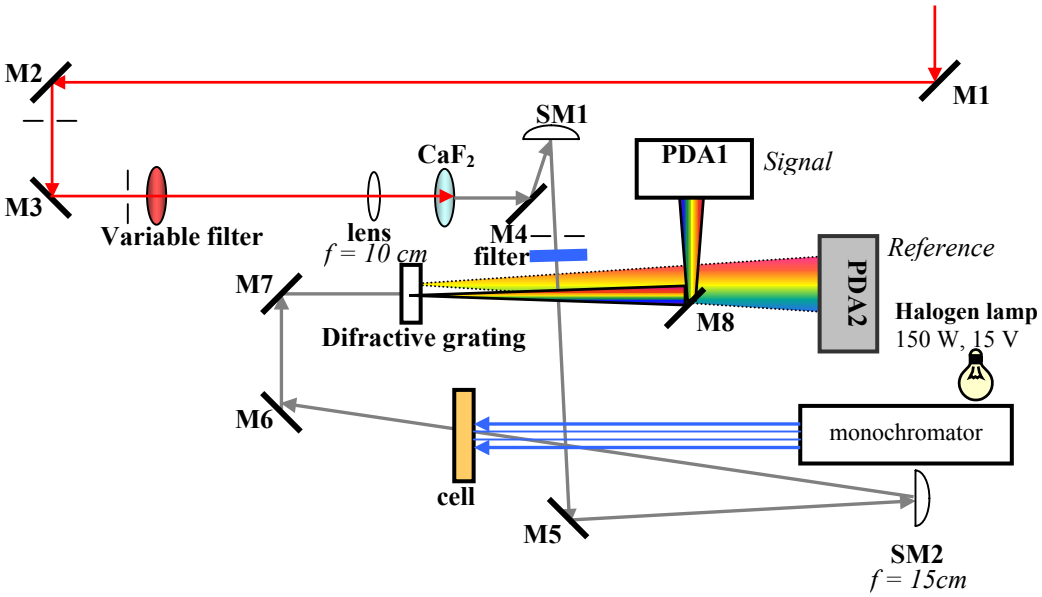


Fig. 2.2: Steady-state set-up scheme. M = mirror, SM = spherical mirror, PDA = photodiode array.

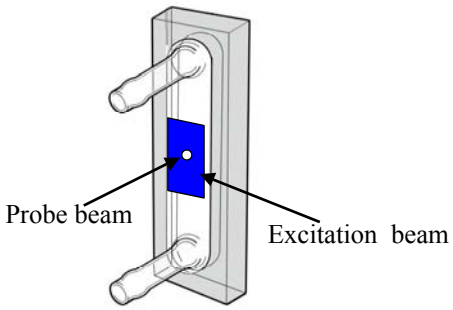


Fig. 2.3: The flow cell. It can contain a solvent layer 0.5 mm thick. The excitation (rectangle) and probe beams (circle) are shown.

2.3 Pump-Probe set-up

The pump-probe set-up scheme is reported in Fig. 2.4. At the beginning of the set-up, the beam coming from the laser is divided by a 10%-90% beam splitter into two beams. The more intense passes through a type-I BBO crystal (beta-BaB_2O_4), to obtain the second harmonic (400 nm) from the fundamental (800 nm). This is our pump beam, whose power is controlled by a λ/2-plate BBO crystal. After the frequency doubling, the pump beam is filtered by three dichroic mirrors in order to eliminate the infrared light that remains after the harmonic generation. Then it passes through a 125 Hz chopper, synchronized to the laser. After the chopper a beam-splitter divides the beam. The first beam is monitored by a photodiode, while the other is used to excite the sample (pump) after being focused by a f = 25 cm spherical mirror.

The IR laser beam (10% of the full laser beam) is used to generate the supercontinuum as before: this is our probe beam. Also in this set-up there is a reference beam for the supercontinuum light. The only difference with the previous set-up is the absence of the BG39 filter since for these measurements a more extended spectrum of the supercontinuum light is needed. Part of the fundamental laser light is removed

by putting a solution of an infrared organic dye (IR140) after the sample. This filters out the infrared part of the spectrum which is two order of magnitude more intense and causes the saturation of the PDAs. The details about the dye are focused on paragraph 2.5.

The pump and the probe beams are focalized on the sample by two spherical mirrors, with focal length of 25 cm and 15 cm, respectively. In this way it is possible to control independently the focal position and diameter of the pump and probe beams. On the sample the focus of the probe must be smaller than the focus of the pump in order to observe an area uniformally illuminated by the pump (see paragraph 2.6).

After the sample the pump beam is spatially filtered, while, as in the other set-up, the probe and the reference pass through a transmission grating, while the resulting spectra are collected by two photodiode arrays with 512 pixel.

The spatial superposition of the pump and the probe beams is controlled by two spherical mirrors set before the sample, while the temporal overlap is controlled by moving the delay line on the probe path. The resolution of the delay line is ~0.03 μm in space, i.e. ~0.1 fs in time.

As before, the sample is contained in a flow cell connected to a peristaltic pump. The pump is necessary to allow the fluid sample recirculation so that every time that a pump beam arrives, it excites a fresh sample, so that the system is probed always at the same initial conditions.

Finally, it is important to underline that the presence of the cell and of the solvent introduces a change in the GVD that has to be corrected [50, 51, 52, 53]. This correction procedure will be discussed on paragraphs 2.10 and 2.11.

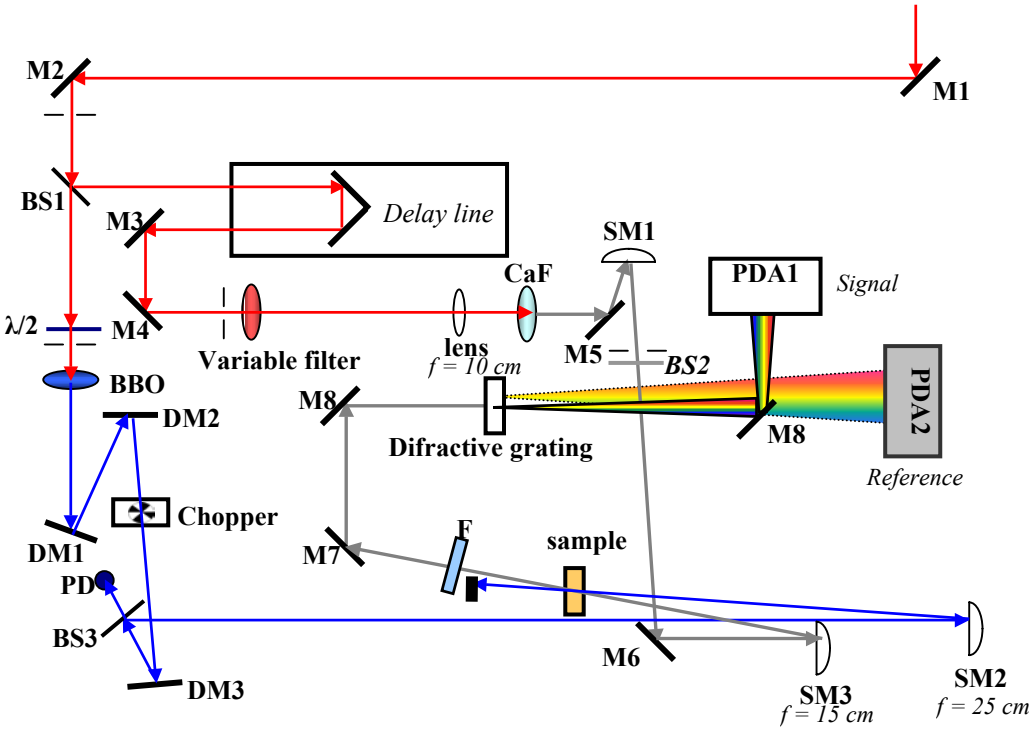


Fig. 2.4: Pump-Probe set-up scheme. M = mirror, SM = spherical mirror, DM = dichroic mirror, BS = beam splitter, PD = photodiode, PDA = photodiode array.

2.4 Supercontinuum generation

The first experimental observation of supercontinuum was made by Alfano and Shapiro [54] who observed a frequency broadening in calcite, quartz and several glasses under picosecond pulse excitation. It consists in a non-linear process due to the dependence of the refractive index of the medium to the intensity of the pulse:

$$n(t) = n_o + \Delta n(t) = n_o + n_2 I(t), \tag{2.1}$$

where n_o is the time-independent part, n_2 is the non-linear component describing the strength of the coupling between atoms and the electromagnetic wave, and $I(t)$ is the intensity of the laser pulse. This dependence has as a consequence a modulation of the phase of the different components of the pulse (self-phase modulation - SPM) [55]. In a dispersive medium of length L, the phase of the electric field is given by $\varphi_m(t)=n(t)kL=n(t)2\pi L/\lambda$, therefore the difference in the phase introduced by the dependence of the index of refraction on the pulse intensity is:

$$\exp[i\Delta\varphi(t)] = \exp\left[\frac{-i2\pi\Delta n(t)L}{\lambda}\right] = \exp\left[\frac{-i2\pi n_2 I(t)L}{\lambda}\right]. \tag{2.2}$$

If $n_2 > 0$ (the most common case), there is a decreasing of the frequency (red-shift) on the front side of the pulse ($dn/dt > 0 \Rightarrow \Delta\omega_i(t) = \frac{d}{dt}\Delta\varphi(t) < 0$) and an increasing (blue-shift) on the back. The supercontinuum polarization is the same as the one of the incident pulse. [56]

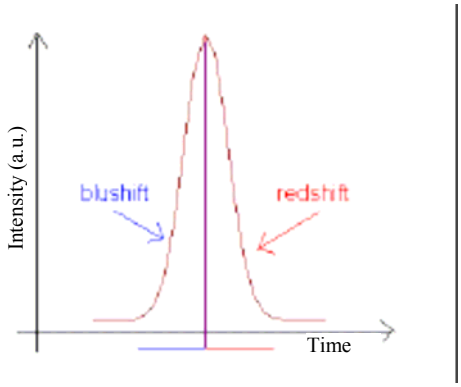


Fig. 2.5: Schematic representation of a laser pulse: due to SPM, the front part is redshifted while the back part is blueshifted

It is important to underline that the supercontinuum generation is intrinsically affected by the problem of group velocity dispersion (GVD) due to the fact that in every material the index of refraction depends non-linearly on the frequency of the incident pulse. If we rewrite the phase of the electric field as $\varphi_m(\omega)=n(\omega)kL=k(\omega)L$, its Taylor expansion gives:

$$k(\omega)L = k(\omega_0)L + \left(\frac{dk(\omega)}{d\omega}\right)_{\omega_0}(\omega-\omega_0)L + \frac{1}{2}\left(\frac{d^2k(\omega)}{d\omega^2}\right)_{\omega_0}(\omega-\omega_0)^2 L + ... \quad (2.3)$$

The first term is related to the phase velocity, the second to the group velocity, while the third one represents the GVD. The meaning of this term is that the group velocity is different for different pulse frequency so that there is a chirp of the pulse that must be corrected [57].

2.5 Flattering of the supercontinuum light

Our supercontinuum spectrum spans from ~400 nm to 900 nm but it is necessary to filter the near infrared part around 800 nm (the fundamental of the laser) to avoid the saturation of the PDA. For this purpose an organic dye, IR 140, that absorbs in the range of interest was chosen (Fig. 2.6). In particular, we use a solution in methanol with an OD~1.6, at 800 nm (value obtained in a spectrophotometer with a 1 mm thick cell). The solution is put in a cell that is placed after the sample so that the probe and the reference beams can pass through and it can be filtered out. The solution in the cell should be changed every two-three days because it is not stable in time and after some days the molecules bleaches.

In Fig. 2.7 a spectrum of the supercontinuum used in pump-probe measurements is reported.

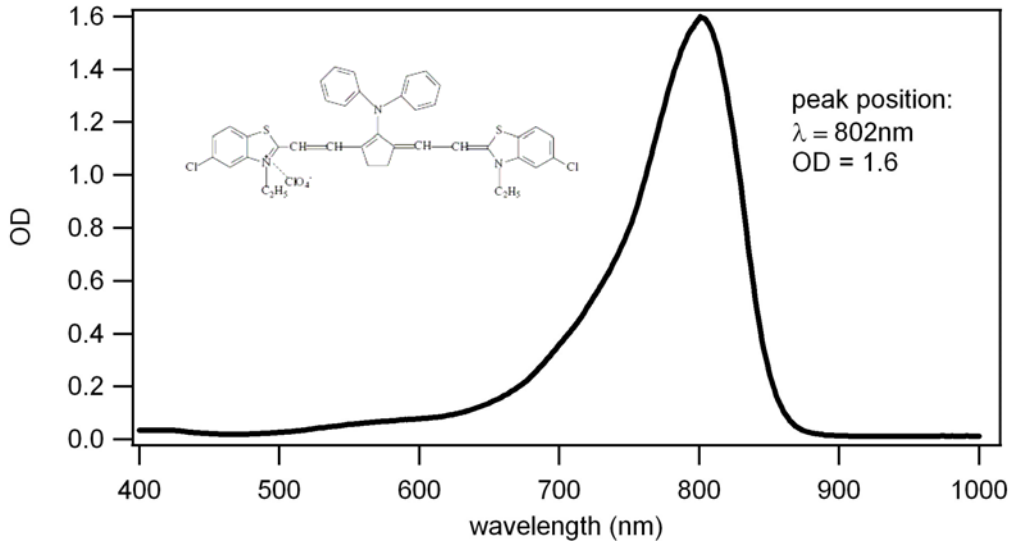


Fig. 2.6: Absorption spectrum of IR140 in MeOH. Its chemical structure is also reported. The cell used for this measure is 1 mm thick.

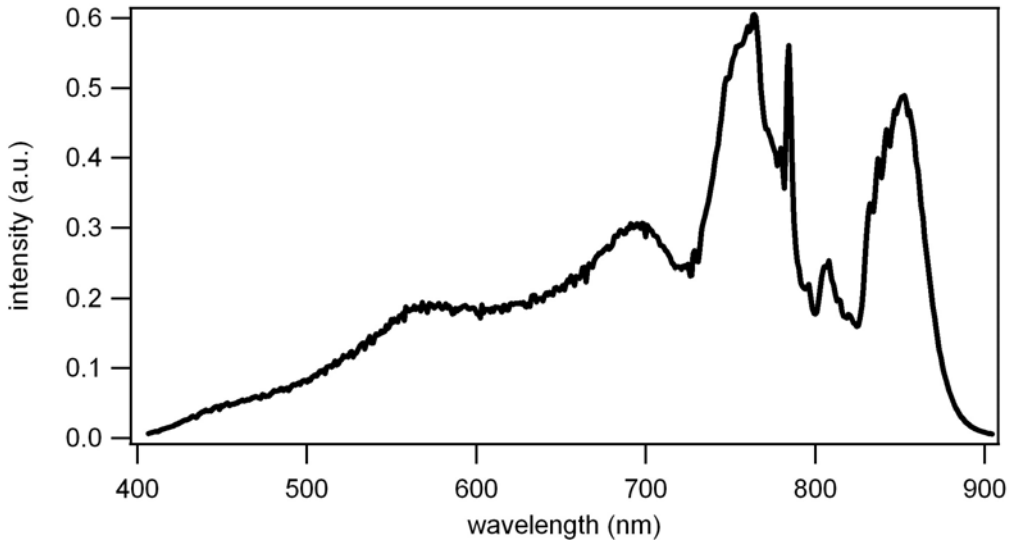


Fig. 2.7: White light spectrum used in pump-probe measurements.

2.6 Pump and probe pulses characterization

In order to obtain measurements with good time resolution and high signal-to-noise ratio, sample should be placed in a plane where the foci of the pump and probe beams overlap, while the diameter of the former must be larger than diameter of the latter. To verify this, the beam profiles are detected with a charged-couple-device camera (CCD) and in Fig. 2.8 the gaussian profiles of the two beams are reported. For the probe beam the dimensions are estimated to be Δx ~70 μm and Δy ~60 μm, while for the pump beam they are Δx ~150 μm and Δy ~130 μm.

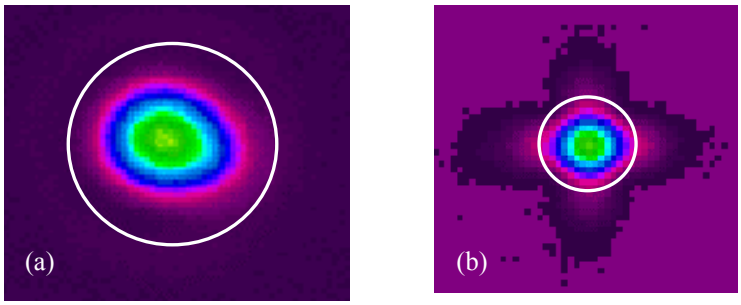


Fig.2.8: (a) Pump beam profile (Δx~150μm and Δy~130μm) (b) Super continuum probe beam profile (Δx~70μm and Δy~60μm)

For this measurement supercontinuum has been focalized with a f = 250 mm spherical mirror (SM2 in Fig.2.4), whereas in pump-probe measurements we used f = 150 mm mirror (SM3 in Fig. 2.4). We can estimate the actual dimension of the beams considering the relation between the beam diameter and the focal length:

$$d = \frac{4\lambda f}{\pi D} \quad , \qquad (2.4)$$

where d is the diameter of the beam at focus, λ is the wavelength of the beam, f is the focal length and D is the diameter of the beam diameter. Considering d is 65 μm, for f = 250 mm, we obtain d~40 μm for 150 mm.

To characterize the instrument time resolution it is necessary to measure the cross-correlation function between the pump and the probe pulses. This is achieved by

measuring the third harmonic of the Ti:Sa laser, generated by a type-I BBO crystal placed at the sample position. To generate the third harmonic is necessary that the two pulses overlap in space and time. To set the time zero, first the pump-probe signal of a dye (Rhodamine 6G) with a long excited state decay is found and then the sample is replaced by a BBO crystal. At this point a scan in time is made and the third harmonic intensity is measured by a photodiode array. The cross-correlation curve is fitted with a Gaussian. From the FWHM of the cross-correlation curve it is possible to estimate the time-width of the longer of the two pulses [57]. This value is ~ 61 fs.

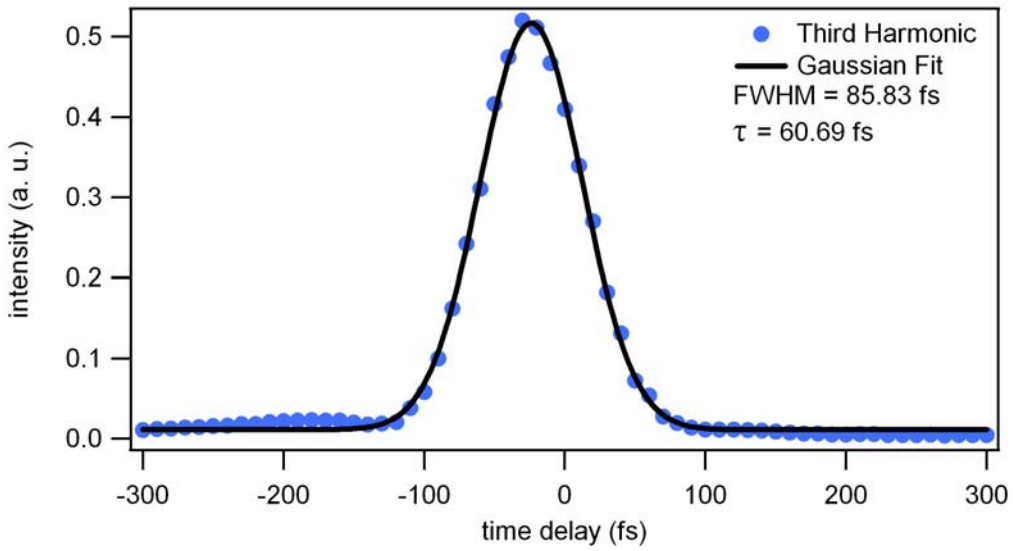
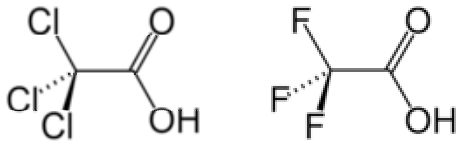


Fig. 2.9: Cross-correlation function of the pump and the probe beam. The pulse temporal length is obtained by dividing the FWHM by $2^{1/2}$.

2.7 Experimental procedures

The n-butylamine Schiff base of all-trans retinal is prepared according to previously described method [5] and protonated by using a 3-5 fold excess of trichloracetic (TCA) or trifluoroacetic (TFA) acid (their chemical structures are reported in Fig. 2.10). The former is used in the steady-state measurements in MeOH, while the latter is used in other measurements. The protonation with TFA is necessary in ACN since in this solvent TCA produces unstable PSBR at the room temperature [44]. Previous measurements do not show any change in excited-state dynamics when protonating acid (i.e. counterion) is changed. The pure dried solvents were used as received. Steady state absorption spectra are recorded in a spectrophotometer (Ultrospec 3000). The absorption maximum is at 444 nm in MeOH and 450 nm in ACN. The different peak positions are due to the slight difference in polarity between two solvents. The OD measured in a 1 mm thick cell is 0.3-0.7 at the peak position (Fig. 2.11).



(a) **CCl_3COOH** (b) **CF_3COOH**

Fig. 2.10: chemical structure of (a) trichloracetic (TCA) and (b) trifluoracetic (TFA) acid.

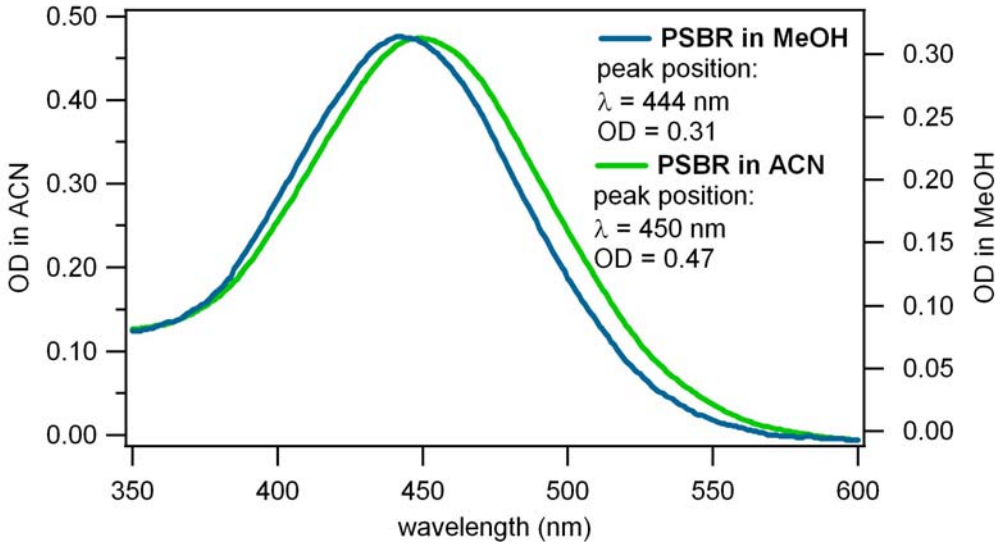


Fig. 2.11: absorption spectrum of PSBR in ACN (green) and MeOH (blue). The cell used for this measure is 1 mm thick.

For both the steady-state and the pump probe measurements it is necessary first to align and calibrate the two PDAs. This alignment implies that at pixels having the same index number on the two PDAs should be assigned to the same wavelength. Absolute calibration is done by using a crystal of $YAlO_3$ whose transmission spectrum contains many peaks with known wavelengths.

After a measurement of the background signal, in which the probe beam remains blocked by a shutter, the reference and the probe signal are made to pass through the $YAlO_3$ crystal put at the sample position. Then, the PDAs are slowly translated in the vertical direction until the two spectra overlap. At this point, the PDAs are aligned and the crystal is removed. The SC spectra are normalized and it is verified that the ratio between them is ~1. Then the crystal is put again at the sample position, but this time only the probe beam passes through it. A transmission spectrum is taken, compared with the reference spectrum and a graph with pixel index on x-axis and wavelength on y-axis is constructed. Fitting these data we obtain the wavelength calibration parameters (Fig. 2.12).

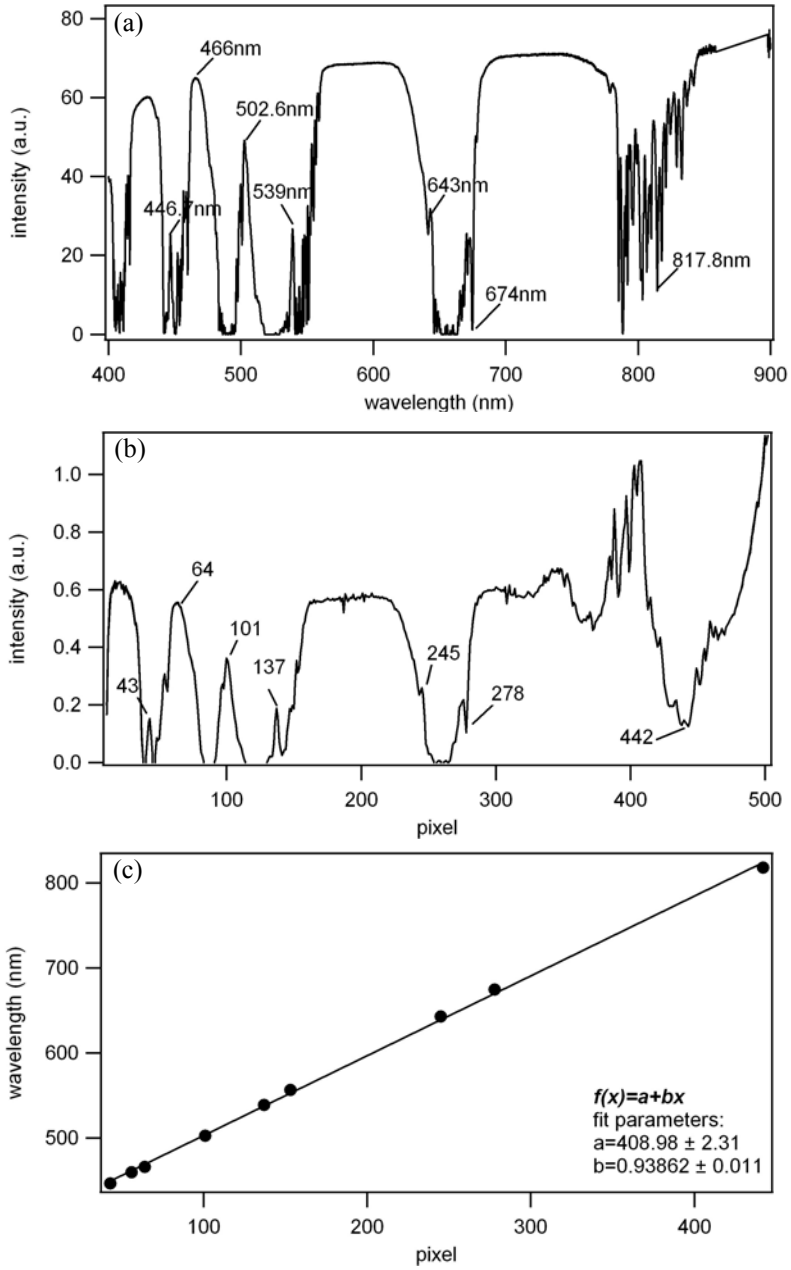


Fig. 2.12: Comparison between the reference transmission spectrum of $YAlO_3$ (a) and the measured spectrum (b) . In the last figure (c) there is the fit that gives us wavelength calibration parameters of PDA.

For the steady-state measurements, as reported in the description of the set-up, the light coming from a halogen lamp is used to excite the sample. The wavelength (400 or 540 nm) is selected with a monochromator and for every measurement the beam intensity is regulated varying the voltage on the power supply of the lamp. The probe beam is adjusted to reside in the centre of the excitation beam rectangle and both beams illuminates the central area of the flow cell (Fig.2.3). Before starting a scan, the probe and the reference spectra are normalized with the flow cell containing only the solvent. To minimize isomerization due to the photons coming from the probe beam a shutter is put in the probe beam so that measurement of each data point lasted <500 ms. In this way the number of absorbed photons originating from the excitation beam exceeded at least 20 times those originating from the probe beam. For each scan the cell was filled with a fresh sample (>90% all-trans) using the peristaltic pump. Subsequently, flexible tubings (silicon or Tygon, Masterflex) leading into and out of the flow cell were strongly pressed with a clamp to suppress any flow of the sample in the flow cell.
In the pump-probe measurements, approximately 25 ml of the PSBR solution is continuously flown through the flow cell using the peristaltic pump. Before starting a scan background signal in presence of the sample and the pump beam is taken. The solvent contribution to the signal was recorded by making a scan with the pure solvent. This measurement was also used to calculate the GVD correction (see paragraph 2.11).
All measurements are performed at ambient temperature and during the preparation, transport and measurements, a particular care is taken to screen the sample from the ambient light.

2.8 Data Acquisition

The transmission coefficient is defined by

$$T = \frac{I}{I_0} \quad , \tag{2.5}$$

where I is the intensity of the probe pulse after passing through the sample and I_0 is the beam intensity before the sample. In our particular case I_0, after the normalization of the probe to the reference beam, has an intensity comparable to that of the reference beam. The optical density, OD, (absorption coefficient), is defined by,

$$OD(\lambda) = -\log(T) \quad . \tag{2.6}$$

In the steady-state experiment we have performed, the OD of the sample is measured in time intervals that are, initially, few seconds long, but reaching several minutes at the end of the measurements. This is due to the fact that the process becomes slower for longer time of exposure since a large part of the molecules are already isomerized. Depending on the excitation intensity, a complete scan takes from 10' to 45' until the steady-state condition is achieved. The final measurement consists of a set of 130-150 data points.

In the pump-probe experiment we measure the perturbation induced by the pump pulse. This can be quantitavely expressed by the relative differential transmission coefficient ΔT/T, defined by:

$$\frac{\Delta T}{T} = \frac{T_p - T_u}{T_u} = \frac{\left(\frac{I_p}{I_{0,p}} - \frac{I_u}{I_{0,u}}\right)}{\frac{I_u}{I_{0,u}}} \quad , \tag{2.7}$$

where I_p and I_u are the probe beam intensity after the sample with and without the presence of the pump beam, respectively, while the subscript *0* indicates the initial intensity of the probe beam. The intensity of the reference beam $I^R_{0,p}, I^R_{0,u}$ is proportional to $I_{0,p}, I_{0,u}$ (i.e. $I_{0,p} = CI^R_{0,p}, I_{0,u} = CI^R_{0,u}$). Thus the relative variation of transmission results:

$$\frac{\Delta T}{T} = \frac{\frac{I_p}{I_{0,p}}}{\frac{I_u}{I_{0,u}}} - 1 = \frac{\frac{I_p}{C \cdot I_{0,p}^R}}{\frac{I_u}{C \cdot I_{0,u}^R}} - 1 = \frac{\frac{S_p - B_p}{S_p^R - B_p^R}}{\frac{S_u - B_u}{S_u^R - B_u^R}} - 1 \quad , \qquad (2.8)$$

where S is the signal measured with the probe beam open, B is the background signal when the probe beam is closed, superscript R denotes the reference PDA and subscripts p and u denote presence (pump) or absence (unpumped) of the pump pulse, respectively. In practice, for every time delay, the reference (S_p^R, S_u^R) and signal (S_p, S_u) spectra are acquired by the two PDAs and the $\Delta T/T$ coefficient is calculated in real time. Sorting of the pump and unpumped spectra is made using a photodiode that detects the pump beam after the chopper. The use of two synchronized PDAs permits us to have a signal to noise ratio of 10^{-4}.

The system can acquire each laser shot and then the SC intensity is mediated over an user-selected number of laser shots. However, since in our case the signal is very low, four shots at a time are accumulated to have a better signal on the PDAs. The measure is repeated 500 times and averaged out. This means that, since the repetition rate of the laser system is 1 kHz and since we have four shots pumped and four unpumped for every spectrum, we need 4 seconds for every time delay.

In a scan ~250 time delays between pump and probe is considered, from –300 fs to 50000 fs. The zero position is fixed at the time delay where a signal begins to appear. This is only indicative as the zero position will be determined after the data fitting. The interval between two consecutive time delays is 5 fs for the first 1000 fs and then the duration of the interval is progressively increasing up to 500 fs for the last 40 ps. This is because the decay of the excited state is slow [4], while a large number of points is not necessary. A complete measure, consisting of 5 consecutive scans, has a typical time duration of ~90 min.

2.9 An example: Rhodamine 6G

To optimize the system few tests with the dye Rhodamine 6G, were performed. Its intense and narrow absorption peak and its long living excited state make this molecule a suitable sample for signal optimization. An absorption spectrum of our solution of Rhodamine6G in ethanol is reported in figure 2.14. The peak is at 529 nm and OD is ~1.9 (value obtained in a spectrophotometer with a 1 mm thick cell).

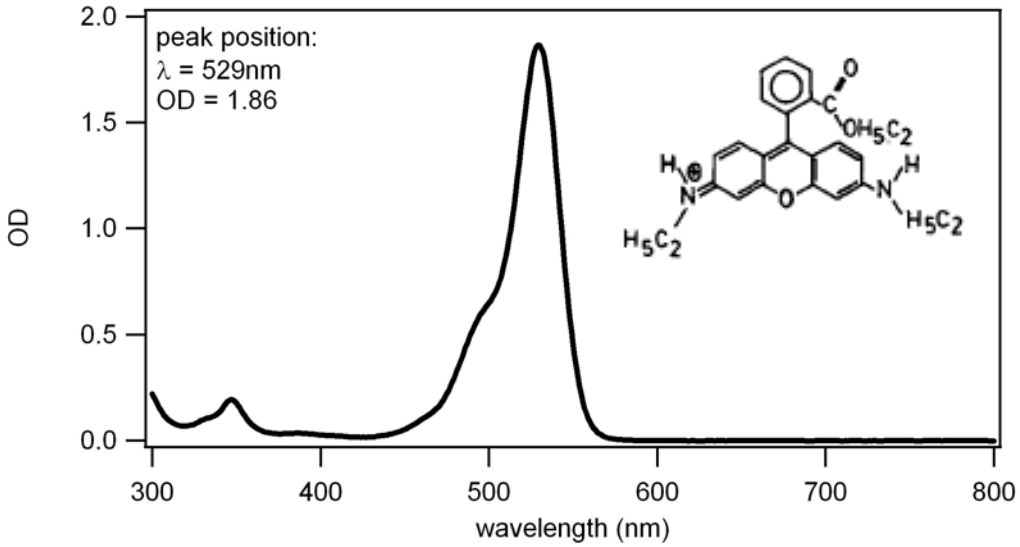


Fig. 2.14: Absorption spectrum of Rhodamine6G in ethanol. Its chemical structure is also reported. The cell used for this measure is 1 mm thick.

To avoid contribution of multiphoton processes the linear response of the system with the pump power is verified. This measurements are important because they are related to the pump intensity used for the experiments with PSBR. The spectra are taken at a time delay of 250 fs, where the contribution of the stimulated emission is visible. The results are reported in Fig. 2.15. in this figure it can be noted that the sample response is linear up to a pump power of ~200 μW.

A kinetic trace at 560 nm is reported in Fig. 2.16. After few tens of femtoseconds, stimulated emission decays slowly, on the order of ~4 ns nanoseconds [58], so that the fast fluctuations of $\sim 10^{-3}$ ΔOD in intensity can be assigned to noise in our experiment.

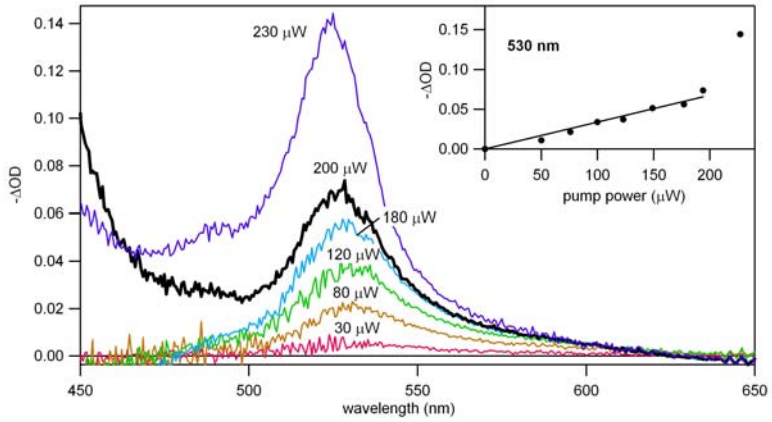


Fig 2.15: Spectra of Rhodamine6G taken with different pump power and at a time delay of 250 fs. Inset: Intensity of the peak vs pump power. The sample response is linear until ~200μW of pump power.

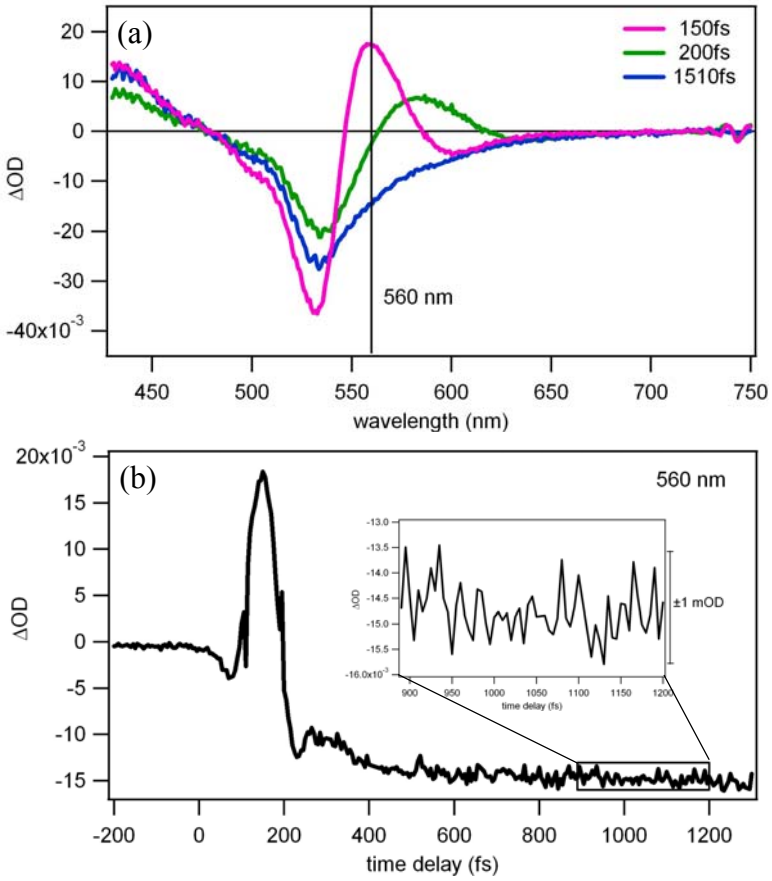


Fig. 2.15: (a) spectra taken at different time delay; (b) a kinetic trace at 560 nm. Pump power ~ 100μW.

2.10 Cross Phase Modulation (XPM)

Pump-probe experiments on liquid-phase samples are characterized by some artefacts arising from the high pump intensity. This artefacts are comprehensive of multiphoton absorption, stimulated Raman scattering by the solvent or by the fused silica windows of the sample flow cell, etc. However, the most important is the so called "Cross Phase Modulation" (XPM). This artefact consists in a modulation of the real part of the refractive index of the medium in a time-dependent way so that spectral changes in the white light continuum used as a probe can be detected when pump and probe overlap in time. The total energy of the probe remains constant but it is redistributed over different frequencies. The XPM occurs even when the medium is completely transparent , since it can arise either from the solvent or the fused silica flow cell, being this last effect usually dominant

In the past some models about the XPM effect have been proposed [50, 51, 52], but the most complete description is reported by Ekvall et al. [53]. These authors reproduced the experimental signals by numerically solving the following set of coupled wave propagation equations describing the non-linear coupling between the probe and the pump:

$$\frac{\partial A_{pump}}{\partial z}+\frac{1}{v_{g,pump}}\cdot\frac{\partial A_{pump}}{\partial t}=i\frac{\omega_{pump}}{c}\frac{n_2}{2}\left|A_{pump}\right|^2 A_{pump}\,, \tag{2.9}$$

$$\frac{\partial A_{probe}}{\partial z}+\frac{1}{v_{g,probe}}\cdot\frac{\partial A_{probe}}{\partial t}+\frac{i}{2}\beta^{(2)}_{probe}\frac{\partial^2 A_{probe}}{\partial t^2}-\frac{1}{6}\beta^{(3)}_{probe}\frac{\partial^3 A_{probe}}{\partial t^3}=$$

$$=i\frac{\omega_{probe}}{c}\frac{n_2}{2}\left|A_{pump}\right|^2 A_{probe} \tag{2.10}$$

where A_i, ω_i are the amplitude and the frequency of the electromagnetic field of the pump and the probe beams respectively, $v_{g,pump}$ and $v_{g,probe}$ represent the group velocities of the pump and probe pulses; $\beta^{(2)}_{probe}$ and $\beta^{(3)}_{probe}$ correspond to the second and third order dispersion coefficients of the probe pulse that can be

calculated from the Sellmaier equation for fused silica and that are included because the pump has a very wide frequency spectrum. Finally n_2 is the non-linear part of the refractive index $n(z,t,\omega)$ that, including all the dependences can be written as:

$$n(z,t,\omega) = n_0(\omega) + \frac{n_2(\omega)}{2}\left|A_{pump}(z.t)\right|^2 . \qquad (2.11)$$

The right hand terms in Eqs (2.9) and (2.10) describe the self-phase modulation of the pump and the XPM of the probe induced by the pump, respectively. The self-phase modulation of the probe and the XPM of the pump induced by the probe are neglected since probe pulse are at least two order of magnitude weaker than the pump pulses. Other contributions, like Raman Scattering or self-steeping – a change in the shape of light pulses, due to propagation in a medium with an intensity-dependent index of refraction [59] – are expected to be small [60, 61].

In their calculations Ekval et al. [53] assumed that the initial amplitude of the pump pulse can be accurately described by a transform limited Gaussian function. The description of the probe pulse is more difficult because of the complexity of the self-phase modulation process. In any case, in the wavelength range 400 nm - 700 nm [53] the continuum can be well represented by a linearly chirped Gaussian beam.

Solving numerically Eqs. (2.9) and (2.10), we obtain the temporal profile of the initially linearly chirped probe pulse after its propagation through the sample in the presence of the pump. Than, the spectrum $S^l_{probe}(\Delta t,\omega)$ of the probe pulse after the sample is obtained from the Fourier transform of the temporal profile. At the same time the pump-probe signal can be calculated if we consider that the spectrum of the reference pulse is simply the spectrum of the probe $S^0_{probe}(\omega)$ before entering the sample. These two quantities, $S^l_{probe}(\Delta t,\omega)$ and $S^0_{probe}(\omega)$, can then be used to calculate a theoretical value for ΔOD defined in eq. 2.2.

This model predicts the measurements very well as it is shown in Fig. 2.16 and 2.17., where the changes in optical density are displayed as a function of the time delay between pump and probe pulses for the representative wavelengths of the SC probe. In Fig. 2.16 a comparison between theoretical and experimental time traces from a study of Ekvall et al. [53] is reported while Fig. 2.17 shows our measurements. Our traces are different from the traces in literature since the flow cell used has an overall glass thickness of 2.5 mm versus 1 mm and in addition also 0.5 mm of solution is present in our case. Nonetheless, the major behaviour observed by Ekvall et al. [53] are also observed in our case, while increasing the wavelength difference between the probe and the pump pulse can be detected. In particular,

1. *changes in dispersion shaped features and broadening of the signal.* This is a result of the group velocity mismatch between the pump and the SC probe ($v_{g,pump}$, $v_{g,probe}$). We also have to consider the influence of dispersion inside the sample on the SC probe due to its broad spectrum. At shorter wavelengths respect to the central part of the SC, i.e. 550 nm for Ekvall et al. [53] and 650 nm in our experiment, the dispersion reduces the effect of the group velocity mismatch. At 425 nm, the dispersion features almost overlap and the resulting signal has a defined shape. At longer wavelengths with respect to the central continuum wavelength, the dispersion enhances the effect of the group velocity mismatch, and at 650 nm the dispersion features are almost separated resulting in a broadening of the signal;
2. *the positive maximum of the oscillatory feature in each of the curves shifts to more positive delay times*. Since the response of the sample is instantaneous, signal is only generated, while the pump and probe pulses overlap in time. Because of the positive chirp ($b_{probe}>0$) of the continuum, red wavelengths of the probe arrive at the sample before blue wavelengths. Since positive Δt corresponds to pump pulses that arrive at the sample before the probe, the overlap between the pump and the probe (and thus the appearance of the

signal), is shifted toward larger delay times for probe wavelengths further in the red;

3. *the amplitude is decreasing.* A factor contributing to this is the velocity mismatch between the pump and probe. At 425 nm or 470 nm, the walk-off between pump and probe is minimal and for these wavelengths the probe overlaps with the pump throughout almost the whole 1 mm thick sample. This means the pump-induced phase modulation, and consequently the signal, is large. For wavelengths further to the red, the signal amplitude is reduced since pump and probe are overlapped only in limited volume of the sample.

The good agreement between theory and experiment indicates that the XPM signal may be useful for characterizing the chirp of supercontinuum. In fact, the time zero for each wavelength in the continuum probe can be obtained from the positive maximum of the XPM signal of a flow cell filled with pure solvent [52]. This method works well when the total thickness of the sample (windows+solvent) is small, because in a thick sample the XPM-related signal has a tendency to split into two separate dispersion- shaped feature and this precludes a definition of a unique time zero for each individual probe wavelength. Nevertheless, in many cases the splitting will only be partial and, taking into account experimental noise, this problem may go unnoticed.

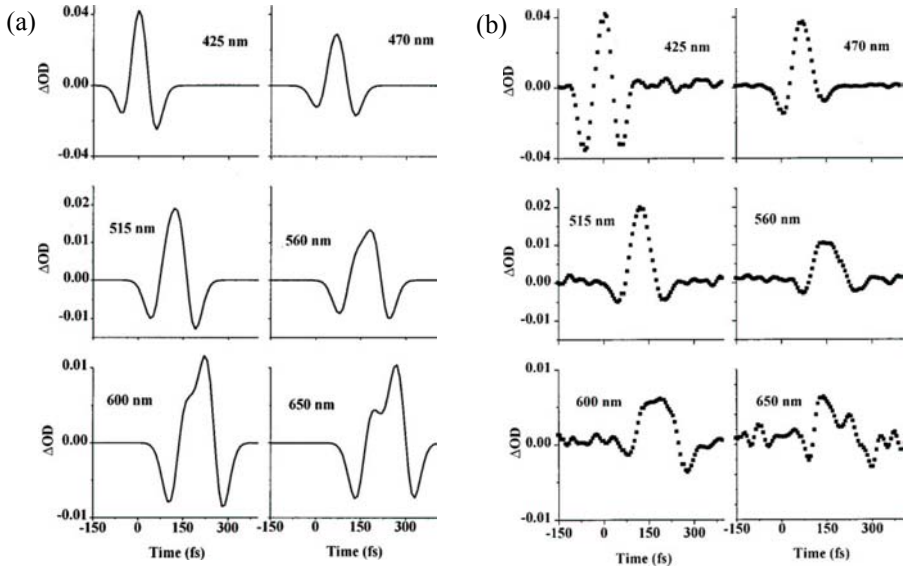


Fig. 2.16: Pump induced change in optical density as a function of time delay between pump and probe pulses for six wavelengths between 400 and 700 nm. The signal is obtained for a 1 mm thick fused silica plate, which mimics the entrance window of a typical commercial flow cell. The pump wavelength is 400 nm while the supercontinuum is cantered at 550 nm.(a) theoretical (b) experimental .[53]

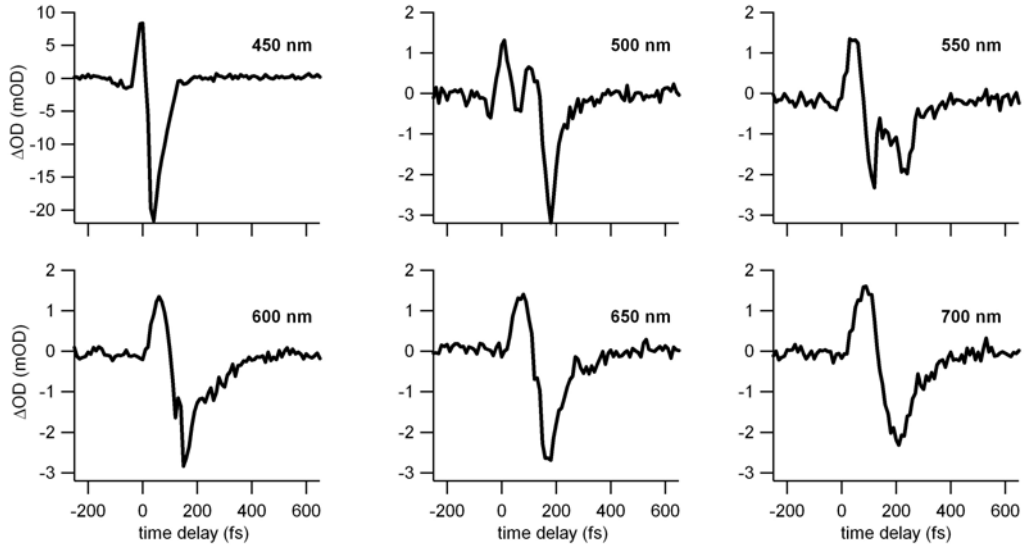


Fig. 2.17: experimental pump-probe signal obtained in our system, for quartz flow cell (2.5 nm thick) filled with solvent (MeOH). The pump wavelength is 400nm while the supercontinuum is cantered at 650 nm.

2.11 GVD correction

The GVD correction is calculated as in ref. [52] following the position of the first positive maximum of XPM signal of the cell-solvent system. The effect of the glass is considered to be dominant, since there is only 0.5 mm of solvent layer versus 2.5 mm of glass, so only measurements with MeOH are used. In Fig. 2.18 the time position of the XPM peak at different wavelength are reported and the data are best fitted with a power law function:

$$\Delta t = t_0 + a\lambda^b \quad , \tag{2.12}$$

from which the GVD correction curve is obtained.

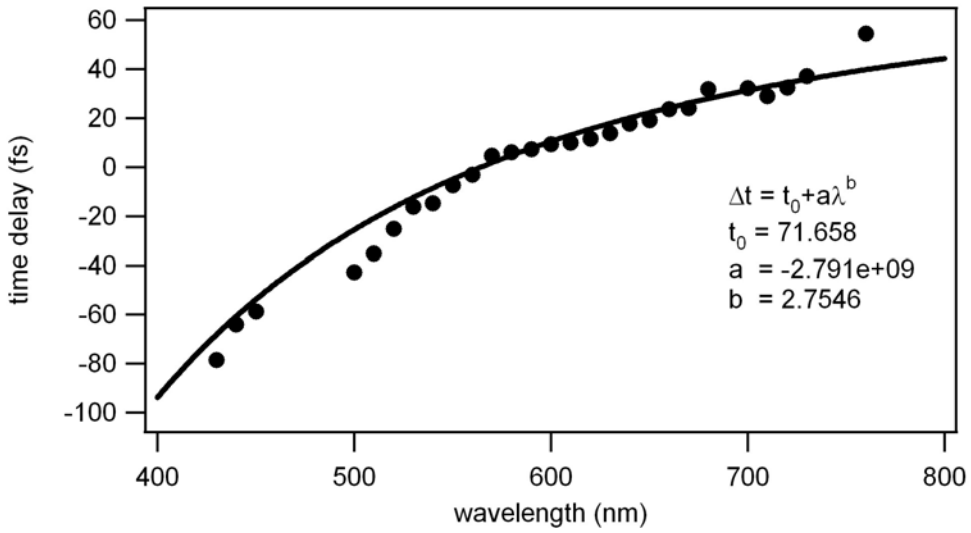


Fig. 2.18: GVD correction curve. The points represents the XPM peak position in time.

In Fig. 2.19 the image plot of the measurements are shown. The first is related to the pure solvent case (MeOH), while in the other two PSBR in MeOH and ACN are considered. For the images without correction, the effect of GVD can be easily noticed, with the red components that arrive after the blue ones.

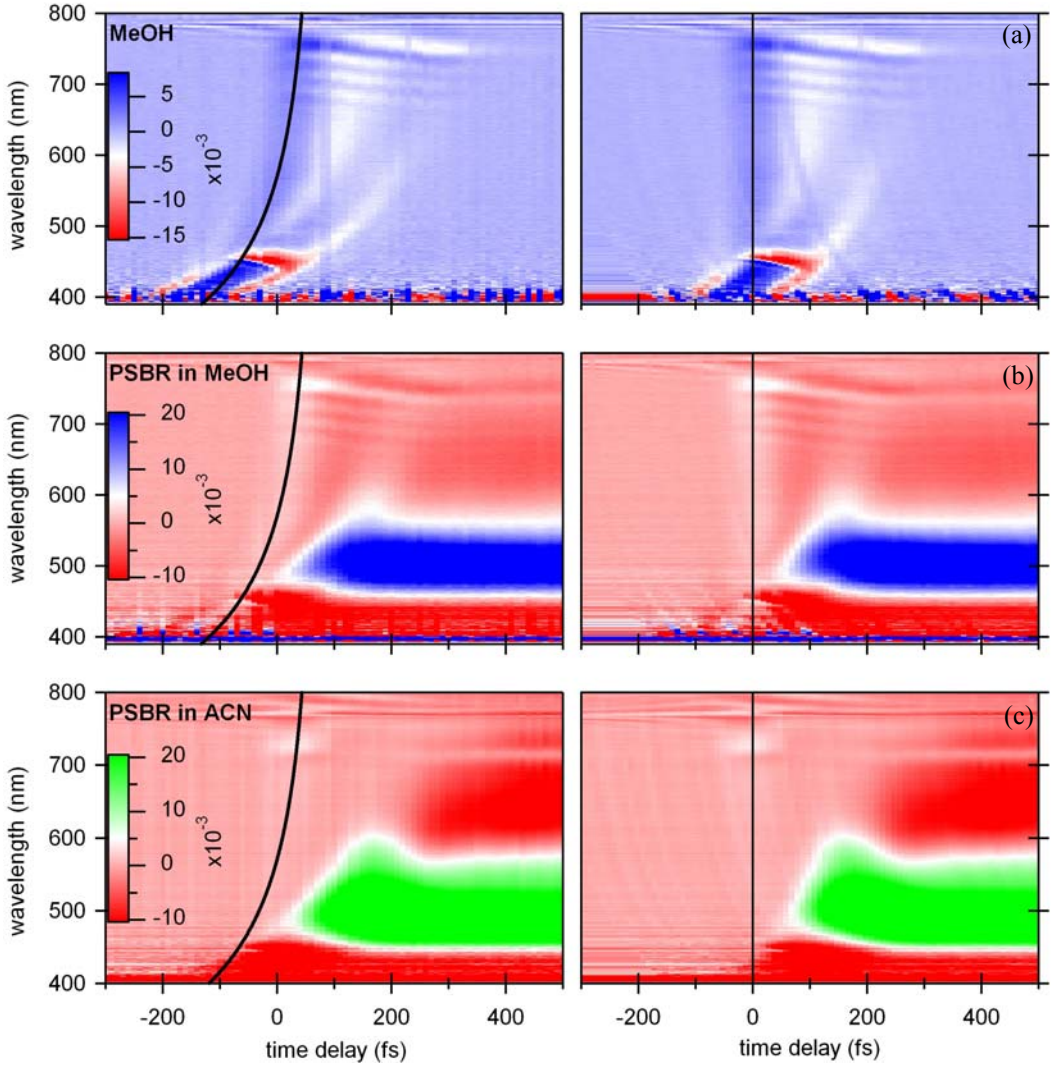


Fig. 2.19: image plot of the pump-probe signal (ΔOD) not corrected (left) and corrected (right) for GVD. (a) pure MeOH; (b) PSBR in MeOH; (c) PSBR in ACN. Pump power of ~90 μW is used for all measurements.

2.12 Subtraction of solvent contribution

Before starting the analysis, the background noise determined for t < 200 fs is removed and the data are corrected for the GVD. In the case of PSBR in MeOH it was also possible to subtract the XPM solvent contribution. This was impossible in the case of ACN since the measurements of the pure solvent and those of the sample were not performed the same day. The slight differences in system condition and in time zero from one day to the other make the subtraction highly problematic. To verify that subtraction can be done, we consider the region around 700 nm for the early time delays (Fig. 2.20). We choose this region since stimulated emission shows a ~ 150 fs rise, therefore making the solvent contribution the most prominent. Normalization of the signal is not necessary since for the two measurements the same pump power (~90 μW) is used and a good superimposition in spectra and kinetic traces can be seen. It is sufficient to subtract the two matrices to obtain the clean PSBR signal. An example of the data matrices before and after subtractions is reported in Fig. 2.22. In this data set the time zero is not corrected yet.

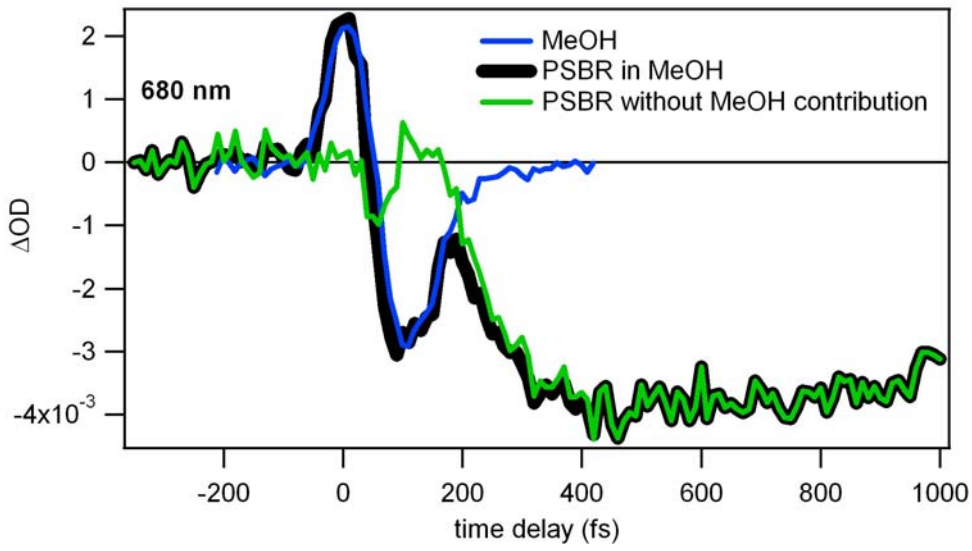


Fig. 2.20: Kinetic traces at 680 nm of the pure solvent, the PSBR in MeOH and the pure PSBR signal after the subtraction of the solvent contribution. It can be seen that the solvent signal (blue) and the sample signal (black) overlap perfectly.

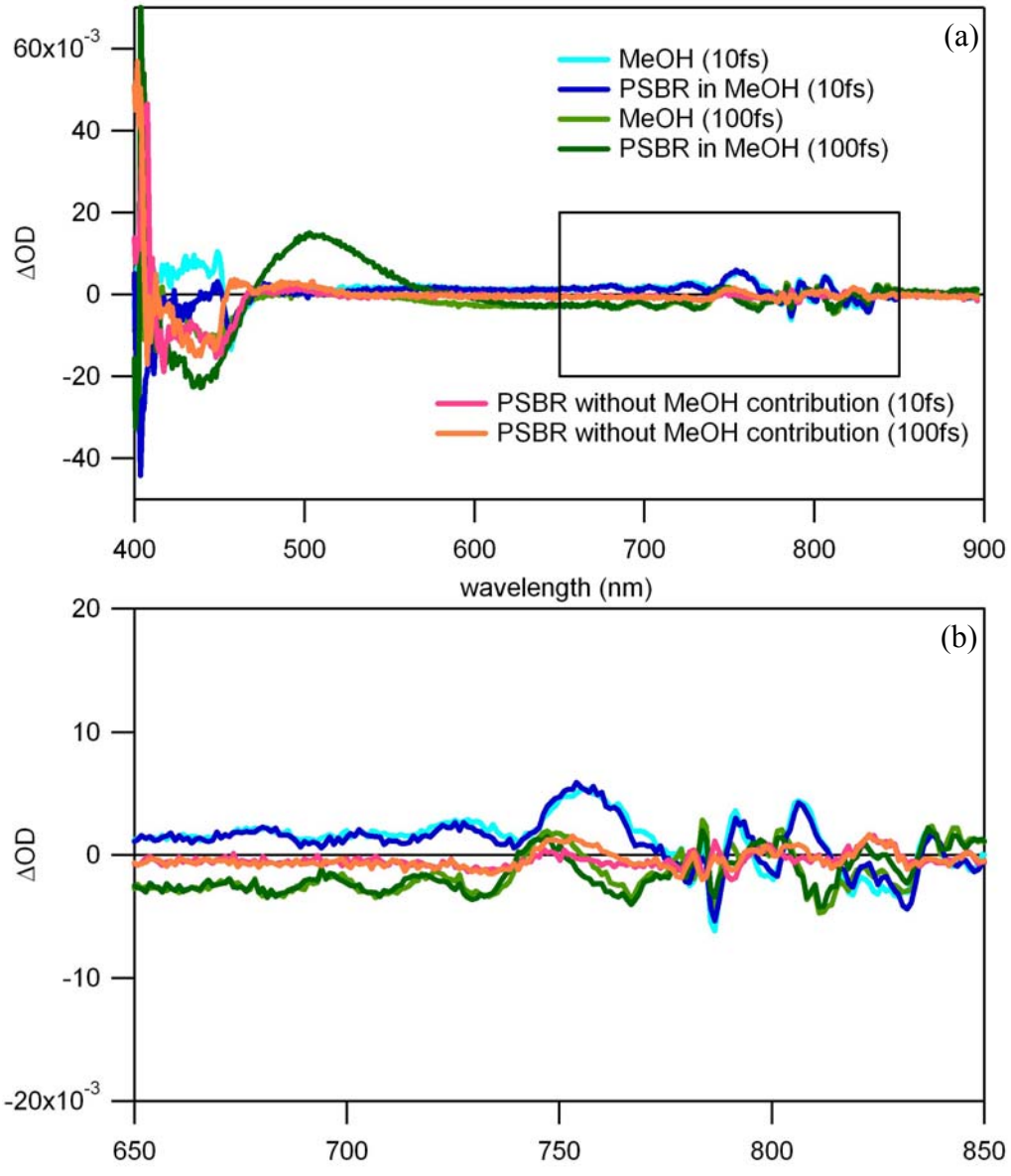


Fig. 2.21: spectra of MeOH, of the sample and after the subtraction. In figure (b) the region around 700 nm is enlarged. In this region only the solvent contribution is visible, since SE appears later. Also in this case it can be observed that signals of pure solvent and of PSBR overlap.

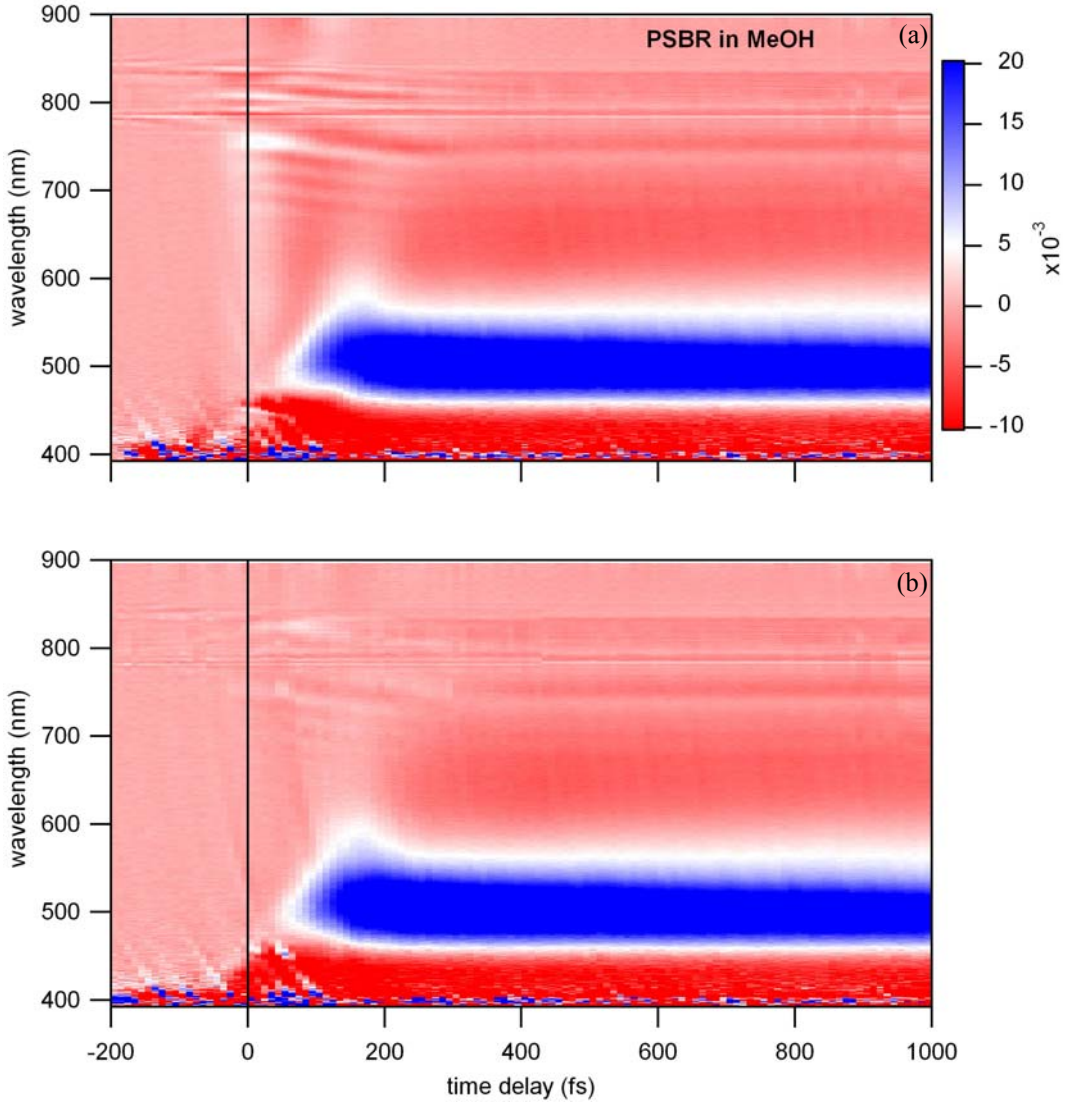


Fig. 2.22: Image plot of pump-probe signal (ΔOD) before (a) and after (b) the subtraction of MeOH contribution.

2.13 Pump-probe data analysis technique

The dataset of a pump-probe experiment is a three-dimensional plot having wavelength and time as independent variables and differential absorption intensity as a dependent one. The fact that pump-probe data are 3D-data set creates problems with their presentation and interpretation. In fact the 3D representation using surface plot or 2D image, where the third dimension is represented by a colour scale, is not so useful. A better choice is to consider only two dimensions presenting the spectra at selected times and kinetic traces at selected wavelengths, but in this way we loose a dimension and the majority of data is omitted from the presentation. A simultaneous analysis, "global analysis", of all dataset is needed to separate information from stochastic noise, and to verify different dynamical scenarios by simultaneous fitting of all data [62, 63, 64]. To achieve this, singular value decomposition (SVD) is used.

Consider a $m \times n$ matrix $M(t_i,\lambda_j)$ containing the transient absorption data as a function of a discrete set of time-delays t_i and wavelengths λ_j. Assuming additive noise, M can be represented by the sum

$$M = \tilde{M} + \Xi, \tag{2.13}$$

where $\tilde{M}$ contains the information about the spectral evolution of the system, and Ξ denotes a normally distributed stochastic disturbance with zero mean (the possible systematic errors are not included in this description). The SVD approach consists in decomposing M into the product of three matrices

$$M = USV^T \quad , \tag{2.14}$$

where U and V are orthogonal matrices of dimensions $m \times m$ and $n \times n$, respectively and their columns contain the left and right singular vectors. Considering the case of transient absorption data, we can identify the columns of U as basis time traces, and the rows of V^T as basis spectra. S is an $m \times n$ matrix and it is zero except in the diagonal, which contains the singular values $s_i = S_{ii}$.

In the case of a completely noise-free matrix, characterized by n linearly independent components, the number of non-zero singular values is equal to the

rank of the matrix n: $s_1 \geq s_2 \geq \ldots \geq s_n \geq s_{n+1}=0$. In the presence of noise, the singular values and the singular vector pairs $\{U_i, V_j^T\}$ are perturbed. Assuming that the noise is small in comparison to the signal, we can still discriminate between the singular vector pairs carrying dynamical information on the system, and those associated to noise. The number of linearly independent significant components, in fact, can be determined from the number of singular values which differ appreciably from the noise. Calling s_y the greatest singular value associated to the noise, a linear algebra theorem [62] ensures that the perturbation is negligible for all the vectors pairs with label i<y, such that $s_i - s_{i+1} >> s_y$.

As an example, in Fig. 2.23 the singular values extracted from the data set of PSBR in MeOH are displayed. It can be immediately observed that the first three values are distinct from the others and they are supposed to be associated to the most prominent spectral and kinetic information of the data set.

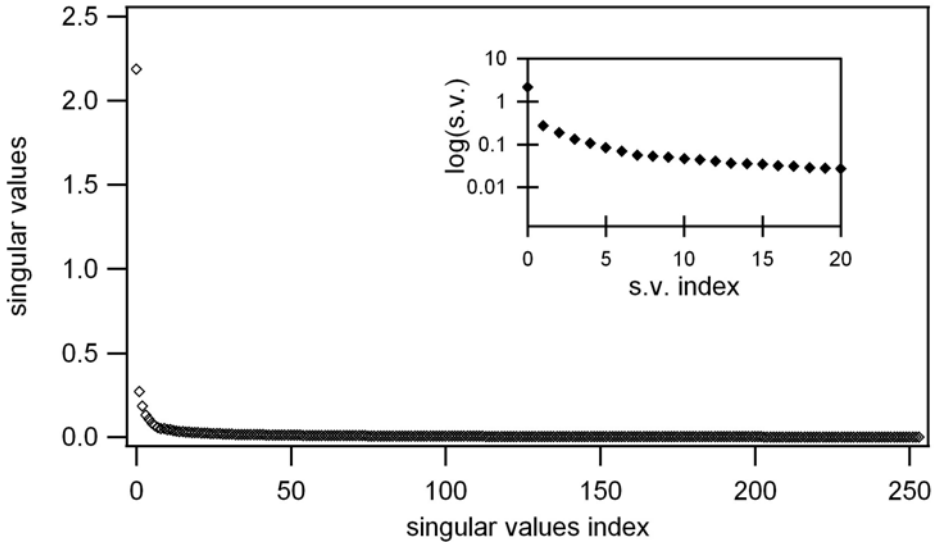


Fig. 2.23: Singular values obtained applying the decomposition of eq. 2.14 on the dataset of PSBR in MeOH. Inset: the first part of the graph is enlarged and reported in logarithmic scale. The significant components retained for the analysis are the first three.

The basis time traces U_i and spectra V_j^T identified by this procedure in general are not associated to any specific species or dynamics. The physical information of

interest should be extracted constructing linear combinations of these orthogonal vectors through appropriate kinetic models. If we suppose that the kinetic response of a system can be described by the sum of K functions:

$$\sum_{k=1}^{K} f_k \quad , \tag{2.15}$$

we can try to fit simultaneously all the N significant time-traces U_i retained from the SVD analysis. In our case the time-resolved transient absorption-traces spectra are fitted by a sum of K exponential function convoluted with a Gaussian and a step function.

The coefficients $c_{i,k}$, obtained by the fitting,

$$U_i \cong \sum_{k=1}^{K} c_{i,k} f_k \,, \tag{2.16}$$

can be used to calculate the spectra T_k associated (Decay Associated Spectra - DAS) to different kinetic components present in the dynamics:

$$T_k = \sum_{i=1}^{N} s_i c_{i,k} V_i^T \quad . \tag{2.17}$$

These spectra show the amplitude of each kinetic component playing a visible role in the evolution of the system.

3. Results

In the first part results of the steady-state measurements are reported and the photoisomerization efficiency is calculated. In the second part a detailed analysis of the pump-probe data is reported.

3.1 Measurements of the photoisomerization efficiency

As anticipated in the introduction, determination of photoisomerization efficiency (Φ) using steady-state spectroscopy is based on the fact that the extinction coefficient of the PSBR drops by ~50% when the molecule goes from *all-trans* to *cis* isomer [32]. As a consequence, optical density (OD) of the sample decays in time due to increasing concentration of the *cis* isomer in PSBR solution during the exposure to light. The rate equations that describe the isomerization process can be written in the analytic form [65] if we consider that *all-trans* isomerizes only into 11-cis and vice-versa. Unlike the inverse isomerization from 11-cis to *all-trans*, from table 1.2 we can see that *all-trans* can isomerize also in 9-cis and 13-cis isomer, but these reactions can be neglected since they are an order of magnitude less efficient [3]. Thus, the number of the trans (N_{trans}) and *cis* (N_{cis}) isomers at time *t* can be described by the following rate equations:

$$\frac{dN_{trans}(t)}{dt} = -ph_{trans}(\lambda)\phi_{trans}(\lambda)N_{trans}(t) + ph_{cis}(\lambda)\phi_{cis}(\lambda)N_{cis}(t) \qquad (3.1)$$

$$\frac{dN_{cis}(t)}{dt} = ph_{trans}(\lambda)\phi_{trans}(\lambda)N_{trans}(t) - ph_{cis}(\lambda)\phi_{cis}(\lambda)N_{cis}(t) \quad , \qquad (3.2)$$

where $ph_{trans}(\lambda)$ and $ph_{cis}(\lambda)$ are relative photoexcitations of the trans and *cis* isomer, respectively. Relative photoexcitation is defined as percentage of molecules absorbing a photon at wavelength λ per unit time:

$$ph_{trans}(\lambda) = \sigma(\lambda)\frac{N_{photon}}{A} \quad , \qquad (3.3)$$

where N_{photon} is the number of photons arriving at surface A in unit time and $\sigma(\lambda)$ is the molecule cross section that can be calculated from the extinction coefficient $\varepsilon(\lambda)$ considering that:

$$\sigma(\lambda) = \ln 10\frac{\varepsilon(\lambda)}{N_A} \quad , \qquad (3.4)$$

where N_A is the Avogadro's number.

By solving Eqs. (3.1) and (3.2) we obtain the variation of absorbance $A(t)$ in time:

$$A(t) = \frac{c_0 l}{a+b}\left[(b\varepsilon_{trans}(\lambda) + a\varepsilon_{cis}(\lambda)) + a(\varepsilon_{trans}(\lambda) - \varepsilon_{cis}(\lambda))e^{-(a+b)t}\right] \quad , \qquad (3.5)$$

where c_0 is the initial concentration of the *all-trans* PSBR molecules, l is the thickness of the sample, and the coefficients a and b are defined as

$$a = ph_{trans}(\lambda)\phi_{trans}(\lambda) \qquad (3.6a)$$

$$b = ph_{cis}(\lambda)\phi_{cis}(\lambda) \quad . \qquad (3.6b)$$

From Eq. (3.5) it can be observed that the absorbance decreases exponentially with illumination time until it reaches the steady state condition when reaction rates of the *all-trans*→11-cis and the inverse process are equal. The decay constant τ is inversely proportional to $ph_{trans}(\lambda)$ and can be expressed as:

$$\tau = \frac{1}{a+b} = \frac{1}{ph_{trans}(\lambda)\left[\phi_{trans}(\lambda) + r\phi_{trans}(\lambda)\right]} = \frac{X}{ph_{trans}(\lambda)} \quad , \qquad (3.7)$$

where r corresponds to the ratio $\varepsilon_{cis}(\lambda)/\varepsilon_{trans}(\lambda)$ that is considered a constant value independent from λ since in previous studies of Becker and Freedman [31, 32] it was shown that the absorbance spectra of the *all-trans* and the 11-cis PSBR isomers practically does not differ in shape when normalized.

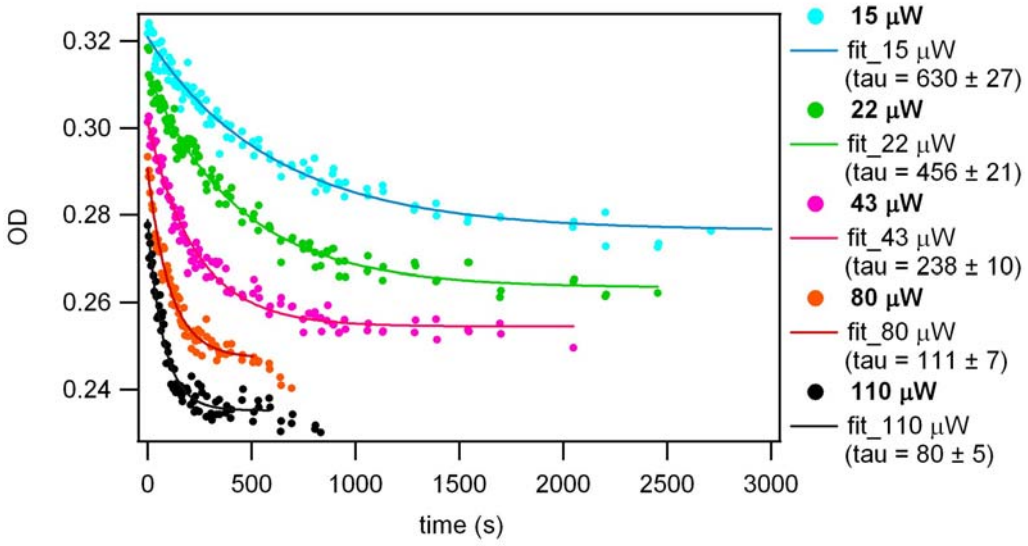


Fig 3.2: Optical density (OD) decay A(t) of PSBR in ACN at 450 nm for different excitation power and upon 400 nm excitation with corresponding exponential fits (solid lines) are also reported. From 80 µW to 15µW, the data are vertically shifted by 0.01, 0.02, 0.03 and 0.04, respectively.

The value of r is equal to 0.45 and 0.58 in MeOH and ACN, respectively. Fitting the $\tau(ph_{trans})$ function for various ph_{trans} values we obtain the constant of proportionality X and from this we can calculate the photoisomerization yield of the *all-trans* PSBR isomer:

$$\phi_{trans}(\lambda) = X^{-1} - r\phi_{cis}(\lambda) \quad . \qquad (3.8)$$

Here $\phi_{cis}(\lambda)$ values determined in previous HPLC experiments [31] have been used.

In Fig. 3.1 several OD decay curves $A(t)$ obtained with different excitation power are reported. By fitting the data with an exponential function we obtain the OD decay constant τ for various values of ph_{trans}. The experiment has been repeated for two excitation wavelengths (400 nm and 540 nm) and two solvents MeOH (Fig.2.a) and ACN (Fig.2.b). The maximum ph_{trans} value of ~5% has been limited by the intensity of our excitation source, whereas minimum value of ~0.3% has been imposed in order to avoid a dominant contribution of the probe beam

photons to the isomerization process. Since in our case both independent (τ) and dependent variables (ph_{trans}) contain uncertainties, we use Orthogonal Distance Regression (ODR), a fitting method that minimizes orthogonal distance from the data point to the fitted curve, to obtain the fit parameter X. Using Eq. (3.8) photoisomerization quantum yields $\phi_{trans}(\lambda)$ are calculated for the different excitation wavelengths and solvents (table 3.1).

	λ(nm)	**MeOH**	**ACN**
X	400	4.0±0.5	2.8±0.2
	540	3.2±0.1	2.9±0.4
$\phi_{trans}(\lambda)$	400	0.16±0.03	0.22±0.03
	540	0.20±0.02	0.23±0.06

Table 3.1: fitting parameters X and photoisomerization quantum yields $\phi_{trans}(\lambda)$ obtained from our measurements.

A slight increase (25%) of $\phi_{trans}(\lambda)$ is observed in MeOH when we pass from 400 nm to 540 nm while in ACN no dependence on the excitation wavelength has been detected. Comparing $\phi_{trans}(\lambda)$ for the excitation wavelength at 540nm, an increase of 15% is also observed when MeOH is substituted with ACN.

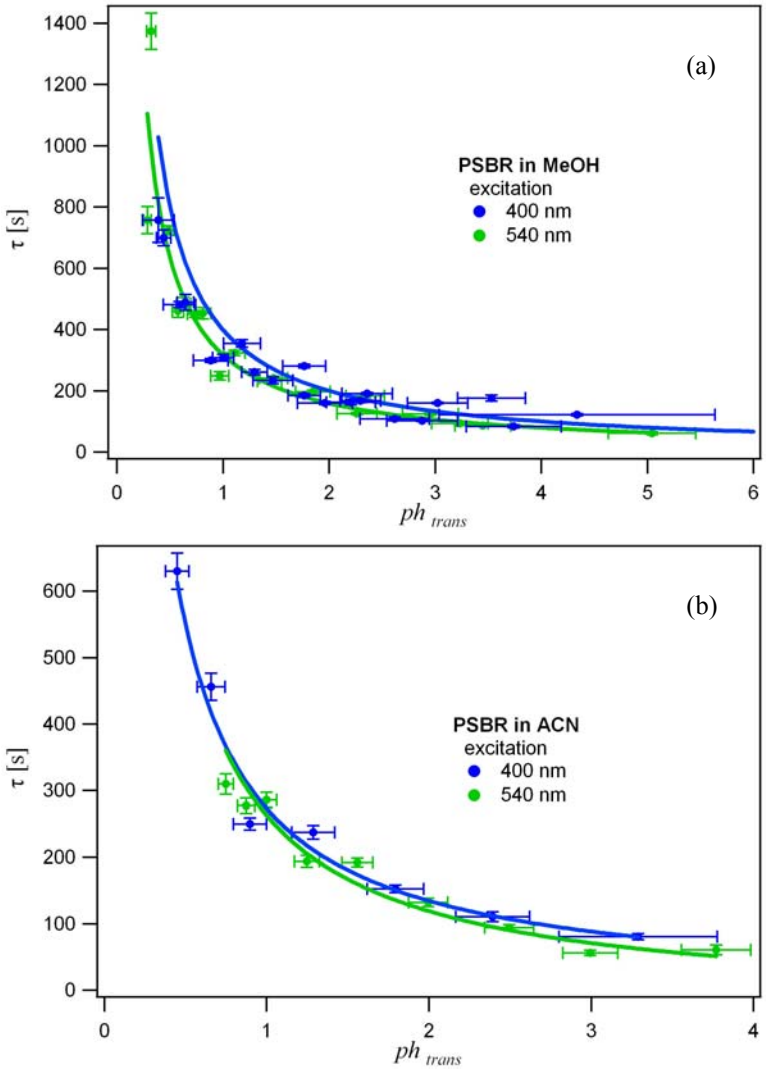


Fig. 3.2: Dependence of the OD decay constant τ on relative photoexcitation $ph_{trans}(\lambda)$ for PSBR in MeOH (a) and ACN (b) upon 400 nm (blue dots) and 540 nm (green dots) excitation. Data are fitted with a function of the form $f(x) = a/X$.

3.2 Results of pump-probe measurements

To avoid contribution of multiphoton processes to the pump-probe signal it is important to verify that the response of the sample is linear respect to the pump-power used. From the measurement with Rhodamine 6G we know that the excitation power of some tens of microwatt should be used. As in the case with the dye, at a fixed time delay several spectra with different pump power are taken. Then, the peak intensity in function of the pump power is plotted (Fig. 3.3), where it can be seen that the maximum power that stays in the linear regime is ~100 μW.

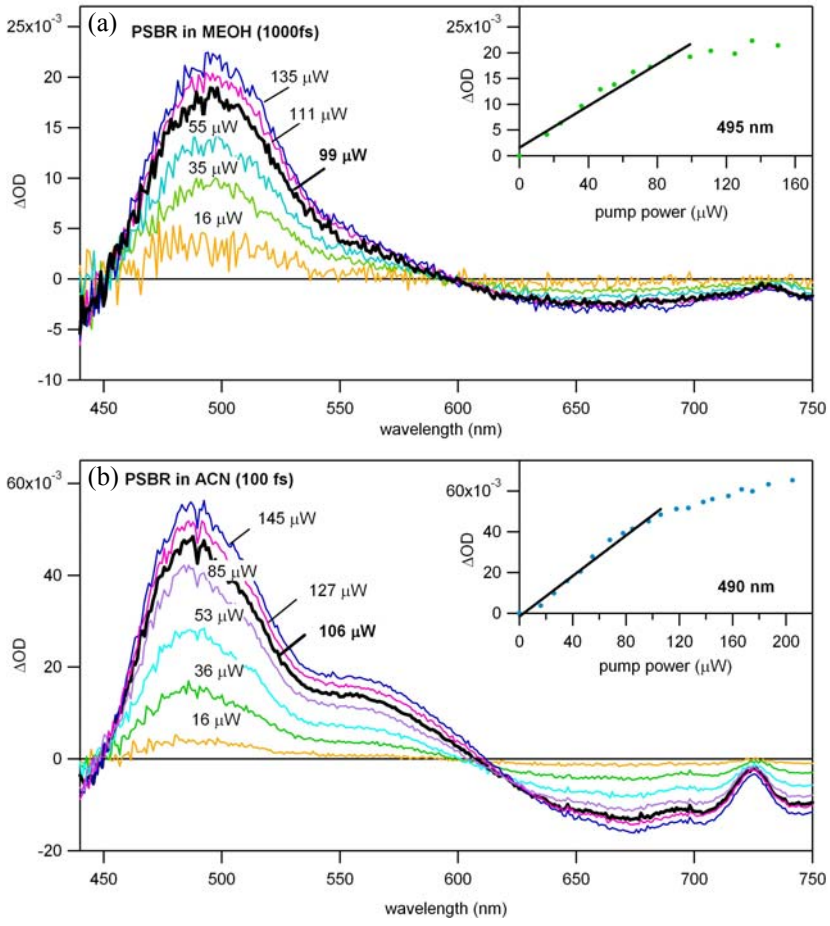


Fig 3.3: Spectra of PSBR in MeOH (a) and ACN (b) taken with different pump power at a time delay of 1000 fs and 100 fs, respectively. Inset: intensity at 495 nm (490 nm) of the peak vs pump power. In both solvents the sample response is linear until pump power of ~100μW.

3.2.1 The data matrices

In Fig. 3.4 the data matrices of PSBR in both solvents are reported.

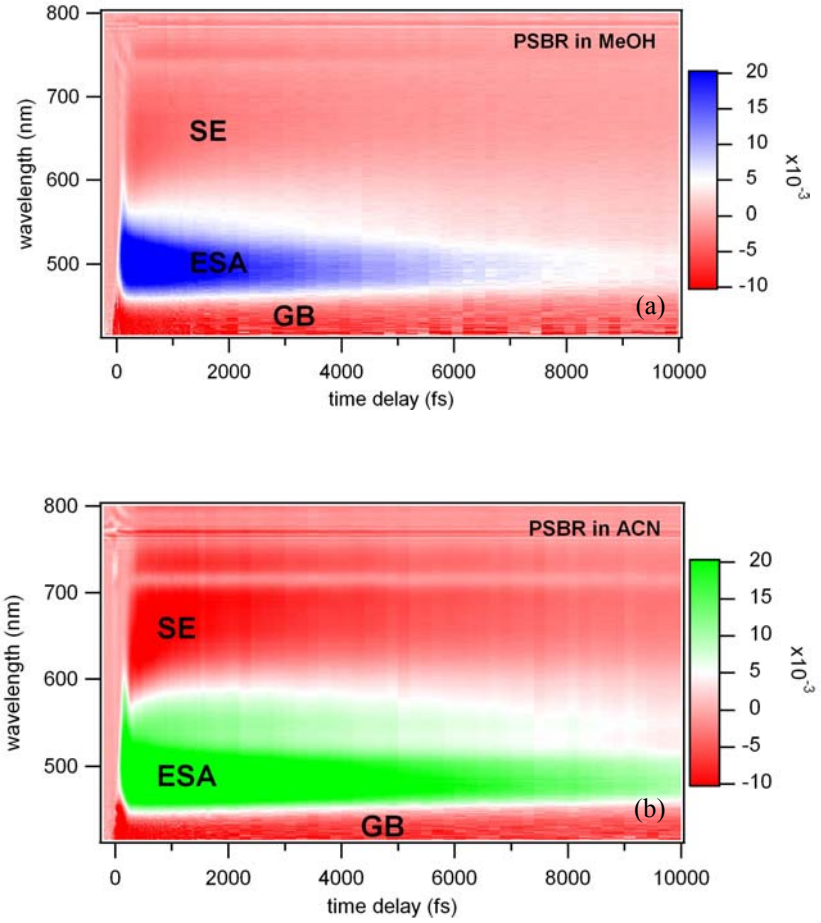


Fig. 3.4: image plot of transient absorption spectra for PSBR in MeOH (a) and in ACN (b). The three spectral components are indicated: ground state bleaching (GB), excited state absorption (ESA) and stimulated emission (SE).

Remembering that a negative signal corresponds to a decrease in absorption, while a positive signal corresponds to an increase, three spectral components can be individuated:

1. $\lambda < 460nm$: a negative spectral component is observed and assigned to the ground state bleaching (GB) since in this region ground state absorption dominates;
2. $460nm < \lambda < 580nm$: a strong positive spectral component is present corresponding to an excited state absorption (ESA);
3. $\lambda > 580nm$: a broad negative spectral component is observed. Since in this region the ground state absorption is negligible, it is supposed that the spectral component can be assigned to stimulated emission (SE) from an electronically excited state S_1 [5]. To verify that it is not a spontaneous emission, we take several spectra of the probe beam (I_p or I_u) at a fixed delay time and pump power, but for different values of the probe power. In Fig. 3.5 the difference between probe intensities when the pump is on or off (I_p - I_u) is reported. As we expect at a wavelength of 700 nm, probe power before the sample and intensity of probe beam after the sample are directly proportional. This confirms that the region corresponds to SE.

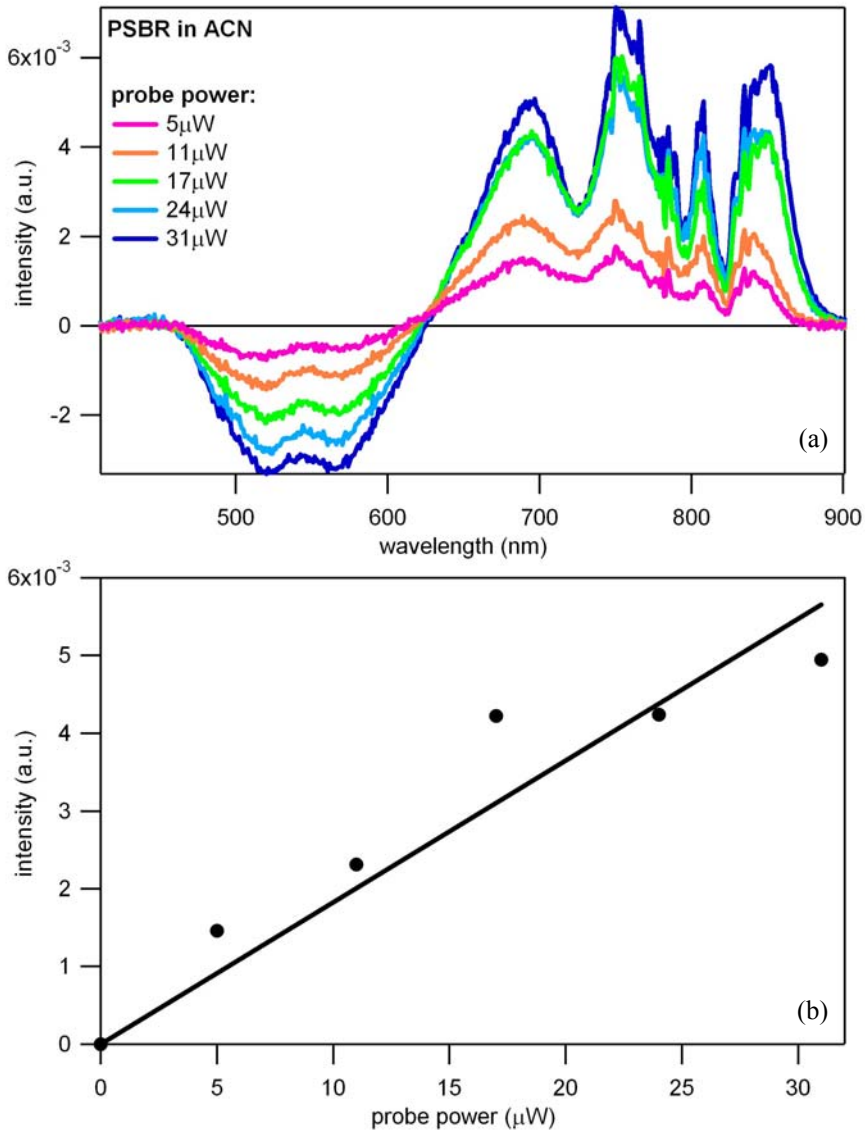


Fig. 3.5: (a) difference between the pump (I_p) and unpumped (I_u) signals at different probe powers; (b) intensity of the I_p-I_u at 700 nm (SE band) vs probe power.

Anyway up to now, we have only located where the GB, ESA and SE spectral components are dominating, but due to overlapping their exact spectral shape is more difficult to extract from the data.

Before entering in detailed analysis some preliminary observations can be drawn from the data matrices. First, the decay of the ESA and SE spectral components results faster in MeOH than in ACN suggesting a different relaxation dynamics. Second, for short time delay (<200 fs) a fast peak is present in both solvents. It is negative in the region between GB and ESA and positive in the region between ESA and SE and the peak is more evident in ACN than in MeOH. A better characterization of these features will be done through the analysis of the spectra and kinetic traces.

3.2.2 Spectra and kinetic traces

In the following analysis only the region between 420 and 800 nm has been considered since elsewhere the signal-to-noise ratio is too low.

The first step in analysis of matrices containing pump-probe data is determination of the time zero and the decay times through a global fitting of a selection of kinetic traces. For the global fitting we select three traces: 520 nm (MeOH) or 490 nm (ACN) that corresponds to ESA, 600 nm that is in an intermediate position between ESA and SE, and 700 nm that corresponds to pure SE. It is observed that the decay at 700 nm corresponds to that of fluorescence at the same wavelength (Fig. 3.6(a) and (b)), demonstrating that in this region there is only the contribution of SE, i.e. of the excited state decay. This observation justifies the use of the decay times found in fluorescence measurements in subsequent fits. We do not consider a trace ~400 nm (GB) since in this region the GVD correction is not determined with high precision due to low XPM signal in solvents (Fig. 2.18). The difference between MeOH and ACN in the choice of the trace around 500 nm is due to a compromise between a region where the GVD is well determined and the appearance of a fast positive peak (Fig.3.6). It is important to underline that we are interested in dynamics larger than 100 fs, in particular in the

decay of the excited state that determines photoreactivities of the PSBR. Moreover, since our time resolution is limited to ~90 fs we restrict our analysis to time constants larger than 100 fs.

The following fitting procedure has been employed:

1. the single traces are fitted using fluorescence decays time(900 fs,4000 fs,13000 fs for MeOH and 4000 fs,8400 fs for ACN), a variable fast decay time ~100 fs, and a fixed decay constant of 1 ns that represents quasi constant residual features;
2. the coefficients found in the previous step are used to do a first global fit of the three traces with all the times fixed except the fastest one to obtain an estimation of the delay time;
3. the delay time is fixed, and the time delays are let to vary one by one until an equilibrium is reached.

In this way time constants of 600 fs, 3000 fs, 12000 fs in MeOH and of 3000 fs and 8200 fs in ACN have been found. In the latter case an additional time of ~390 fs was found for the kinetic traces between 490 nm and 640 nm where it is also observed the fastest dynamic.

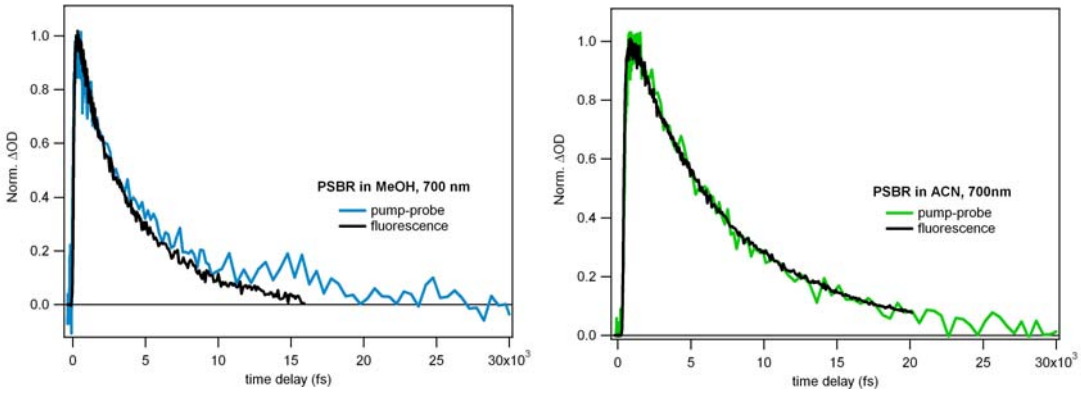


Fig. 3.6: Comparison between kinetic traces at 700 nm in MeOH (left) and in ACN (right) obtained with pump-probe and time-resolved fluorescence set-up. All traces are normalised.

A look at the time resolved spectra (Fig.3.7 and 3.8) reveals that they differ for PSBR in MeOH and in ACN.

In MeOH the ESA reaches the maximum value at 150 fs, while in ACN at 300 fs. Also the rise of the SE is different in two solvents, where in ACN both SE and ESA reach its maximum at the same moment (300 fs), while in MeOH the SE maximum arrives 150 fs after the ESA maximum (300 fs).

For long time delays (t>300 fs) the signals decay functions shows several decay times originating from the electronic relaxation from S_1 to S_0. Moreover, it can be observed that the SE spectral component is continuously redshifting, while simultaneously the ESA spectral component is blueshifting in both solvents, but while in MeOH this shift goes on until 5 ps, in ACN it ceases at 1.5 ps. In both solvents, the end of shifting goes with the appearance of a shoulder in the red part of ESA spectral component, a feature that is more evident in ACN. As it well be seen in discussion, the spectra for t>2 (ACN) and t>5 ps (MeOH) can be considered as vibrationally equilibrated spectrum. Appearance of an isosbestic point at 620 nm for t > 1 ps in MeOH (Fig. 3.7(b)) and at 610 nm for t>3 ps in ACN (Fig. 3.8(b)) tells us that the ESA and SE spectral components have the same relaxation dynamics.

The spectra for t>50 ps has a small negative signal in the blue part followed by a positive signal after 540 nm. The spectral component shape is completely different with respect to the shape observed for early time delays thus we can consider that at this delay a complete decay of the electronic state is reached. Negative signal around the position of the ground state absorption is attributed to those molecule which have isomerized since the 11-cis isomer has approximately 50% smaller extinction coefficient [3, 5, 7]. We cannot distinguish the *all-trans* and 11-cis GB spectral components since their maximum shift is only 2 nm [5]. The residual positive signal is assigned to undefined metastable product [7].

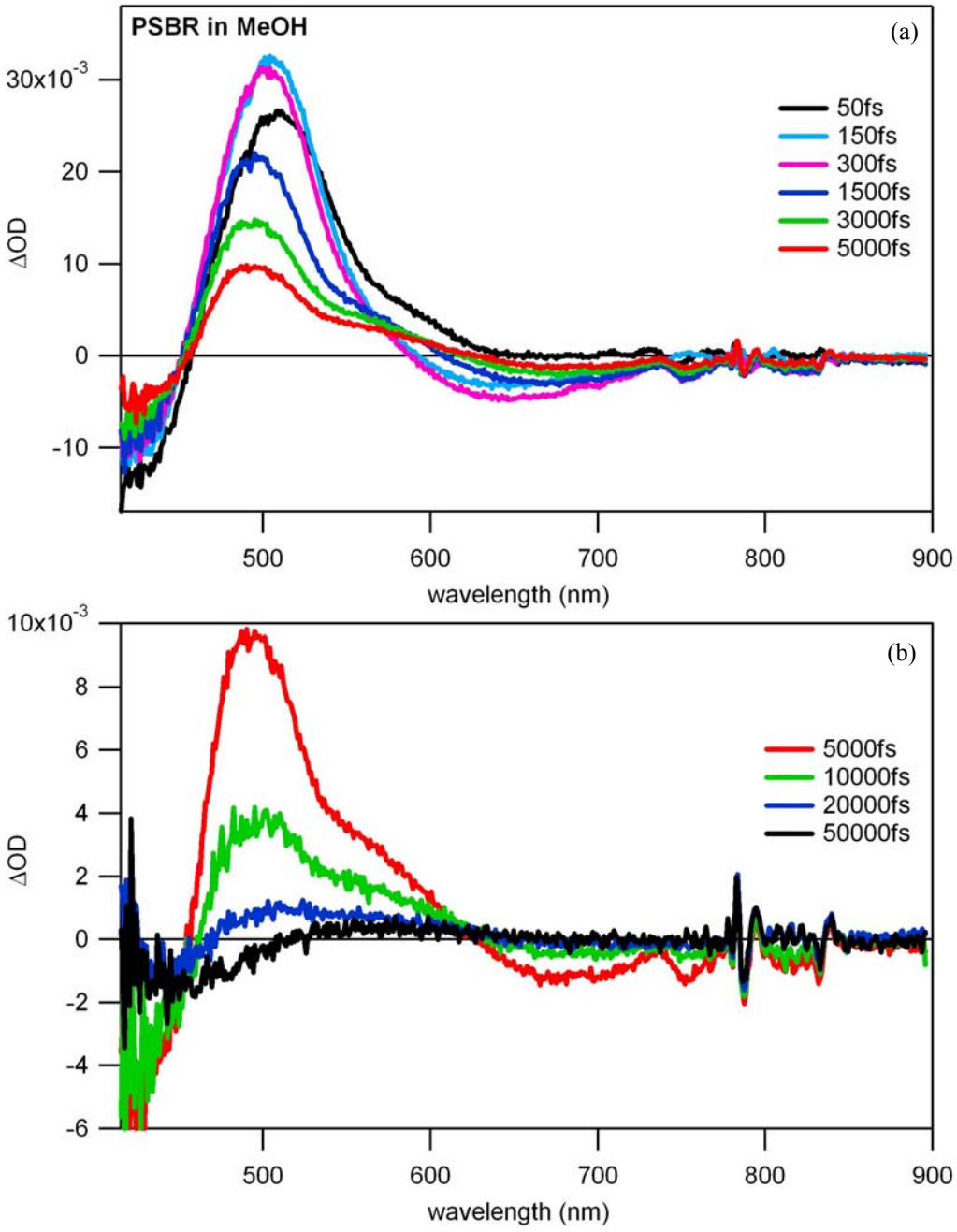


Fig. 3.7: Transient absorption spectra for PSBR in MeOH in the range (a) 5-50 ps and (b) 5000-50000 fs.

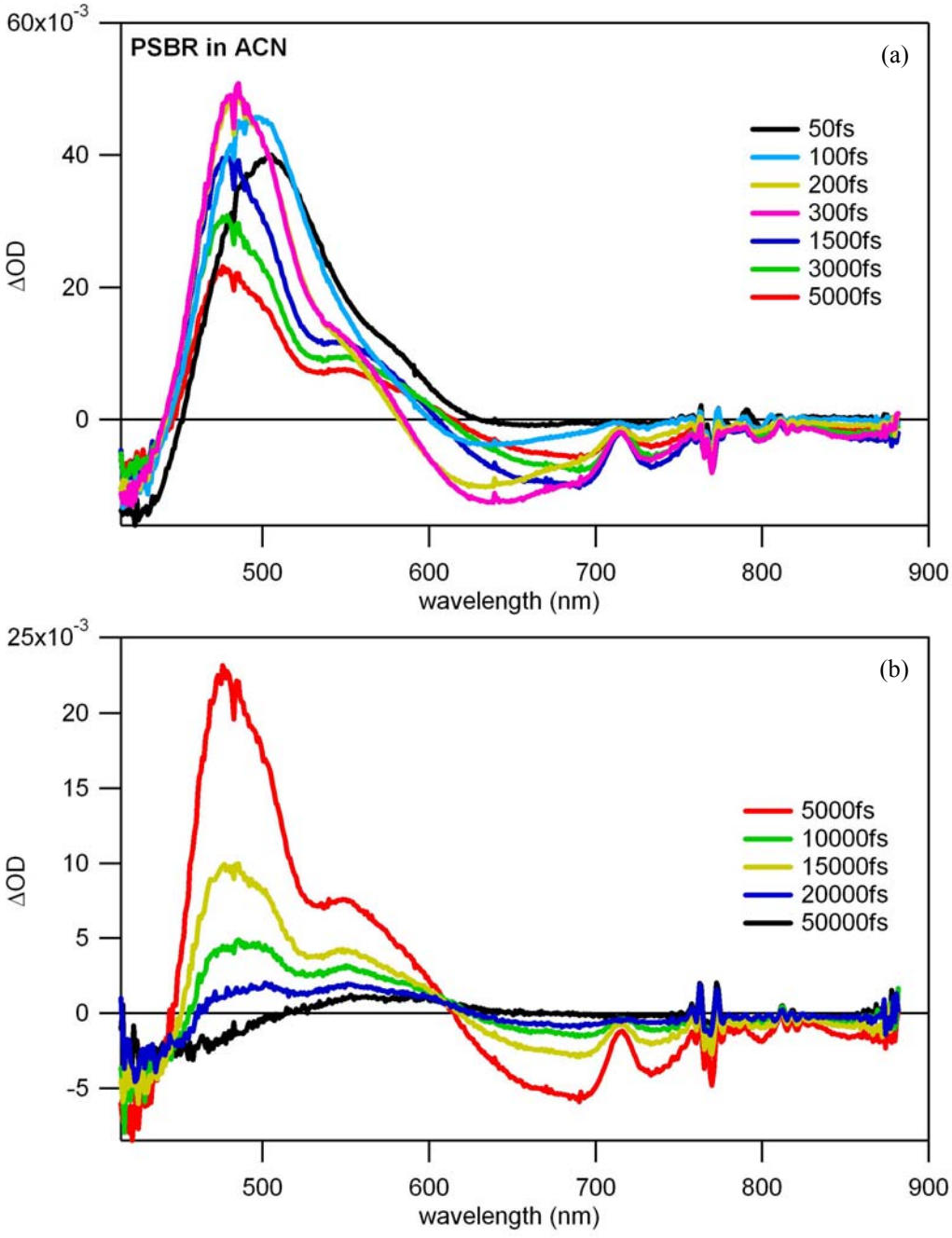


Fig. 3.8: Transient absorption spectra for PSBR in ACN in the range (a) 50-5000 fs and (b) 5-50 ps.

The presence of a residual signal is more evident if we consider kinetic traces. In Fig. 3.9(a)-(b) a trace in the GB region (440, 450 nm) is reported. A fast negative peak, present also at other wavelengths, and a remaining negative signal for long time delays (t>20 ps) are present. In Fig. 3.9(c)-(d) another trace is reported but this time it belongs to the red part of the ESA spectral component at 560 nm. Also in this trace a fast peak and a residual for long time delays are observed, but this time they are positive. As discussed in ref [4, 5] the fast peak is probably due to the contribution of the S_2 excited state.

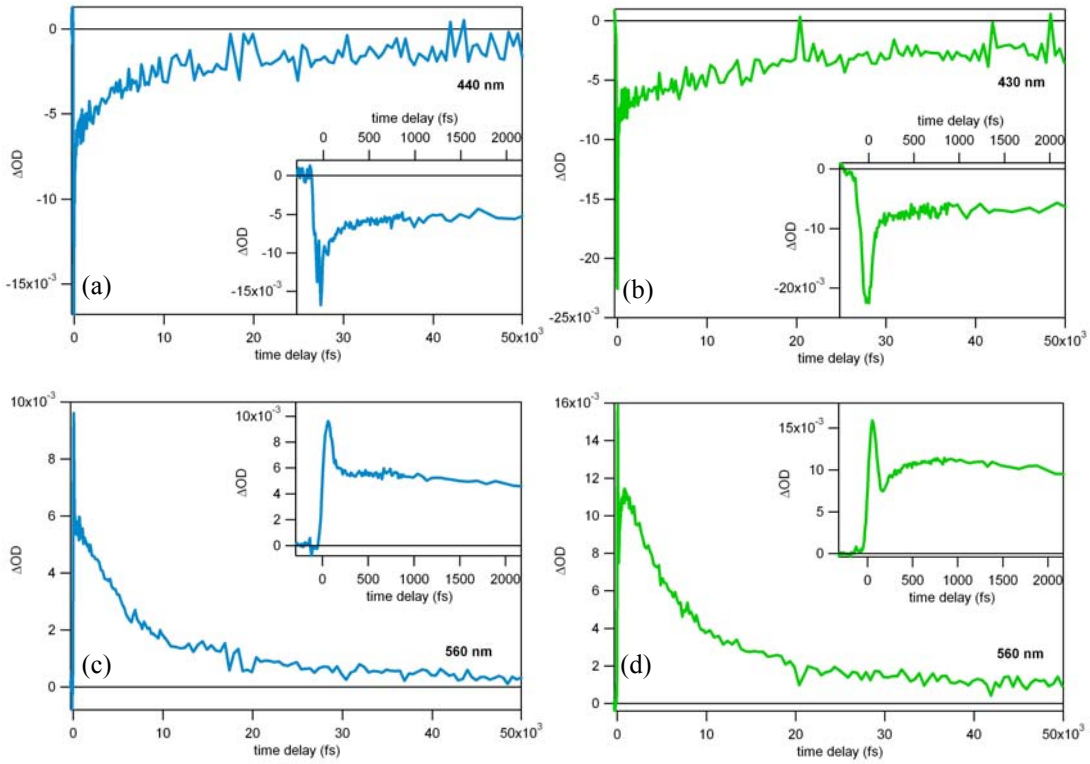


Fig. 3.9(a)-(b): kinetic traces at 440 nm for PSBR in MeOH (a) and at 430 nm for PSBR in ACN (b) corresponding to the GB band. A fast negative peak (inset) and a remaining negative signal for long time delays (t>20 ps) are observed. (c)-(d): kinetic traces at 560 nm for PSBR in MeOH (c) and in ACN (d) corresponding to the red part of the ESA band. A fast positive peak (inset) and a remaining positive signal for long time delays (t>30 ps) are observed.

Similar relaxation dynamics of the ESA and SE absorption spectral components is evident if we directly compare a trace at 490 nm for MeOH and at 470 nm for ACN with the trace at 700 nm that we know, from the comparison with fluorescence, to be related only to relaxation of the excited state (Fig.3.10(a)-(b)). The only difference between the two traces is found for long time delays (t>10 ps) where the residual negative signal is observed in the ESA traces. The relative amplitude of different time decays are reported in table 3.2 and it can be seen that both ESA and SE traces have very similar decay parameters except for the presence of the long time decay. Also the rise of the two traces is comparable and is ~140 fs in MeOH and ~240 fs in ACN.

In Fig. 3.10(c)-(d) a kinetic trace at 600 nm is reported, a wavelength corresponding to an intermediate region between ESA and SE spectral components. Here a fast positive peak is followed by a negative signal, that further rises with 600 fs (MeOH) and 390 (ACN) to a positive signal. Finally absorption decreases biexponentially with 3 ps and 12 ps decay constants in MeOH and 3 ps and 8.2 ps in ACN.

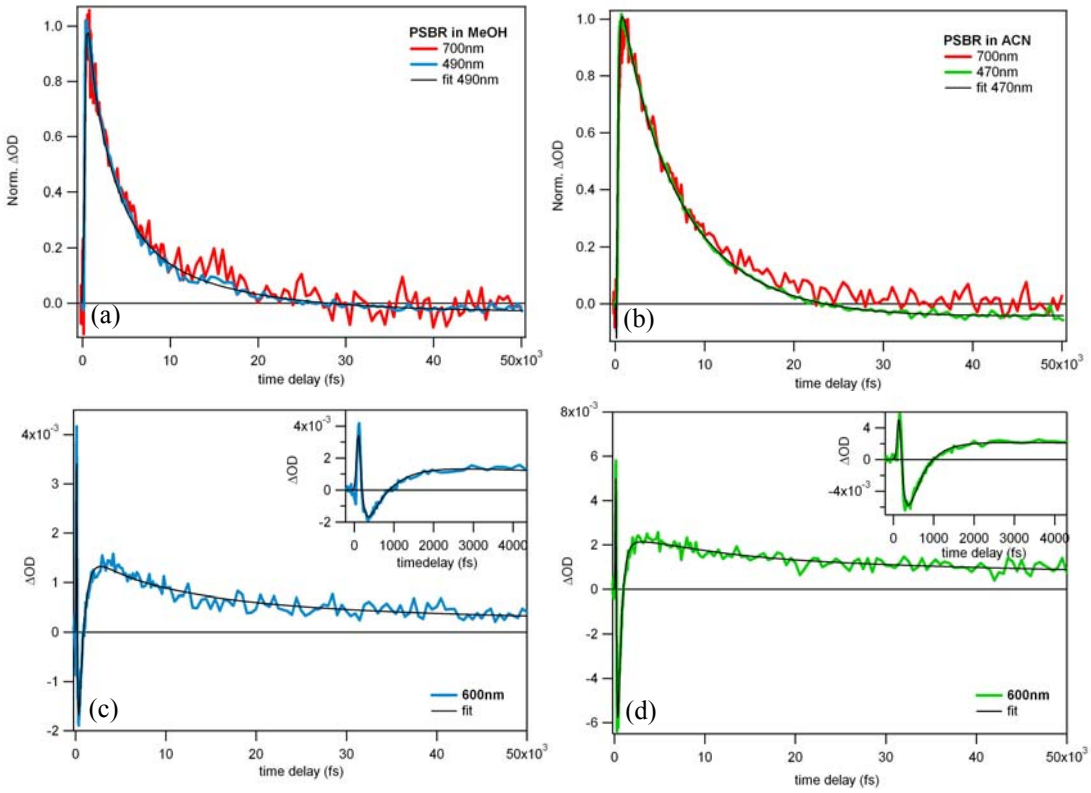


Fig. 3.10(a)-(b): Comparison between a kinetic trace of the ESA band (490 nm in MeOH and 470 nm in ACN) and a kinetic trace of the SE band (700 nm) for PSBR in MeOH (a) and ACN (b). The fit of the ESA trace is also reported. All the traces are normalized. (c)-(d): Kinetic trace at 600 nm in the region between ESA and SE bands for PSBR in MeOH (c) and in ACN (d). The fit of the data is also reported. Inset: the first part of the trace for t < 4 ps, where both the fast positive peak and the negative part can be observed, is enlarged.

Direct comparison of the kinetic traces at 700 nm (Fig. 3.11) obtained in MeOH and in ACN reveals their different decay. While in MeOH three decay times are necessary to fit the trace, only two times are sufficient in ACN. In Table 3.2 the relative amplitudes associated to different time decays are reported. It can be noted that while in MeOH the dominant time decay is the shorter one (3 ps), in ACN it is the longest (8.2 ps).

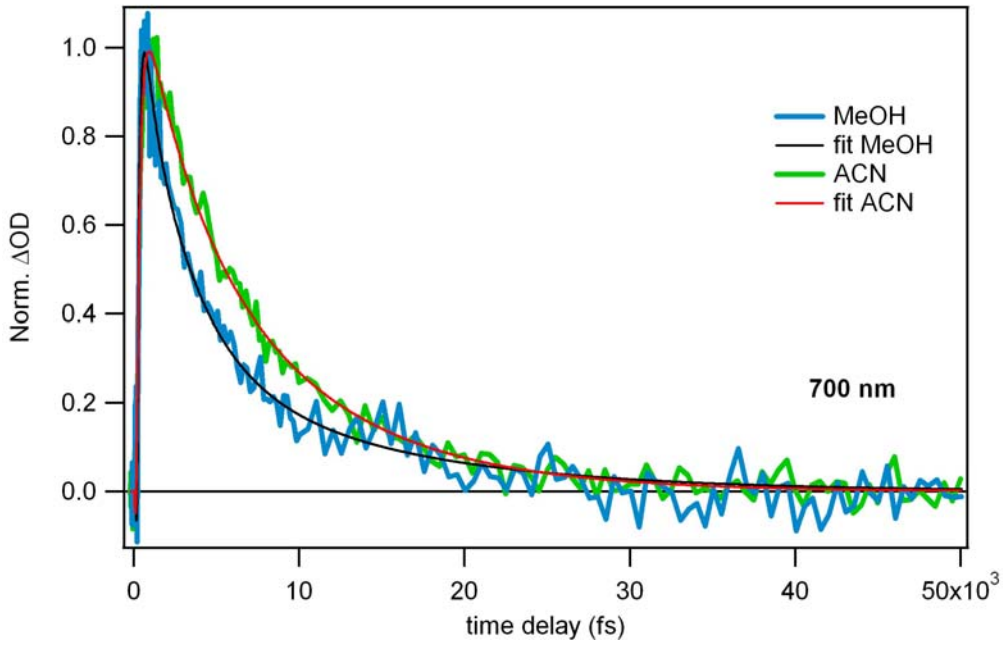


Fig. 3.11: Transient absorption kinetic trace at 700 nm (SE spectral component) for PSBR in MeOH (blue) and in ACN (green).

MeOH	τ_1 = 600 fs	τ_2 = 3 ps	τ_3 = 12 ps	τ_4 =100 ps
490 nm	0.20	0.54	0.24	0.02
700 nm	0.19	0.56	0.25	-
ACN	-	τ_2 = 3 ps	τ_3 = 8.2 ps	τ_4 =100 ps
470 nm	-	0.22	0.73	0.05
700 nm	-	0.29	0.71	-

Table 3.2: Decay times τ_i and their relative amplitudes for the kinetic traces related to ESA (490 nm for MeOH and 470 nm for ACN) and to SE (700 nm) spectral components.

Finally, an interesting feature can be observed at 440 nm in ACN and at 450 nm in MeOH where GB and ESA compensate one another (Fig. 3.12). A sort of plateau is observed for t< 1 ps followed by a rise of the residual negative signal. This rise can be attributed to the appearance of the 11-cis isomer and since the same time constant should be observed also in the decay of the excited state, a global fit of 440 nm and 450 nm traces with that at 700 nm for the relative solvent is done. A rise of ~3 ps is found in both solvents, so we can conclude that the isomerization time is shorter than this value.

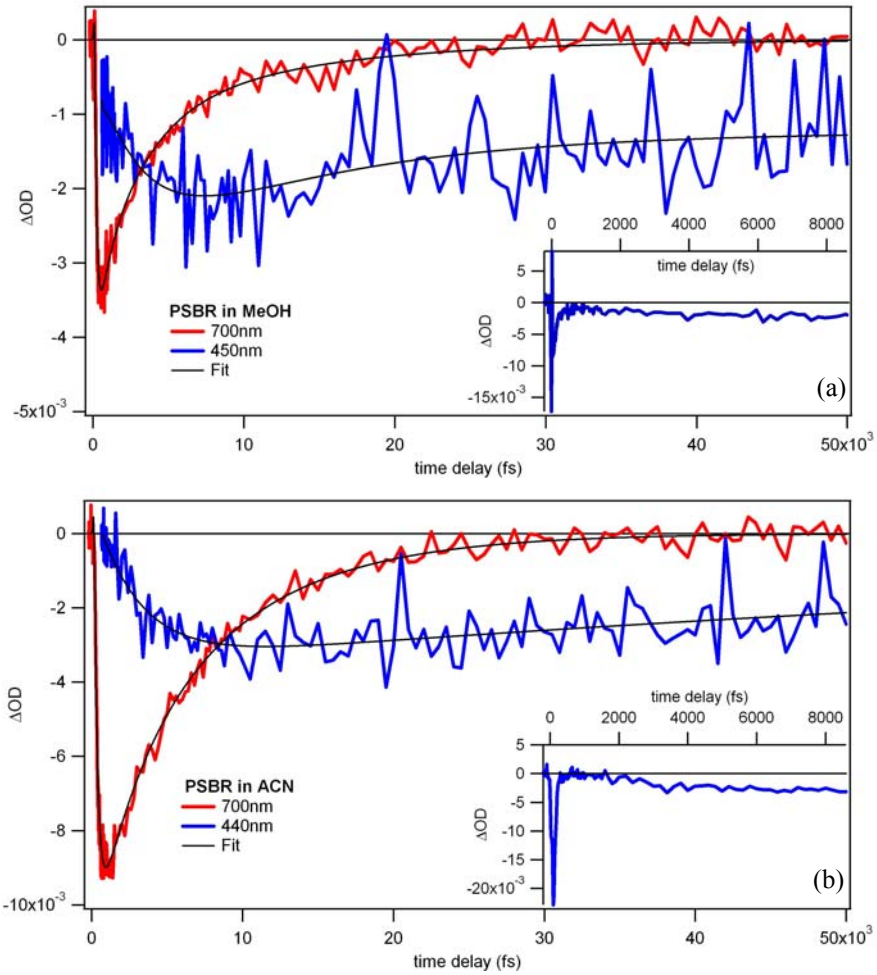


Fig. 3.12: Comparison between the decay of the excited state (SE band) and the rise of the CIS band at 450 nm for PSBR in MeOH (a) and at 440 nm in ACN (b). Inset: the first part of the trace corresponding to t < 8 ps is enlarged. The fast initial dynamic followed by a plateau and a subsequent rise can be observed.

3.2.3 SVD Analysis

A global fit of the eigen-traces is done using time zero and decay constants deduced from the fitting of the kinetic traces as explained in the previous section. The coefficients obtained from the fit are used to construct the Decay Associated Spectra (DAS) as explained in paragraph 2.13. In Fig. 3.14 the SVD eigen-traces with their fits are reported, while the corresponding DAS are shown in Fig. 3.14 for both solvents. In Fig. 3.14(b) the DAS associated to the shortest time, used to fit the kinetic traces in the intermediate part between ESA and GB, is reported as a dotted line since it is not used for the fit of all the kinetic traces. The similarities between the first three traces in MeOH and the two in ACN suggest that the choice to use three and two time constants, respectively, is correct. Moreover, it can be observed that the DAS associated to ACN have a more detailed shape, with a well defined shoulder in the red part of the increase in ESA spectral component, probably caused by more efficient vibrational relaxation in this solvent.

In Fig. 3.15 the DAS associated to an infinite time delay is reported for both solvents. A positive residual signal is observed and attributed to the presence of undetermined remaining species.

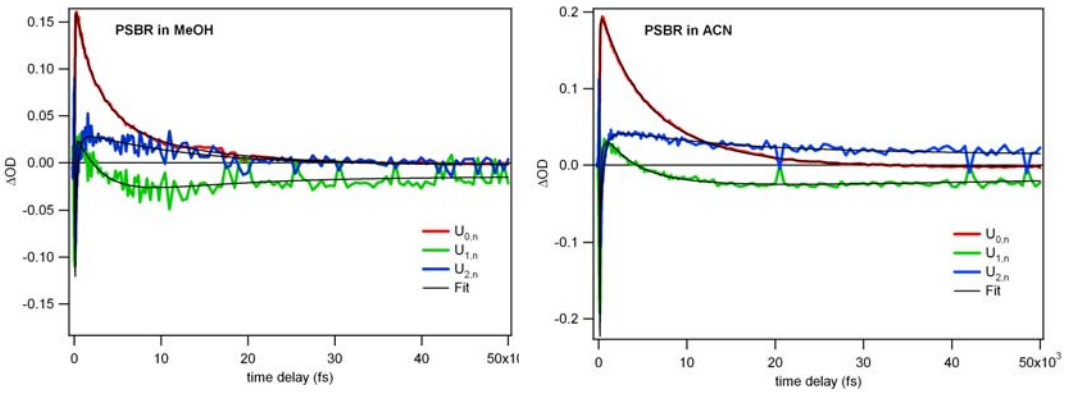


Fig. 3.13: SVD eigen-traces for PSBR in MeOH (left) and in ACN (right).

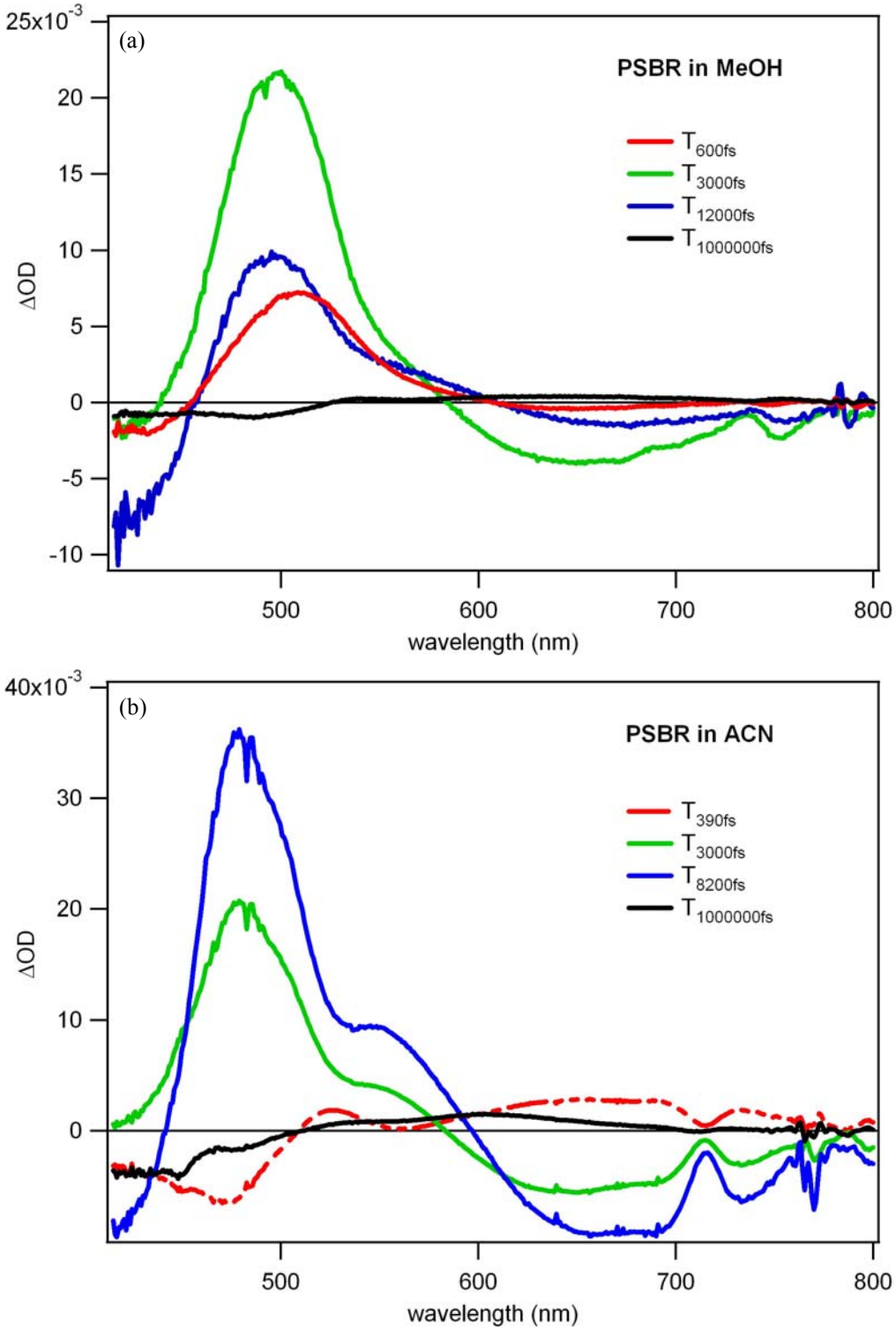


Fig. 3.14: Decay Associated Spectra (DAS) of PSBR in MeOH (a) and in ACN (b). In (b) the DAS associated to the shortest time (390 fs) is reported as a dotted line since it is not used for the fit of all-the kinetic traces.

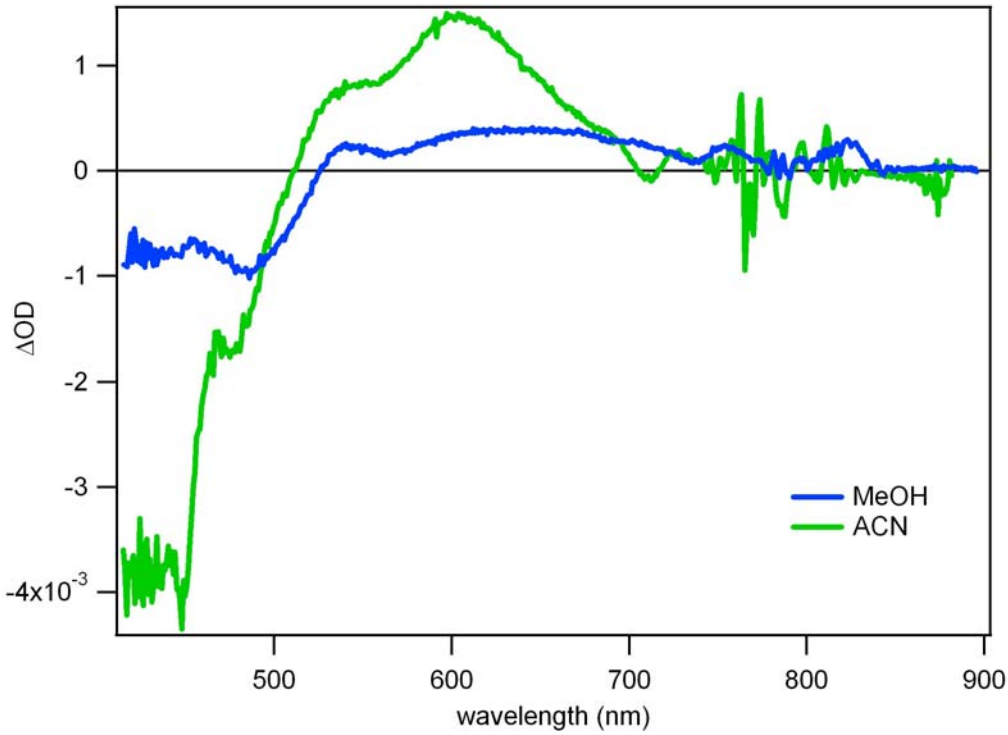


Fig. 3.15: Comparison between the DAS associated to the 1 ns time decay (CIS spectral component) for PSBR in MeOH (blue) and ACN (green).

4. Discussion

In this section a detailed discussion and interpretation of the experimental results is given. In the first part we give an overall interpretation of the isomerization process on the basis of pump-probe and steady-state results. In the second part a comparison between our results in solution and results from literature in protein environment is given.

4.1 Spectral structure assignments

In Fig. 4.1 a kinetic trace at 5 ps is shown and the three principle spectral components individuated in pump-probe measurements are indicated. As reported in previous chapter, remembering that a negative signal corresponds to a decrease in absorption while a positive one corresponds to an increase, four spectral components can be identified: ground state bleaching (GB) with maximum (λ_{max}) at 445 nm, excited state absorption (ESA) with λ_{max}= 580 nm, stimulated emission (SE) with λ_{max} = 700 nm and *cis* spectral component (CIS) that corresponds to spectrum taken at 50 ps (Fig. 4.1). Around the maxima there are regions in which a spectral component is dominating, although they have a more complicated

spectral shape and in some region they overlap. In Fig. 4.1 their possible spectral extention is reported.

In SVD analysis the CIS spectral component is represented by the DAS associated to the longer time delay (1 ns) and a negative spectral component under ~500 nm followed by a positive spectral component are observed in both solvents (Fig. 3.15). They correspond to the residual spectrum observed for long time delays (>20 ps) in the range 400-650 nm (Fig.3.9).

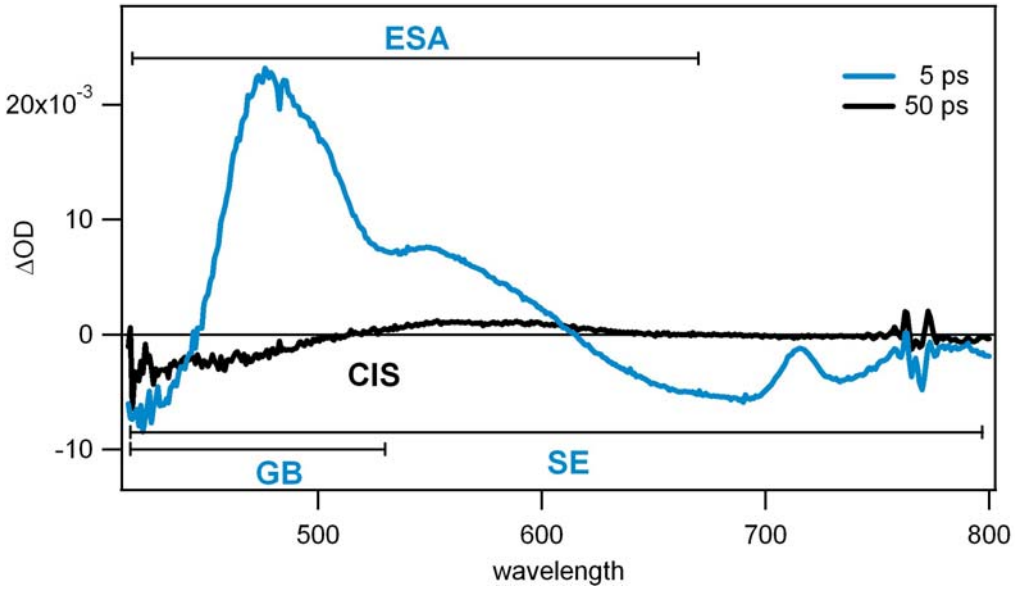


Fig. 4.1: Spectra at 5 ps (blue) and at 50 ps (black) of PSBR in ACN where the different spectral components are indicated.

The negative remaining signal observed in the traces at shortest wavelengths (< 500 nm) is attributed to concentration increase of *cis*-isomer in solution. Since the latter has 50% smaller extinction coefficient with respect to all-trans, a decrease in absorption is measured. Moreover, a positive signal is observed for higher wavelengths (500-650nm). It was observed for the first time by Bismuth et al. [7] who did pump-probe measurements of PSBR in ethanol. Assignment to the *cis*-isomer is excluded because, as we have seen, it produces a negative signal, limited

for $\lambda < 530$ nm. Possibly, it could appear due to the presence of hot molecules before a full thermalization or to undefined metastable photoproducts. The first possibility is excluded since no continuous evolution which would accompany cooling of the chromophore is observed, thus the second possibility remains as the most plausible. To identify the structure of this photoproduct, further investigations are necessary.

4.2 Dynamics of the system

As already discussed in the introduction, the photoisomerization process of PSBR can be rationalized by the 2-state model where, after the population of the Franck Condon (FC) point, the system relaxes along C=C double bond stretch coordinate to a stationary point (SP), from where the molecule continuous relaxation along torsional coordinate toward the conical intersection (CI) between the potential surfaces of the excited (S_1) and the ground state (S_0).

The first part of the relaxation process is happening very fast, in < 100 fs according to Olivucci et al [26, 66], ultimately causing excitation of many vibrational modes [66]. Time resolved fluorescence measurements [4] have shown that the S_1 state vibrationally relaxes with time constant of τ_b=2 ps in MeOH and τ_b=0.48 ps in ACN. Parallely, since the S_2 state is also accessed with 400 nm excitation [67] it undergoes internal conversion with τ_c=0.44 ps in MeOH and τ_c=0.35 in ACN (Fig. 4.2).

In the second part of the relaxation, the molecule arrives at SP, where it is completely vibrationally relaxed and the isomerization process can start. In fluorescence and pump-probe measurements different decay channels (with decay constants τ_1, τ_2, τ_3) are individuated for the S_1 internal conversion, corresponding to the decay of the ESA and SE spectral components. They are assigned either to non-reactive (τ_1) or reactive (τ_2,τ_3) paths on the PES. These constants are different in two solvents used here, and in particular τ_1 constant is present only in MeOH. The molecule follows one of these paths on the PES, finally reaching a CI where another branching happens. Here, the molecule can reach an equilibrium

point on the ground state PES corresponding either to *all-trans* or *cis* configuration.

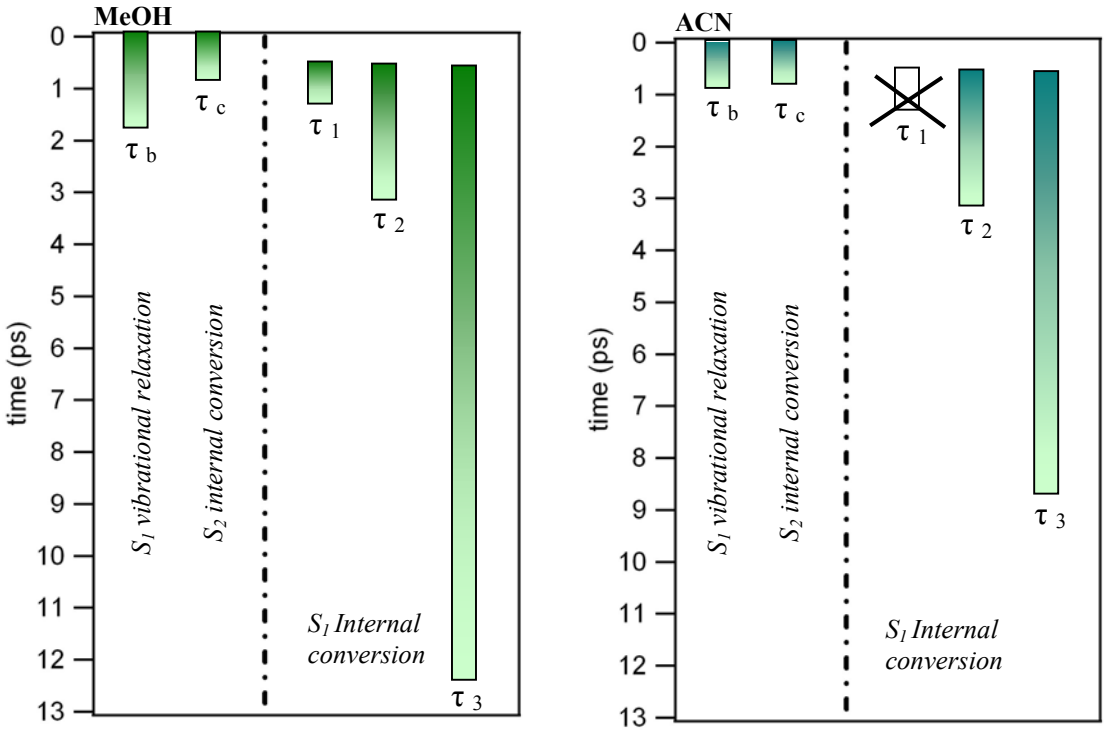


Fig. 4.2: Schematic representation of the dynamics of the system in both solvents. Early events correspond to S_1 vibrational relaxation (τ_b = 2 ps in MeOH and 0.48 ps in ACN) and S_2 internal conversion (τ_c = 0.44 ps in MeOH and 0.35 ps in ACN), while later on the S_1 internal conversion takes place and corresponds to the decay of the ESA and SE spectral components where three different decay constants are individuated (τ_1 = 0.6 only in MeOH, τ_2 = 3 ps in both solvents, τ_3 = 12 ps in MeOH and 8.2 ps in ACN).

4.3 Early events: vibrational relaxation and S_2 internal conversion

From the pump-probe spectra for t < 5 ps (Fig.3.7(a)-3.8(b)), two main features are observed in both solvents:

1. the blueshift of the ESA spectral component and the redshift of the SE spectral component;
2. ESA spectral component narrows and a shoulder appears in the red part of the ESA spectral component.

This behaviour, already observed in previous pump-probe measurements [5, 6, 7], can be explained if we consider the results of fluorescence measurements where, apart from vibrationally relaxed fluorescence, two different spectral components are individuated and related to the relaxation of S_1 (b-spectral component) and to S_2 (c-spectral component). As it can be observed in Fig. 1.7 the b-spectral component goes from ~550 nm to ~900 nm and has a slower decay (τ_b) in MeOH than in ACN (2 ps versus 480 fs), while the c-spectral component (τ_c) covers a range from ~400 to ~700 nm and has a similar decay in both solvents (~400 fs). It was observed that as the b-spectral component and the c-spectral component loose their intensity, the fluorescence narrows by more than 2000 cm^{-1} [4]. These S_1 and S_2 relaxation processes are also responsible for the features 1) and 2). The latter can be rationalized in a more phenomenological way by looking at Fig. 4.3, schematically showing energy levels of S_1, S_2 and higher electronic states (S_n). When the system relaxes and goes from the FC point to the SP, less energy is necessary to go from S_1 to the ground state (redshift of the SE spectral component) while more energy is needed for the absorption process $S_1 \rightarrow S_n$ and $S_2 \rightarrow S_n$ (blueshift of the ESA spectral component).

The relaxation process can explain also the different shape of the spectra observed in MeOH where the vibrationally relaxed spectrum is reached later than in ACN, since the decay of the b-spectral component is slower. The S_2 contribution is

significant, especially in the early time of the process. On the contrary in ACN the b- and c- spectral components have almost the same much shorter decay, and, therefore, the shoulder starts to be visible earlier at ~1.5 ps when the shift of the peaks is over. The fact that in MeOH the maximum of the ESA peak is reached before that of the SE

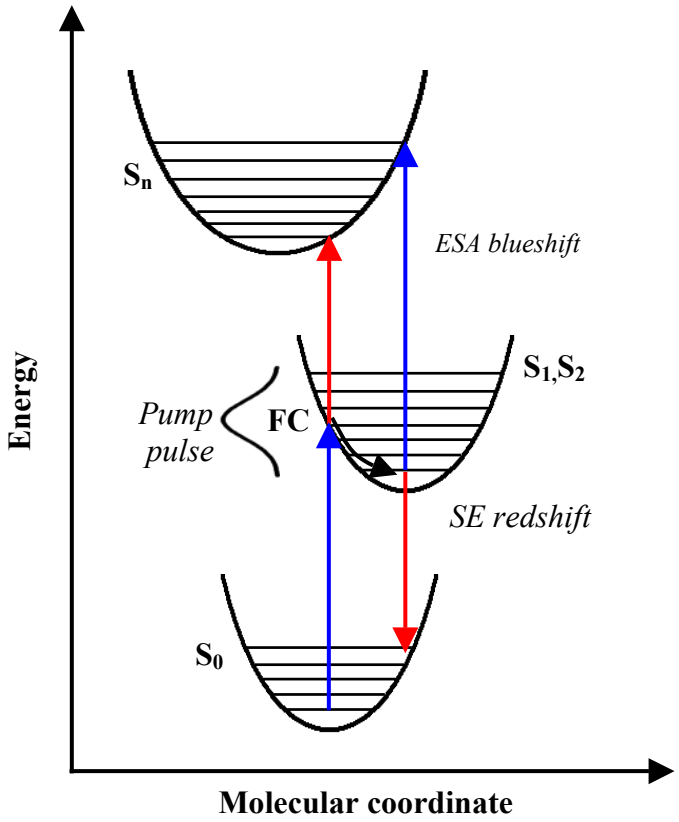


Fig. 4.3: shift of the ESA and SE spectral components. When the molecule is excited, it reaches the FC point and then relaxes. When it reaches the point of minimum energy, more energy is necessary to reach the excited state S_n (ESA blueshift) while less energy is necessary to reach the ground state S_0 (SE redshift).

peak (not observed in ACN) can also be related to a different weight of the S_2 internal conversion and the S_1 vibrational relaxation, since the spectral components associated to these two processes are overlapping and the former (c-spectral component) in MeOH has also a larger intensity in ACN.

These two contributions can also explained the fast decaying peak (τ < 100 fs) observed in all kinetic traces from ~400 to ~650 nm in both solvents (Fig.3.9, 3.10(c)). This peak was already observed in previous pump-probe measurements [5, 6, 7] and attributed to the depopulation of the FC point and to the propagation

of the wavepacket towards the bottom of the S_1 potential surface. In our case this hypothesis can be confirmed by the presence of a fast negative peak around 430 nm that can be related to stimulated emission from the FC point that was not observe before. On the basis of fluorescence measurements and on the fact that S_1 and S_2 are almost degenerate near the FC point [66], we think that same contribution to this peak comes also from S_2, that is, from the stimulated emission $S_2 \rightarrow S_0$ (negative fast peak at short wavelength) and from the absorption process $S_2 \rightarrow S_n$ (positive fast peak in the region 460-650 nm).

We are unable to say more about this fast dynamic since our time resolution is too low. Future measurements with a resolution of < 10 fs are needed to clarify the early time dynamics of the PSBR photoreaction.

4.4 Internal conversion process of the S_1 state

The decay of the SE and ESA spectral components reflects the S_1 internal conversion process and results multiexponential in both solvents but with different time constants. That these two spectral components follow the same dynamics is seen not only by the appearance of an isosbestic point in spectra for long time delays (t>3 ps in ACN and t>5ps in MeOH, Figs. 3.7, 3.8) but also in the good superposition of normalized kinetic traces of the ESA and SE spectral components (Fig.3.10(a)).

As reported in previous section, in MeOH these spectral components show triexponential decay while in ACN a biexponential decay is sufficient to fit the data.

Four observations can be made about these decay channels:

a. a fast decay channel is observed only in MeOH (channel I, τ_1=0.6 ps);
b. in both solvents a channel with lifetime of 3 ps (channel II, τ_2=3 ps) is observed;

c. the slower channel becomes even slower in going from ACN (τ_3 =8.2 ps) to MeOH (τ_3=12 ps) (channel III).
d. in MeOH relative amplitude (a_2) of channel II is larger than the one of the channel III (a_3) while in ACN we have the inverse situation ($a_2 < a_3$).

All these features have been also observed in previous fluorescence measurements [4]. This shows that the S_1 SE and ESA stems from a surface with probably three minima, each corresponding to a radiative decay channel. SVD analysis is showing that DAS of all these decay channels (I-III) are very similar telling us that minima are not having very different potential energies. Therefore, surface must be shallow in the region where the chromophore is vibrationally relaxed.

Our hypothesis is that different decay channels, non-reactive and reactive, are present on S_1 and that solvent modifies the PES and consequently changes the photoisomerization quantum yield, Φ.

Since previous HPLC measurements [3, 31, 32] and our steady-state measurements, have found an increase of Φ in passing from MeOH to ACN, and since in the latter solvent only channel II and III are presented, it is plausible to associate channel I to the non-reactive channel. Why channel I is not present in ACN has not been clarified yet.

A first hypothesis is that solvent changes the S_1 topology in such a way that the local minimum associated to this non-reactive channel does not exist. Theoretical calculation of the S_1 topology for PSBR in ACN are needed to support this idea.

Our steady-state measurements have found wavelength dependence of Φ for MeOH, more precisely, slight increase of Φ when the chromophore is excited with no excess energy (540 nm). In ACN no variation is observed. An activation barrier could be present on the non-reactive path so that a minimum excess energy in S_1 is necessary to access to it. In MeOH there is a good agreement between our values and the literature [3], while in ACN we found a smaller value (0.22 instead of 0.27 [3]). Nevertheless, the Φ enhancement in passing from MeOH to ACN is observed also in our case. The fact that in ACN Φ does not depend on the

excitation wavelength can be due to solvent behaviour of vibrationally relax the system. In an efficient and fast way, so that the molecule is unable to overtake the potential barrier. This hypothesis is supported by a theoretical work of Burghardt and Hynes [68] that found that a solvent is able to induce new intramolecular vibrational couplings and to cancel the intrinsic one in the chromophore, therefore influencing the pathway from the FC zone to the CI.
Anyway, even upon 540 nm excitation when channel I is not populated [4] the Φ in MeOH is 15% smaller (35% according to Koyama et al. [3]) than in ACN suggesting that the behaviour in the latter solvent cannot be rationalized by only the absence of the non-reactive decay channel. In fact, as showed by Nakamura and coworkers [69], the solvent can affect not only topology of the hypersurface near the FC point, thus changing the branching between non-reactive and reactive channels, but also can change the topology of the CI. The latter plays a big role in determing the branching ratio at the CI between formation of *cis* isomer and return to the *all-trans* ground state. The existence of branching at the CI is corroborated by the fact the amplitudes of channel II and III (Table 3.x) related to the percentage of molecules that follows reactive paths would give $a_2+a_3=\Phi=0.8$, a value 4 times exceeding the one determined by HPLC analysis [4].

The fact that channel II is present in both solvents (and probably also in other solvents as suggested by fluorescence measurements [4]) indicates its relation to isomerization. This is confirmed by the fact that the same time constant is found also in the rise of the CIS spectral component (Fig. 3.12) whose intensity is proportional to concentration of *cis*-isomer in solution. On the basis of this consideration channel II may be related to the formation of 11-cis isomer since it is formed with highest efficiency. On the other hand, channel III may represent other isomerization path, 9-cis and 13-cis isomers (table 1.2), since we know that in solvents the isomerization is not completely selective [3].

Anyway, on the basis of observation d), which noted that amplitude of channel III (a_3) changes in two solvents, other assignments of this channel can be proposed. In fact a similar behaviour has been already observed in fluorescence measurements in DCM where $a_2 < a_3$ under 570 nm excitation and $a_2 > a_3$ under 400 nm excitation [4]. Even if the relative amplitudes cannot be directly related to the photoisomerization efficiency since the branching ratio at the CI is very important, the fact that, as for a_3, we observe enhancement of Φ may suggest that channel III is also related to 11-cis isomerization. If both channel II and III are related to 11-cis isomerization, we can suppose either there are two CI with a different branching ratio or there is only one CI that can be reached through two different paths each having different branching ratio.

It remains to answer which channel is more favorable to 11-cis formation.

If it is channel II, the only possible explanation to rationalize larger Φ in ACN where $a_2 < a_3$, is that ACN modifies the CI in such a way that the branching ratio is so favorable to 11-cis formation, that it compensates the fact that at the FC point the branching ratio is less favorable for channel II. But this cannot justify the behaviour observed in DCM because in this case the different branching observed at the FC point is due to different excitation wavelength, and this cannot influence the CI.

This leaves us with channel III as the most efficient in 11-cis formation. On the other hand, time constant τ_3 related to channel III is smaller in ACN than in MeOH or DCM. This could suggest that the solvent modifies the path followed by the molecule on the PES in such a way that in ACN the branching ratio at the CI is more favorable to 11-cis isomerization so that Φ is enhanced respect to the other solvents. In the case in which two CI are present on the PES, we can also suppose that ACN is able to modify the CI associated to this channel so that Φ is increased.

Finally, even if with our measurements we cannot isolate a spectral feature whose dynamics is generated exclusively by the isomerization, from the analysis of the rise of the CIS spectral component reported in Fig. 3.12 we can estimate

isomerization time to < 3 ps. A more precise determination of this time requires pump-dump-probe experimental approach.

4.5 Comparison with protein environment

The process studied in solution is an *all-trans→cis* isomerization that in protein environment is present in several retinal proteins, like bacteriorhodopsin (bR) and halorodopsin (HR). The former is a proton pump while the latter is an ion pump and in both proteins chromophore isomerizes from *cis* to *all-trans* form. Their similarity is underlined by the fact that with appropriate modification of the residuals surrounding the chromophore, bR can become an ion pump and HR a proton pump [70]. The major difference between them is the photoisomerization efficiency Φ that in bR is very high (~64%) [2] while in HR is only 32% [5] , a value more similar to the one in solution (<24%) [3]. It would be interesting to compare Φ of bR and HR and their mutants in which some aminoacids in the protein pocket surrounding the chromophore have been substituted. Logunov et al. [71] studied several bR mutants and observed that it is hard to make an accurate comparison of the photoisomerization yields. This happens because while in bR only the *all-trans* retinal isomer is present, in mutants also various *cis* isomers appear.

From previous studies [2] we know that in bR Φ is excitation wavelength (λ_{ex}) independent like it is for PSBR in ACN. Unfortunately measurements of Φ for various λ_{ex} were not done for HR so a direct comparison with PSBR in MeOH is not possible. Anyway similarity between ACN and bR can suggest similar local electric field surrounds the chromophore in both environments. Moreover, in ACN Φ is not only wavelength independent on λ_{ex} but also reaches its maximum value in solution. ACN is a solvent both highly polar and non-hydrogen bonding (Table 1.1). On the other hand, in cyclohexane (a non-hydrogen bonding and non polar solvent) Φ drops to the value found in MeOH [31]. This tells us that the polarity of the protein pocket of bR, containing the *all-trans* PSBR chromophore, may be fundamental for photoisomerization efficiency. Polarity may not be

sufficient since MeOH is practically as polar as ACN but the presence of hydrogen bonds seems to decrease Φ.

From X-ray crystallography [20, 21, 72] it has been found that in protein the chromophore is surrounded by water molecules that make H-bonds with it [73, 74]. In contrast to situation in H-bonding solvents, the bond positions can be fixed since the protein pocket is not a floppy environment as the solvent but an ordered and relatively stiff environment. Rhorig et al. [75] found that the chromophore is very flexible in solution, in contrast to the protein environment which, by steric repulsion, restricts the accessible conformational space of the chromophore. We suggest that a highly ordered H-bond network surrounding the chromophore can contribute to Φ enhancement, whereas the constantly changing H-bond network [75], as the one found in solvents, only deteriorates the PSBR photoreactivity.

The amount of force that H-bond exert on the chromophore might also be important for photocatalysis, since in bR (Φ=0.62) H-bonds are stronger than in HR (Φ=0.32) [76, 77].

Solvent environment is most similar to HR in which a biexponential decay was rationalized by the presence of a reactive and a non-reactive channel. The presence of the non-reactive channel explains why in HR Φ is so small with respect to other retinal proteins. Anyway, as in solvent environments, the branching ratio at the CI seems to be very important.

Several computational studies investigated influence of the environment in CI [38, 39, 68]. In a study on Rhodopsin [39] it was found that, in absence of opsin, the shape and character of the PES surrounding the CI does not prompt a preferential formation of the isomerized photoproduct. On the other hand, the protein cavity induces a large deformation of the excited and ground state PESes. The resulting structural asymmetry of the potential energy seems consistent with a situation where the isomerization to all-trans isomer is preferred. Here, the isomerization is 11-cis→*all-trans* was studied but nevertheless it is an important indication of large influence of the protein environment on the PES near the CI. The central role of the branching ratio at CI was evidenced by Nakamura et al.[69] who

studied Φ in HR. These authors found that the branching ratio at the CI is influenced by the interaction between the Schiff base cation and counterions of different size (halide ions). Thus a notable change in the local environment around the Schiff base of the chromophore seems to significantly affects the S_1 PES.

Finally, it is interesting to observe that in some bR mutants the decay of the excited state was found to be biexponential and slower than in wild type bR [71]. In these mutants a positively charged, a negatively charged or neutral hydrogen bonding amino acid residue, known to be functionally important within the retinal cavity, was replaced by a neutral non-hydrogen bonding one. More than one channels appeared, that suggests some hydrogen bonding is necessary to enhance Φ.

5. Conclusion

In this thesis, the dependence of the photoisomerization efficiency (Φ) on the excitation wavelength and the ultrafast dynamics of the photoisomerization process in the protonated Schiff base of *all-trans* retinal (PSBR) have been studied in two different solvents. Methanol (MeOH) and acetonitrile (ACN) were chosen, since the latter has 50% larger Φ with respect to all other solvents [3]. Our motivation was to find out which processes in the excited state are responsible for the photoisomerization reaction and how the environment can make it more efficient.

From the analysis of pump-probe data, apart from three spectral components corresponding to ground state bleaching (GB), excited state absorption (ESA) and stimulated emission (SE), a new spectral component (CIS) was individuated and attributed to *cis* isomer formation and undefined metastable products.
A fast peak was observed in all the kinetic traces between 400 nm and 650 nm and attributed to the early events of the photoisomerization process corresponding to S_2 internal conversion. Vibrational relaxation was found to be faster in ACN ($t < 2$

ps) than in MeOH (t < 5 ps). Further investigations with an improved time resolution are needed for a better characterization of these processes.

Several reactive and non-reactive pathways have been identified in the decay of the S_1 excited state corresponding to internal conversion process. A fast decay of 0.6 ps was observed only in MeOH and attributed to a non-reactive path. Moreover, since steady-state measurements revealed that in MeOH there is a 25% increase of Φ when excitation wavelength is tuned from 400 to 540 nm, it is supposed that a certain amount of the excess energy is necessary to access the non-reactive channel. This enhancement of Φ is not observed in ACN that could be due to its behaviour of vibrationally relax the system faster than in MeOH. The slower decays, ~3 ps and ~10 ps, were attributed to reactive channels. We suppose that the solvent, apart from influencing the branching at the Franck-Condon point between reactive and non-reactive channels, may further influence the branching ratio at the conical intersection so that *cis*-isomer formation is enhanced in ACN.

Still, in bacteriorhodopsin Φ is at least two times larger than in any solvent. Halorodopsin is more similar to PSBR in solution since Φ is comparable and the decay of the excited state is biexponential. This suggests that a small change of the environment and in the hydrogen bonds with the residuals surrounding the PSBR in the protein pocket can drastically change the isomerization efficiency of the chromophore. Moreover, the ordered and stiff protein environment could be able to select only the movements that are necessary for biological function, which is not possible in the floppy solvent environment.

Finally, from the rise of the CIS spectral component we estimate the isomerization time to be < 3 ps. This value is only indicative and further measurements with a pump-dump-probe set-up are necessary.

Bibliography

[1] R.W. Schoenlein, L.A. Peteanu, R.A. Mathies, C.V. Shank. The first step in vision: femtosecond isomerization of rhodopsin. *Science*, 254: 412-415, 1991

[2] J.B. Hurley, T.G. Ebrey, B, Hong, and M. Ottolenghi. Temperature and wavelength effects on the photochemistry of rhodopsin, isorhodopsin, bacteriorhodopsin and their photoproducts. *Nature*, 270: 540-542, 1977.

[3] Y. Koyama, K. Kubo, M. Komori, H. Yasuda, and Y. Mukai. Effect of protonation on the isomerization properties of normal-butylamine schiff-base of isomeric retinal as revealed by direct HPLC analyses: selection of isomerization pathways by retinal proteins. *Photochemistry and photobiology*, 54 (3): 433-443, 1991.

[4] G. Zgrablic, S. Haacke, and M. Chergui. Heterogeneity and relaxation dynamics of the photoexcited retinal Schiff base cation in solution. 2009, *in press*.

[5] P. Hamm, M. Zurek, T. Röshinger, H. Patzelt, D. Oesterhelt, W. Zinth. Femtosecond spectroscopy of the photoisomerization of the protonated Schiff base of all-trans retinal. *Chem. Phys. Lett.,* 263: 613-621, 1996.

[6] B. Hou, N. Friedman, S. Rhuman, M. Shaves, and M. Ottolenghi. Ultrafast spectroscopy of the protonated Schiff bases of free and C_{13}=C_{14} locked retinals. *J. Phys. Chem. B*, 105: 7042-7048, 2001.

[7] O. Bismuth, N. Friedman, M. Sheves, S. Rhuman. Photochemical dynamics of all-trans retinal protonated Schiff-base in solution: excitation wavelength dependence. *Chemical Physics*, 341: 267-275, 2007.

[8] Y.A. Ovchinnikov. Rhodopsin and bacteriorhodopsin: structure-function relationships. *FEBS Lett.*, 148 (2): 179-191, 1982.

[9] P.A. Hargrave, J.H. McDowell, D.R. Curtis, J.K. Wang, E. Jusczak, S.L. Fong, J.K. Rao, P. Argo. The structure of bovine rhodopsin. *Biophis. Struct. Mech.*, 9, 235-244, 1983.

[10] K. Palczewski, T. Kumasaka, T. Hori, C. A. Behnke, H.Motoshima, B. A. Fox, I. Le Trong, D. C. Teller, T. Okada, R. E. Stenkamp, M. Yamamoto, M. Miyano. Crystal structure of rhodopsin: a G-protein coupled receptor. *Science*, 289: 739-745, 2000.

[11] R. E. Stenkamp, D. C. Teller, and K. Palczewski. Crystal structure of rhodopsin: a G-protein coupled receptor. *ChemBioChem*, 3: 963-967,2002

[12] J. Li, P. C. Edwards, M. Burghammer, C. Villa, and G. F. X. Schertler. Structure of bovine rhodopsin in a trigonal crystal form. *J. Mol. Biol.*, 343: 1409-1438, 2004

[13] K. Ozaki, R. Hara, T.Hara, and T. Kakitani. Configurational Changes of the retinal chromophore. *Biophys. J.*, 44 (1) : 127-137, 1983.

[14] I. Hara-Nishimura, M. Kondo, M. Nishimura, R. Hara, T. Hara. Amino acid sequence surrounding the retinal-binding site in retinochrome of the squid, Todaroses pacificus. *FEBS*, 335 (1): 94-98, 1993.

[15] T. Shimamura, K. Hiraki, N. Takahashi, T. Hori, H. Ago, K. Masuda, K. Taki, M. Ishiguro, and M. Miyano. Crystal structure of squid rhodopsin with intracellular extended cytoplasmic region. *J. Biol. Chem.*, 283 (26): 17753-17756, 2008

[16] E. Pebay-Peyroula, G. Rummel, J. P. Rosenbusch, E. M. Landau. X-ray Structure of bacteriorhodopsin at 2.5 Angstroms from microcrystals grown in lipidic cubic phases. *Science*, 277: 1676-1681, 1997

[17] H. Luecke, B. Schobert, H. T. Richter, J. P. C., J. K. Lanyi. Structural changes in bacteriorhodopsin during ion transport at 2 Angstrom resolution. *Science*, 286: 255-260, 1999.

[18] H. J. Sass, G. Büldt, R. Gessenich, D. Hehn, D. Neff, R. Schlesinger, J. Berendzen, and P. Ormos. Structural alterations for proton translocation in the M-state of wild-type bacteriorhodopsin. *Nature*, 406: 649-653, 2000.

[19] D.L. Dorset. Direct structure analysis in protein electron crystallography: crystallographic phases for halorhodopsin to 6-Å resolution. *Proc. Nat. Acad. Sci.*, 92: 10074-10078,1995.

[20] M. Kolbe, H. Besir, L.O. Essen, D. Oesterhelt. Structure of the light-driven chloride pump halorhodopsin at 1.8 Å resolution. *Science*, 288: 1390-1396, 2000.

[21] Y. Shichida and T. Yamashita. Diversity of visual pigments from the viewpoint of G protein activation-comparison with other G protein-coupled receptors. *Photochem. Photobiol. Sci.*, 2: 1237–1246, 2003.

[22] SS. Deeb. The molecular basis of variation in human color vision. *Clin Genet*, 67: 369-377, 2005.

[23] F. Baldissera. *Fisiologia e biofisica medica*. Poletto editore. Seconda edizione, 2000.

[24] G. Wald. *The molecular basis of visual excitation*. Nobel Lecture, December 12, 1967.

[25] N.A. Dencher, D. Dresselhaus, G. Zaccai, end Büldt. G. Structural changes in bacteriorhodopsin during proton translocation revealed by neutron diffraction. *Proc. Nat. Acad. Sci.,*86: 7876-7879, 1989.

[26] R. González-Luque, M. Garavelli, F. Bernardi, M. Merchán, M. A. Robb, M. Olivucci. Computational Evidence in favour of a two-state, two-mode model of the retinal chromophore photoisomerization. *Prot. Nat. Acad. Sci.*, 97 (17): 9379-9384, 2000.

[27] T. Rosenfeld, B. Honig, M. Ottolenghi. Cis-trans isomerization in the photochemistry of vision. *Pure Appl. Chem.*, 49: 341-351, 1977.

[28] M.Gravelli, T. Vreven, P. Celani, F. Bernardi, M. A. Robb, and M. Olivucci. Force fields for "ultrafast" photochemistry: the S_2 $(1B_u)\rightarrow S_1(2A_g)$ reaction path for all-trans-hexa-1,3,5-triene. *J. Am. Chem. Soc.*, 120: 1285-1288, 1998.

[29] A. Sinicropi, A. Migani, L. De Vico, and M. Olivucci. Photoisomerization acceleration in retinal protonated Schiff-base models. *Photochem. Photobiol. Sci.*, 2: 1250-1255, 2003

[30] J. M. Donahue and W. H. Waddell. The trans→cis photoisomerization of protonated retinyl Schiff base. *Photochemistry and Photobiology*, 40 (3): 399-401, 1984.

[31] R. S. Becker and K. Freedman. A comprehensive investigation of the mechanism and photophysics of isomerization of a protonated and unprotonated Schiff base of 11-cis-Retinal. *J. Am. Chem. Soc.*, 107: 1477-1485, 1985.

[32] K. A. Freedman and R. S. Becker. Comparative investigation of the photoisomerization of the protonated and unprotonated n-Butylamine Schiff Bases of 9-cis-, 11-cis-, 13-cis-, and all-trans-retinals. *J. Am. Chem. Soc.*, 108: 1245-1251, 1986.

[33] R. F. Childs and G. S. Shaw. A quantitative examination of the photoisomerization of retinal iminium salts by high-field ^{1}H NMR spectroscopy. *J. Am. Chem. Soc.*, 110: 3013-3017, 1988.

[34] T. Kobayashi, T. Saito, H. Ohtani. Real-time spectroscopy of transition states in bacteriorhodopsin during retinal isomerization. *Nature*, 414: 531-534, 2001.

[35] H. Kandori, Y. Schicida, and T. Yoshizawa. Photoisomerization in Rhodopsin. *Biochemistry*, 66 (11): 1197-1209, 2001.

[36] S. M. Bachilo and T. Gillbro. Fluorescence of retinal Schiff base in Alchools. *J. Phys. Chem.*, 103: 2481-2488, 1999.

[37] V. I. Prokhorenko, A. M. Nagy, S. A. Waschuk, L. S. Brown, R. R. Birge, R. J. D. Miller. Coherent control of retinal isomerization in bacteriorhodopsin. *Science*, 313: 1257-1261, 2006.

[38] M. Ben-Nun, F. Molnar, K. Schulten, and T. J. Martinez. The role of intersection topography in bond selectivity of cis-trans photoisomerization. *Prot. Nat. Ac. Sci.*, 99 (4) : 1769-1773, 2002.

[39] P.B. Coto, A. Strambi, M. Olivucci. Effect of opsin on the shape of the potential energy surfaces at the conical intersection of the rhodopsin chromophore. *Chemical Physics*, 347: 483-491, 2008.

[40] R.A. Mathies, C.H. Brito Cruz, W.T. Pollard, and C.V. Shank. Direct observation of the femtosecond excited state cis-trans isomerization in bacteriorhodopsin. *Science*, 240: 777-779, 1988.

[41] Q. Zong, S. Rhuman, M. Ottolenghi, M. Sheves, N. Friedman, G. H. Atkinson, and J.K. Delaney. Reexamining the primary light-induced events in bacteriorhodopsin using a synthetic C_{13}=C_{14}-locked chromophore. *J. Am. Chem. Soc.*, 118: 12828-12829, 1996.

[42] L. Song and M. A. El-Sayed. Primary step in bacteriorhodopsin photosynthesis: bond stretch rather than angle twist of its retinal excited-state structure. *J. Am. Chem. Soc.*, 120: 8889-8890 (1998).

[43] G. Haran, E. A. Morlino, J. Matthes, R. H. Callander, R. M. Hochstrasser. Femtosecond polarized pump-probe and stimulated emission spectroscopy of the isomerization reaction of rhodopsin. *J. Phys. Chem. B*, 103: 2202-2207, 1999.

[44] G. Zgrablic. Solvent effects on the ultrafast dynamics of the retinal chromophore of bacteriorhodopsin. *PhD thesis*, 2006.

[45] S. K. Dilaimi, J. C. Aumiller, R. H. Johonson, and P. E. Blatz. Spectroscopic examination of hydrogen bonding and proton transfer in model

Schiff bases related to the visual pigment chromophore. *Photochem. Photobiol.*, 46: 403-412, 1987.

[46] T. Arlt, S. Schmidt, W. Zinth, U. Haupts, and D. Oesterhelt. The initial reaction dynamics of the light-driven chloride pump halorhodopsin. *Chem. Phys. Lett.*, 241: 559-565, 1995.

[47] R. R. Birge, L. P. Murray, R. Zidovetzki, and H. M. Knapp. 2-photon, c-13 and two-dimensional h-1-nmr spectroscopic studies of retinal Schiff-bases, protonated Schiff-bases, and Schiff-base salts – evidence for a protonation induced π-π^* excited-state level ordering reversal. *J. Am. Chem. Soc.*, 109 (7): 2090-2101, 1987.

[48] Operator's manuals for VERDI and MIRA, Coherent laser division

[49] Legend user manual, Coherent laser division

[50] G. P. Agrawal and M. J. Potasek. Nonlinear pulse distortion in single-mode optical fibers at the zero-dispersion wavelength. *Physical Review A*, 33 (3): 1765-1776, 1986.

[51] G. P. Agrawal, P. L. Baldeck, and R. R. Alfano. Temporal and spectral effects of cross-phase modulation on copropagating ultrashort pulses in optical fibers. *Physical Review A*, 40 (9): 5063-5072, 1989.

[52] S. A. Kovalenko, A. L. Dobryakov, J. Ruthmann, and N. P. Ernsting. Femtosecond spectroscopy of condensed phases with chirped supercontinuum probing. *Physical Review A*, 59 (3): 2369-2384, 1998.

[53] K. Ekvall, P. van der Meulen, C. Dhollande, and L.-E. Berg. Cross phase modulation artifact in liquid phase transient absorption spectroscopy. *Journal of applied physics*, 87 (5): 2340-2352, 2000.

[54] R. R. Alfano and S. L. Shapiro. observation of self-phase modulation and small-scale filaments in crystal and glasses. *Phys. Rev. Lett.*, 24 (11): 592-594, 1970

[55] A. Brodeur and S. L. Chin. Ultrafast white-light continuum generation and self-focusing in transparent condensed media. *J. Opt. Soc. Am. B*, 16 (4): 637-650, 1999

[56] L. De Carlo. Spettroscopia con onda evanescente mediante spettro continuo prodotta da una fibra non lineare. *Tesi di laurea*, 2006

[57] J.-C. Diels and W. Rudolph. Ultrashort laser pulse phenomena. *Academic Press*, 1996.

[58] W. Holzer, H. Gratz, T. Schmitt, A. Penzkofer, A. Costela I. García-Moreno, R. Sastre, F.J. Duarte. Photo-physical characterization of rhodamine 6G in a 2-hydroxyethyl-methacrylate methyl-methacrylate copolymer. *Chemica Physics*, 256: 125-136, 2000.

[59] F. Demartini, C. H. Townes, T. K. Gustafson, P. L. Kelley. Self – steepening of light pulses. *Phys. Rev.*, 164 (2): 312-323, 1967.

[60] D. Andersson and M. Lisak. Nonlinear asymmetric pulse distorsion in long optical fibers. *Opt. Lett.*, 7 (8): 394-396, 1982.

[61] D. Andersson and M.Lisak. Nonlinear asymmetric self-phase modulation and self-steeping of pulses in long optical waveguides. *Phys. Rev. A.*, 27: 1393-1398 (1983).

[62] I. H. M. van Stokkum, D. S. Larsen, and R. van Grondelle. Global and target analysis of time-resolved spectra. *Biochimica at Biophysica Acta*. 1657: 82-104, 2004.

[63] L. Bonacina. Ultrafast structural dynamics in electronically excited many-body systems. *PhD thesis*, 2004.

[64] M. Vengris. Biological photoreactions explored by multi-pulse ultrafast spectroscopy. *PhD thesis*, 2005

[65] M. Ricci. Misura dell'efficienza di isomerizzazione del retinale in funzione dell'energia dei fotoni assorbiti. *Tesi di laurea*, 2008.

[66] A. Cembran, F. Bernardi, M. Olivucci, and M. Garavelli. Counterion controlled photoisomerization of retinal chromophore models: a computational investigation. *J. Am. Chem. Soc.*, 126: 16018-16037, 2004.

[67] A. Cembran, F. Bernardi, M. Olivucci, and M. Garavelli. Excited-state singlet manifold and oscillatory features of a nonatetraeniminium retinal chromophore model. *J. Am. Chem. Soc.*, 125: 12509-12519, 2003.

[68] I. Burghardt and J. T. Hynes. Excited-state charge transfer at a conical intersection: effects of an environment. *J. Phys. Chem. A*, 110, 11411-11423, 2006.

[69] T. Nakamura, S. Takeuchi, M. Shibata, M. Demura, H. Kandori, and T. Tahara. Ultrafast pump-probe study of the primary photoreaction process in

paranoids halorodopsin: halide ion dependence and isomerization dynamics. *J. Phys. Chem. B*, 112: 12795-12800, 2008.

[70] G. Vero. Analogies between Halorhodopsin and bacteriorhodopsin. Biochimica set Biophysical Act, 1460: 220-229 (2000).

[71] S. L. Logion, M. A. El-Spayed, L. Song, and J. K. Lanai. Photoisomerization quantum yield and apparent energy content of the K intermediate in the photocycle of bacteriorhodopsin, its mutants D85N, R82Q, and D212N, and deionised blue bacteriorhodopsin. *J. Phys. Chem.*, 100 (6): 2391-2398, 1996.

[72] T. Okada, Y. Fujiyoshi, M. Silow, J. Navarro, E. M. Landau, and Y. Shichida. Functional role of internal water molecules in rhodopsin revealed by x-ray crystallography. *Pub. Nat. Ac. Sci.*, 99 (9) : 5982-5987, 2002.

[73] M. Shibata, T. Tanimoto, and H. Kandori. Water molecules in the Schiff base region of bacteriorhodopsin. *J. Am. Chem. Soc.*, 125: 13312-13313, 2003.

[74] Y. Furutani, M. Shibata , and H. Kandori. Strongly hydrogen-bonded molecules in the Schiff base region of rhodopsins. *Photochem. Photobiol. Sci.*, 4: 661-666, 2005.

[75] U. F. Röhrig, L. Guidoni, U. Rothlisberger. Solvent and protein effects on the structure and dynamics of the rhodopsin chromophore. *Chemphyschem.* 6 (9): 1836-1847, 2005.

[76] M. Shibata, N. Muneda, K. Ihara, T. Sasaki, M. Demura, and H. Kandori. Internal water molecules of light-driven chloride pump proteins. *Chem. Phys. Lett.*, 392: 330-333, 2004.

[77] M. Shibata, K. Ihara, and H. Kandori. Hydrogen-bonding interaction of the protonated Schiff base with halides in a chloride-pumping bacteriorhodopsin mutant. *Biochemistry*, 45: 10633-10640, 2006.